UNIVERSITY OF STRATHCLYDE

Department of Civil and Environmental Engineering

Synthesis of Calcium Silicate Hydrate (C-S-H) and novel cementitious materials: characterisation, engineering applications and environmental aspects

by

Riccardo Maddalena
BEng, MEng

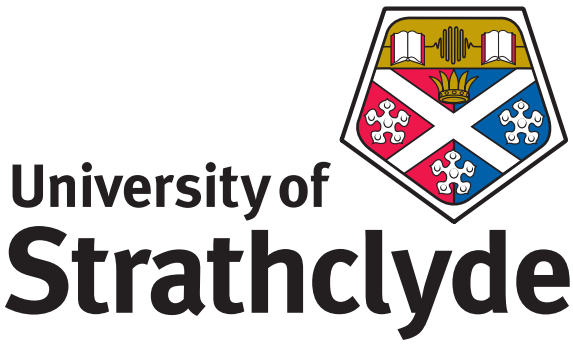

A thesis presented in fulfilment of the
requirements for the degree of

Doctor of Philosophy

May 2018

This thesis is the result of the author's original research. It has been composed by the author and has not been previously submitted for examination which has led to the award of a degree. Chapters which have already been published in peer reviewed journals or have been submitted for publication, during the course of this degree are indicated. My contribution and those of the other authors to this work has been explicitly indicated below. I confirm that appropriate credit has been given within this thesis where reference has been made to the work of others. The work presented in Chapter 5 was previously published in Construction and Building Materials (Elsevier) as *"Low-pressure silica injection for porosity reduction in cementitious materials"* by Riccardo Maddalena (student) and Dr. Andrea Hamilton (PhD supervisor), 2016. This study was conceived by all of the authors. I carried out the experiment design, analysis, data collection, results interpretation and the draft of the manuscript. The supervisor contributed to the data analysis, the water transport calculations, and the revision of the manuscript prior submission to the journal. The work presented in Chapter 6 was previously published in Journal of Cleaner Production (Elsevier) as *"Can Portland cement be replaced by low-carbon materials?"* by Riccardo Maddalena (student), Dr Jen J. Roberts and Dr. Andrea Hamilton (PhD supervisor), 2018. This study was conceived by all of the authors. I carried out the experiment design, analysis, data collection, results interpretation and the draft of the manuscript. Dr Roberts contributed to the environmental aspects and the supervisor contributed to the data analysis, and the revision of the manuscript prior submission to the journal.

Signed: _____

Date: _____

to my beloved family and to my dad

Acknowledgements

As for every step of my life, I have never been alone and I wish to thank all the people that have made this journey unforgettable.

While most of the students find the PhD a stressful time, and many end up in tears, I enjoyed it a lot. It was a beautiful and memorable experience that truly changed my life.

First and foremost I want to thank Dr Andrea Hamilton, who supervised my work with patience and enthusiasm. It was an honour to be her first PhD student at University of Strathclyde. She has been a constant and maternal presence in my progression from doctoral student to researcher. She has taught me the *beauty* of science, and the determination to achieve results with confidence and scientific rigour. She has been a model to follow through the years and her dedication has inspired not only my research and study but also my personal development. Dr Hamilton has always believed in me and I am thankful for her continuous trust and faith.

Besides my supervisor, I would like to thank the rest of my thesis committee, Prof. Leon Black and Dr Grainne El Mountassir for their insightful comments and encouragement, but also for the hard questions which encouraged me to widen my research from various perspectives.

I would like to acknowledge the lab staff (John, Derrek, Gavin, and Mara), the IT friend Darren and the administrative staff for their support through Health and Safety and bureaucracy.

A special thank goes to my friends and PhD *mates* Alessia, Brunella and Gea, *Il Comitato*, for their friendship, their patience, and their support. I cannot ever think doing my PhD without them. They have been the *fun*, lunch, drinks, travels (etc) and the *hard-work*, the advice, the suggestions and the life-improvements.
I would also like to thank my friends at Strathclyde, Matteo, James, Bruna, Silvia, Michela, Livia, Carolina, Andrea Maroni for their support and kindness, their advice and their company. Thanks to them I have always felt a sense of family in the department.
I thank my fellow labmate Sara, for the stimulating chats, the sleepless nights working together and the successful *journey* to the Diamond Light House.

My PhD experience could not have been the same without two dear friends, soon Dr Amy and soon Dr Phil. The Scottish and the English. Amy has been a true friend and the best *excuse* ever for a tea/coffee break. Our chat spanned from history to science (and gossips!). I thank Phil for his genuity and his friendship. From him I learned how to look at life simply and easy.

A special acknowledgement goes to two of my best friends: Crapiz, for all our bets, for the beers, the food and the company for the past 4 years, and his wise advice. Peppe, for being my friend despite the distance, for being there no matter when and where, for being always in my life. It has certainly helped me to made it here.

I would also like to thank Andrew, for being there while I was completely immersed in my PhD. He has been patient, caring and supportive, believing in my potential and my capabilities.

Last but not the least, I would like to thank my family: my mum and my brothers and sister for supporting me spiritually throughout writing this thesis and my life in general, and specially Noemi and Emanuele, part of my family away from home.

Abstract

This doctoral dissertation describes the synthesis and characterisation of calcium silicate hydrate (C-S-H) phase and other cementitious materials. C-S-H is the most important mineral phase in ordinary Portland cement (OPC), accounting for strength and hardening. Its characterisation has been the subject of research in the past 70 years and yet there are still gaps in knowledge and understanding. In this work the development of a novel method process for direct synthesis of solid calcium silicate hydrate (C-S-H) phases is proposed, by mixing calcium hydroxide and silica. This method allows crystal structural determination of the synthetic mineral, and permits characterisation at the atomic scale and also mechanical-hydraulic measurements on monoliths, rather than the more traditional slurry format. The method is easy, relatively fast and highly reproducible. In particular, structure evolution of synthetic C-S-H is studied under varying calcium to silica ratio, curing time and silica particle size, using either silica fume or nano-silica (particle size). While this method advantageously produces solid C-S-H, its production at bulk-scale is also evaluated by means of a life cycle assessment and compared to other OPC-free binder materials. Novel OPC-free cementitious binders are in fact developed and characterised in terms of mechanical and thermal performance. Proposed as an environmentally friendly alternative to Portland cement, these innovative cementitious materials have a lower carbon footprint and contribute to reduce Portland cement consumption and its CO_2 emissions. Hydrothermal synthesis of C-S-H is carried out to investigate the response to hot and wet conditions, typical of cement encapsulation in deep geological storage of radioactive waste. As a result of these investigations, synthesis conditions have been proven to be the key in "tailoring" and designing the C-S-H structure at the nano-scale. C-S-H produced is used as a crack-sealing agent in aqueous injection. A lab-scale investigation shows that aqueous nano-silica injected through a hardened cement matrix reacts with calcium hydroxide naturally present in hydrated Portland cement producing additional C-S-H and reducing the overall porosity and permeability. This study explores the potential use of solid C-S-H to repair large scale structures which are wet or under water, such as legacy ponds in nuclear waste storage facilities.

Contents

List of Figures

List of Tables

List of Symbols

d	day
h	hour
t	time
φ	open porosity
2θ	diffraction angle
V	volume
L	length
k_s	saturated permeability coefficient
Q	volumetric flow or diffraction spacing
D	hydraulic diffusivity
k_B	Boltzmann's constant
r	radius
η	viscosity
m_s	water saturated mass
m_d	dried mass
2θ	X-ray diffraction angle
RH	relative humidity
Δ	dimensionless parameter in Avrami equation
$\oslash$	diameter
λ	thermal conductivity or wave-length
ϱ	(bulk) density
ϱ_{mat}	matrix density
ϱ_w	density of water
U	thermal transmittance
R	thermal resistance
R_c	mechanical resistance
A_w	capillary absorption coefficient
ξ	coefficient of tortuosity
μ	gradient of the C/S ratio equation
ϵ	stoichiometric correction factor
α_v	coefficient of volumetric expansion

Abbreviations

C-S-H	calcium silicate hydrate
C-A-S-H	calcium aluminum silicate hydrate
XRD	X-Ray diffraction
SEM	scanning electron microscopy
FE-SEM	field emission scanning electron microscpy
W-SEM	tungsten emission scanning electron miscroscopy
BSE-SEM	Back scattering scanning electron miscroscopy
OPC	ordinary Portland cement
TEOS	tetraethyl orthosilicate
TGA	thermogravimetric analysis
DSC	differential scanning calorimetry
C_3S	alite
C_2S	belite
C/S	calcium to silica
LCA	life cycle analysis
CO_2	carbon dioxide
PDF	pair distribution fucntion
NMR	nuclear magnetic resonance
XRF	X-ray fluorescence
EDX	energy-dispersive X-ray spectroscopy
TEM	transmission electron microscopy
TMS	tetramethylsilane
CL	chain length
PTFE	polytetrafluoroethylene
CDW	construction and demolition waste
WBCSD	World Business Council for Sustainable Development
IEA	International Energy Agency
UHPC	ultra high performance cement
X-CT	X-ray computer tomography
IC	isothermal calorimetry
FTIR	Fourier-transform infrared
XAFS	X-ray absorption fine structure
AAC	autoclaved aerated concrete

Chapter 1

Introduction

1.1 Literature review

Cement is a binding agent in concrete and mortars that due to its relatively low production-cost has become the most used building material world-wide. Interestingly, it is widely employed in the construction industry not only as a structural element (reinforced concrete), but also as a refinement layer for insulation and decoration purposes, in masonry design and in a range of application such as weirs, dams, railways, oil-well installations and lately in nuclear waste confinement. Due to the wide availability of raw materials such as limestone and clay and the relative simplicity of the production process, cement history dates back to the Romans, when it was first adopted in unreinforced concrete: the Roman Pantheon is an example of a successful recipe of highly pozzolanic materials, such as volcanic ash, incorporated in what was once called Roman concrete, or *opus caementicium*. The most frequently used cement, and probably the most known, is ordinary Portland cement (OPC), for centuries adopted in construction industry either as a main material or as a binder in masonry structures. By combining Portland cement with fine and coarse aggregates and water it is possible to obtain the building material called concrete.

Because cement is employed in a wide range of applications (housing, bridges, soil grouting, geotechnical foundations, dams, highways infrastructure), it must satisfy safety requirements and characteristics, named *specifications* in international standards and Eurocodes (i.e. class,

strength, etc.). Cement use in buildings can range from renders and mortars used to prevent dampness ingress in domestic buildings to ultra high performance cement (UHPC) used as structural elements which require sulphate and chloride resistance.

Due to its versatile usage, cement and concrete research is in continuous progress. Researchers have investigated novel cement mixtures to respond to the increasing demand of smart cementitious materials. Bentz and co-workers studied porosity evolution of concrete pastes incorporating silica fume, which has a particle size range lower than OPC [1]. Micro and nano-particles play an important role in cement and concrete hydration: they act as a "filler", reducing the water penetration (or other potential contaminants) [2], improving compressive strength and enhancing the long term durability [3, 4]. Furthermore, micro and nano-particles used as a replacement for OPC in concrete contributes to the sustainability of construction materials production [5], reducing the demand and consequentially the manufacturing of OPC in place of 'green' materials, such as fly ash, metakaolin, nanosilica and silica fume.

Ordinary Portland cement Portland cement is made from limestone and clay burnt at calcination temperature (*ca.* 1500 °C). The product obtained is called *clinker*, grounded to make it in powder and mixed with low amount of gypsum, to control setting time and workability. In Table 1.1 an approximate oxide and compounds composition of Portland cement is presented [6].

Table 1.1: Approximate oxides composition of typical Portland cement clinker. Titanium, manganese, phosphorus and chromium oxides are usually $< 0.1\%$.

Oxide	Content (%)
CaO	60–67
SiO_2	17–25
Al_2O_3	3–8
Fe_2O_3	0.5–0.6
MgO	0.1–0.4
Alkalis	0.2–1.3
SO_3	1–3

The aforementioned oxides combine to form phases such as tricalcium silicate, dicalcium silicate, tricalcium aluminate, and tetracalcium aluminoferrite, as indicated in cement chemistry

notation respectively C_3S, C_2S, C_3A and C_4AF. Na_2O and K_2O are minor compounds, known as alkalis. Hydration of cement is a chemical reaction in which, when water (H in cement chemistry notation) is added to cement, it forms a hard gel, the so called calcium silicate hydrate (C-S-H) gel, which gives strength to the paste, along with other phases such as ettringite, calcium aluminun hydrates and alumino-ferrite hydrates. At the beginning, hydration of C_3S (also known as alite) occurs, which is responsible for the early development of strength, whereas hydration of C_2S (known as belite) is slower and responsible for secondary strength development of cement [7]. The hydration reaction (not exact stoichiometry equations) for alite (1.1) and belite (1.2) can be written as follows [6]:

$$2C_3S + 6H = C_3S_2H_3 + 3Ca(OH)_2 \tag{1.1}$$

$$2C_2S + 4H = C_3S_2H_3 + Ca(OH)_2. \tag{1.2}$$

As result of the hydration reaction a certain quantity of calcium hydroxide is produced, often as portlandite and a nearly amorphous phase of C-S-H, having the properties of a rigid gel [8]. C-S-H appears in semi-amorphous state, with an acicular or plate-like morphology. As a poorly crystalline material, direct identification of C-S-H through X-ray diffraction has been the subject of controversial opinion from many authors. In order to better understand the microstructure and its formation, researchers have attempted to synthesise C-S-H gel, using different environmental conditions and starting materials. C-S-H gel has been obtained both directly from stoichiometric mixtures and thermal treatments of calcium, silica and water [9, 10] and indirectly from the hydration of tricalcium silicate [11, 12, 13]. Microstructure of C-S-H has been studied using X-Ray diffraction (XRD), scanning electron microscopy (SEM) at high resolution (100 nm to 5 μm) and nuclear magnetic resonance (NMR) spectroscopy. The hydration of calcium silicates has been studied by means of isothermal calorimetry (IC) and differential scanning calorimetry (DSC), to calculate the rate of hydration by measuring the heat released during chemical reaction with water [14, 15, 16]. Many more techniques have been used to look at C-S-H. Such as transmission electron microscopy (TEM), Fourier-transform infrared (FTIR) spectroscopy, Raman spectroscopy, X-ray computer tomography (X-CT) and

synchrotron beamlines, particularly XRD, pair distribution fucntion (PDF), X-ray absorption fine structure (XAFS) spectroscopy etc.

Nano-particles in cement The addition of micro and nano-particles into cement paste has represented an interesting research field in the last decade. It has been found that addition contributes to enhance ultimate strength in concrete structures, reduce permeability and improve durability with ageing [17, 18, 19, 20].

In the 2000s, the usage of nano-particles in cement technology attracted the attention of researchers and industries, bringing useful developments not only in construction itself but also in the economical assessment of building materials and their environmental impact. Production of Portland cement has increased exponentially in the last century and consequently the emissions of CO_2 in the atmosphere associated with clinker manufacture [21]. World-wide concrete industries are responsible for *ca.* 5–7% of the global greenhouse gas (GHG) emissions [22]. Hence, totally or partially replacing OPC with nano-particles represents a successful strategy in the development of *green* building materials [23, 24].
Silicon dioxide (SiO_2) nano-particles, also called nano-silica, have been investigated as partial replacement in concrete mixtures and ceramics. As shown in Figure 1.1, adapted from Sobolev et al., (2005) [23], decreasing the particle size range results in an increase in specific surface area: it means a higher reactivity and silica nano-particle surface acts as a nucleation site for crystal growth and the formation of C-S-H gel.

It has been proven that the addition of fine particles such as fly ash, metakaolin, silica fume enhances the durability of cement or concrete, improves the compressive and flexural strength and gives increased fire resistance [25, 26]. Carbon nano-tubes have also been used as an admixture in concrete, ceramics and solar cells, and it has been found that they play an important role in improving durability and crack prevention in concrete and enhancing thermal properties in ceramics [27]. Micro-systems such as clay and phyllosilicates, thermally converted into an unstable phase by the dehydroxylation of kaolinite, commercially known as metakaolin, constitutes an emerging OPC-free binder, known as alkali activated cement (AAC) or geopolymers [28, 29]. Titanium dioxide TiO_2 nano-particles, are used in construction

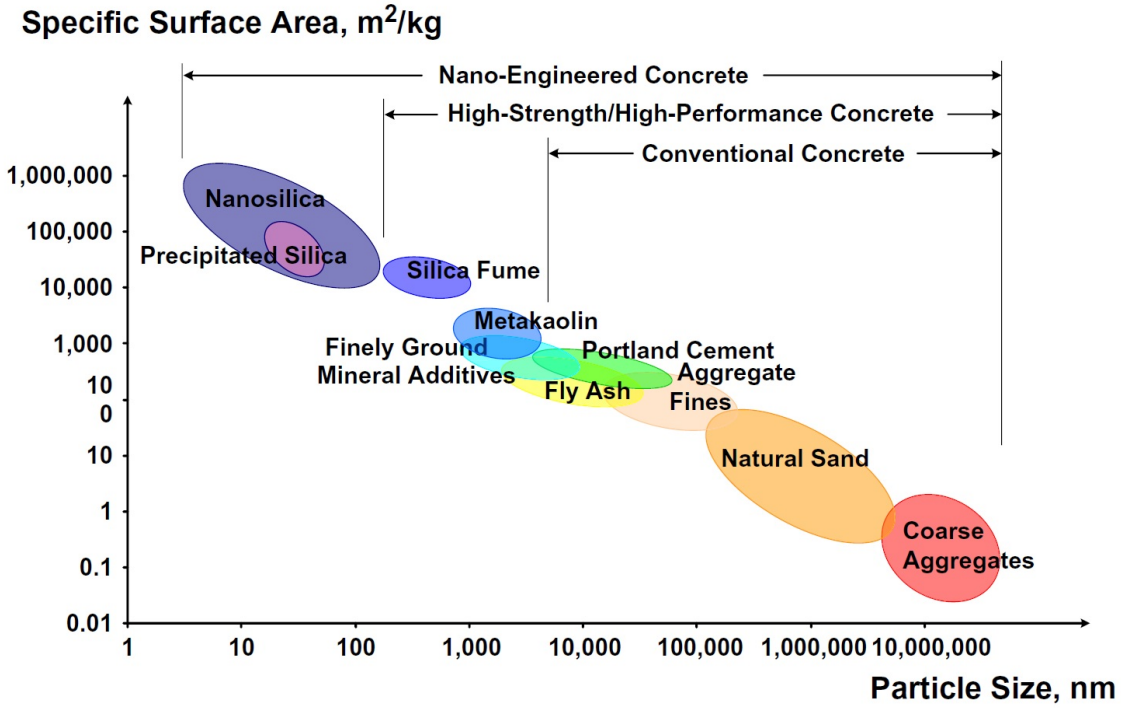

Figure 1.1: Particle size range and specific surface area of micro and nano-particles compared to aggregates in ordinary Portland cement. Image adapted from Sobolev et al., (2005).

technology under the name of photocatalytic (or photo-activated) cement [30]. They are responsible for the rapid hydration of concrete and self-cleaning behaviour, enabling elimination of bacterial films, and functioning as anti-fouling agents under solar irradiation [25].

Deterioration of concrete due to aggressive environmental conditions, and overloading leads to the formation of nano-cracks (10–100 nm width) or micro-cracks (0.1–1000 μm width) which represents a preferential pathway for the ingress of water and potential contaminants and consequently rebar corrosion [31]. When detected on time, cracks can be "healed" by means of sealing agents. Crack-sealing has been made possible by the addition of sealing compounds in concrete mixtures such as sodium silicate spheres [32]. Self-healing bacteria have also been proposed as a crack-healing agent, reacting with carbon dioxide (CO_2) (present in atmospheric air and in the cracks) and calcium hydroxide (portlandite), naturally present in OPC, to precipitate calcium carbonate which fills the cracks [33, 34, 35]. Application of crack-sealing agents in existing structures has been attempted using electro-migration techniques, reported by Cardenas et al., (2008) [36]. However, scaling up such technology is challenging due to the

thickness of real-scale walls (thickness of domestic constructions' walls is in the range 25–40 cm) and the voltage required to mobilise nano-particles into the cracks.
In this section a brief review of Portland cement, its hydration and research advances on cement technology have been presented. In depth reviews of synthesis methods to make C-S-H, specifically the silica particle size and the effect of synthesis conditions can be found in *Chapter 2*, *Chapter 3* and *Chapter 4* respectively. *Chapter 5* contains a detailed review of crack-sealing techniques in cement and water transport. Finally an in-depth discussion of OPC-free cementitious materials and their environmental impact is presented in *Chapter 6*.

1.2 Aim of this work

Research questions Only in the 20th century, thanks to modern technologies, was it possible to fully investigate the microstructure of hydrated Portland cement, discovering that the main phase formed is a poorly crystalline structure called calcium silicate hydrate (C-S-H). C-S-H not only is the main hydrated phase in OPC, which makes up *ca.* 75 wt.%, but it is also the main responsible for strength and hardening. Characterisation of C-S-H and its complex structure has been subject of lively debate from the first crystallographic work by J.D. Bernal in the 1950s to the present, driven by a strong interest in tailoring its chemo-mechanical properties and create 'designer' cements with self-healing capabilities or improved resilience to fracture. Advances in understanding and accuracy of the characterisation of C-S-H have contributed to adopting this particular 'man-made' mineral in a large variety of applications well beyond the construction industry: synthetic C-S-H is nowadays largely employed in human dental repairs and reconstruction; C-S-H bodies, commonly known as calcium silicate boards, are used as thermal insulation materials. In addition to this, C-S-H has been also recently studied as a cation-exchange mineral for metal sequestration and immobilisation.

It is known that the degree of disorder in C-S-H varies with calcium to silica ratio, which varies with synthesis method. The morphology of synthetic C-S-H appears to be different from 'natural' C-S-H formed as a result of OPC hydration: in the latter, the mineral forms constrained between grain of sands (and aggregates, in case of concrete) assuming a typical

needle/acicular shape, whereas in synthetic synthesis often presents a foil-structure. The first question that this thesis addresses is: *how does the synthesis method of C-S-H affect its structure and stoichiometry?* The exponentially increasing amount of research on the characterisation of C-S-H often makes it very difficult or impossible to compare data and results obtained using different synthesis methods, different raw materials and experimental approaches. In this work a novel, easy and relatively fast synthesis process for C-S-H is proposed: parameters such as calcium to silica ratio, curing time, silica particle size and curing temperature are investigated. Particularly, hydrothermal synthesis of C-S-H is described in a dedicated *in-situ* experiment, using synchrotron X-ray radiation. This work studies the C-S-H/portlandite crystal growth/dissolution and has the potential to accurately test long term durability of novel cements for toxic and radioactive waste applications, where high temperature governs the cement hydration and structure evolution.

Another research question is addressed in regards to the durability of the concrete structure: *could additional C-S-H be used as a crack-sealing agent?* Cracking in building materials is a very common phenomenon. In concrete and mortar paste, formation of cracks (micro and nano) can appear either straight after casting in the mould or with ageing. It can be attributed to many factors (aggressive environment, temperature, load, ageing and construction technique) and can be observed either in the free surface or can be found at the concrete-steel interface. Durability of building materials is related to the presence of cracks since they represent a fast pathway to the transport of liquid and gasses that potentially contain water or hazardous compounds.

Restoration and preservation of historical buildings has been investigated through the application of silica particles used to promote crack healing. The cementitious materials used included nano-particles such as nano-silica and silica fume. The lower particle size range and the high reactivity due to the higher specific surface area of nano-particles offer the capability of interacting with calcium sources naturally present in hydrated cement and forming binding and strengthening compounds such as C-S-H phases. Studied at the nano-scale, this process can improve mechanical and hydraulic properties of existing building materials by using non-destructive techniques such as localized injection through micro and macro-size cracks.

The increasing demand of Portland cement for concrete production has raised serious concerns in the global community, due to its environmental impact. Cement is responsible for approximately 5–7% of the anthropogenic CO_2 emissions, and researchers and industries leaders have recently taken action toward a more sustainable construction industry. Researchers have looked at supplementary cementitious materials to be used as partial replacement of OPC or other binding compounds free from any Portland cement, called alkali-activated cement or geopolymer. To answer to the final research question this thesis addresses: *can Portland cement be replaced by low-carbon alternative materials?*, novel OPC-free cement systems are investigated and characterised, and compared to traditional cement. Their mechanical and thermal properties are evaluated and an engineering application for such materials is proposed. Finally the environmental impact, based on a simplified life cycle analysis (LCA) of novel OPC-free materials is assessed in terms of greenhouse gas emissions associated with their production.

The *fil rouge* of the thesis The novelty of the proposed method for the synthesis of C-S-H in *Chapter 6* is the production of a solid form which is easy to make in bulk. The benefit of a solid form is emphasised in *Chapter 6*, where mechanical and hydraulic properties of OPC-free binders, including C-S-H monoliths, are investigated and compared to OPC, and their production at bulk-scale is evaluated using a simplified LCA. C-S-H produced according to the synthesis method described was used as a crack-sealing agent via aqueous injection. *Chapter 4* emphasises the simplicity of the synthesis method and its ability to form and seal micro-cracks under water, such as legacy storage ponds in nuclear power stations, where structural maintenance is one of the major challenges. Investigations in *Chapter 3* and *Chapter 4* explores how C-S-H and its atomic structure responds to extreme environments, such as cement used in the deep geological storage of radioactive waste.

1.3 Outline of the thesis

Chapter 2 of this thesis presents the development of a novel process for the synthesis of C-S-H. It describes the chemical formation of C-S-H from calcium hydroxide, nano-silica and water,

at different target calcium to silica (C/S) ratios. The work presented in this chapter has been submitted to the international journal *Construction and Building Materials* (Elsevier), as "Direct synthesis of solid Calcium Silicate Hydrate phase with tobermorite-like structure" by Riccardo Maddalena (student), Prof. Kefei Li and Dr. Andrea Hamilton (PhD supervisor) and is currently under review.

This study was conceived by the first and third author. I carried out the experiment design, analysis, data collection, results interpretation and the draft of the manuscript. The supervisor contributed to the data analysis, the synchrotron XRD patterns' analysis and lattice parameter calculations, the SEM images and the revision of the manuscript prior submission to the journal. Prof. Li has contributed to the thermo-gravimetric equations description and the revision of manuscript. Diamond Light Source Ltd personnel contributed to the X-ray Pair Distribution Function (PDF) data collection and analysis, reported in the manuscript.

Chapter 3 reports an experimental investigation on the influence of silica particle size on the formation of C-S-H and its physiochemical properties. Particularly, thermal analyses provide an insight to the hydration kinetics of C-S-H and its stoichiometry. This work has been submitted to the international journal *Thermochimica Acta* (Elsevier) as "Effect of silica particle size on the hydration of Calcium Silicate Hydrate investigated by thermal analysis" by Riccardo Maddalena (student) and Dr. Andrea Hamilton (PhD supervisor) and is currently under review.

This study was conceived by all of the authors. I carried out the experiment design, analysis, data collection, results interpretation and the draft of the manuscript. The supervisor contributed to the data analysis, the mathematical models, and the revision of the manuscript prior to submission to the journal.

Chapter 4 describes the synthesis of C-S-H under hydrothermal conditions and its characterisation *ex-situ* using university laboratory facilities, and *in-situ*, using high-energy synchrotron X-ray radiation to attain time-resolved XRD patterns. This work has been submitted to the international journal *Cement and Concrete Research* (Elsevier) as "In-situ XRD studies on hydrothermal synthesis of Calcium Silicate Hydrate: the influence of temperature on stoichiometry" by Riccardo Maddalena (student), Dr. Stefan Michalik and Dr. Andrea Hamilton

(PhD supervisor) and it is currently under review.

This study was conceived by the first and third author. I carried out the experiment design, analysis, data collection, results interpretation and the draft of the manuscript. Dr. Michalik contributed to the instrument set-up and calibration, data collection and analysis, and the revision of the drafted manuscript. The supervisor contributed to the experiment design and set-up, data collection and analysis, coding of Matlab scripts for data analysis, and the revision of the manuscript prior to submission to the journal.

Chapter 5 reports an experimental investigation on the usage of synthetic C-S-H as crack-sealing agent for reduction of permeability. The work presented was previously published in the international journal *Construction and Building materials* (Elsevier) as "Low-pressure silica injection for porosity reduction in cementitious materials" by Riccardo Maddalena (student) and Dr. Andrea Hamilton (PhD supervisor), vol. 134 (2017) pages 610–616.

This study was conceived by all of the authors. I carried out the experiment design, analysis, data collection, results interpretation and the draft of the manuscript. The supervisor contributed to the data analysis, the water transport calculations, and the revision of the manuscript prior submission to the journal.

Chapter 6 reports an overview of physical and chemical properties of novel cementitious materials, compared to OPC. The work describes cement pastes made by different pozzolanic materials, such as metakaolin, silica fume, and nano-silica at different synthesis conditions and stoichiometry. Mechanical and thermal performances are assessed and compared to traditional OPC pastes. Greenhouse gas (GHG) emissions associated with the production of these novel cements are estimated and compared to those associated with the production of OPC. The work has been submitted to the international *Journal of Cleaner Productiona* (Elsevier) as "Can Portland cement be replaced by low-carbon alternative materials? A study on thermal properties and carbon emissions of innovative cements" by Riccardo Maddalena (student), Dr. Jen J. Roberts and Dr. Andrea Hamilton (PhD supervisor) and has been accepted for publication.

This study was conceived by the first and third author. I carried out the experiment design, analysis, data collection, results interpretation and the draft of the manuscript. Dr.

Roberts contributed to the greenhouse gas emissions calculation and environmental impact section, and the revision of the drafted manuscript. The supervisor contributed to analysis and results interpretation, the thermal conductivity measurement technique developed and presented, and the revision of the manuscript prior to submission to the journal.

Chapter 7 summarises the major findings of this doctoral dissertation and outlines future research work.

1.4 Funding and Support

This study was financially supported by the EPSRC grant: EP/L014041/1 [DISTINCTIVE–*Decommissioning, Immobilisation and Storage soluTIons for NuClear wasTe InVEntories*. Nuclear magnetic resonance spectroscopy analyses were conducted at Tsinghua University in Beijing (PR China) and supported by the European Commission via the Marie Curie IRSES project: FP7-PEOPLE-2013-IRSES-612665 [GREAT–*Geotechnical and geological Responses to climate change: Exchanging Approaches and Technologies on a world-wide scale*] and the research fund of Tsinghua University, grant: 2014Z01004. Synchrotron XRD investigations were conducted at the UK Diamond Light Source, experiment number: EE12533-4 in beamline I12 (JEEP, Joint Engineering, Environmental, and Processing) and I15-1 (XPDF, X-ray Pair Distribution Function). Data collected contributed to the results presented here.

Chapter 2

Direct synthesis of solid Calcium Silicate Hydrate phase with tobermorite-like structure

Abstract. The main phase present in Portland cement is a semi-crystalline calcium silicate hydrate (C-S-H) with variable, and also tailorable, stoichiometry. Its crystal structure has an expandable *b*-axis which allows for cation substitution, and as such there has been research on uptake of environmental contaminants and radionuclides into the C-S-H structure, particularly in the applied field of nuclear wasteforms and encapsulation. A novel method for synthesising solid form C-S-H is proposed here, by reacting an aqueous nano-silica (SiO_2, average particle size 5–20 nm) suspension with calcium hydroxide $Ca(OH)_2$ dissolved in deionised water, which is suitable for large scale batch mixing. Samples were characterised using thermal analysis (TGA/DSC), synchrotron XRD and PDF, NMR spectroscopy and SEM. This study proposes a novel, fast and comparatively simple method of synthesising solid C-S-H. Results show that crystallinity of the C-S-H varies with the C/S ratio. A simple linear relationship between target and actual C/S ratio is shown, and it will be a useful tool for experimentalists and practitioners to create C-S-H with confidence in the stoichiometry of the end product.

2.1 Introduction

Cement is the world's most produced material with nearly 2 billion tonnes manufactured globally per year, which creates 1.6 billion tonnes of CO_2 and makes cement production a significant contributor to greenhouse gas emissions [37]. Calcium silicate hydrate (C-S-H) gel, a poorly crystalline phase with variable stoichiometry, makes up *ca.* 75 wt.% of the final hydrated product in ordinary Portland cement (OPC) [38], therefore the bulk and micro-structural properties of C-S-H gel have attracted significant research activity over the last few decades, particularly its ability to adsorb contaminants and radionuclides such as Cl, Cs, Zn, Sr, Co, U etc. [39, 40, 41].

To accurately characterise and structurally tailor C-S-H, researchers have attempted to synthesize pure C-S-H without any accessory minerals present. This has been carried out in a variety of ways, Cong and Kirkpatrick (1996) synthesized C-S-H from β-C_2S and water or from fumed silica, lime and water at final calcium to silicate (C/S) ratios of 0.4–1.85 mol/mol through a long-term reaction process, lasting 2–10 months [42]. Samples were dried under nitrogen flow and characterized using laboratory powder X-ray diffraction (XRD), ^{29}Si MAS NMR spectroscopy and X-ray fluorescence (XRF). Harris et al., (2002) synthesized C-S-H by mixing calcium oxide and colloidal silica suspension under a nitrogen atmosphere, achieving an entire sample C/S ratio range of 0.8–3.0 mol/mol. The actual C/S ratio in the composite C-S-H and portlandite system obtained at higher target C/S values is unknown because it was not measured [43]. Their C-S-H was prepared as a slurry, no solid state chemical characterization was performed but the solubility of C-S-H was tested via leaching experiments.

Garbev et al., (2008) synthesized nano-crystalline C-S-H by reacting calcium oxide with silicon dioxide and distilled water [44]. The synthesis involved mechanical milling to prepare slurries at different C/S ratios followed by nitrogen-drying at 60 °C. Samples were characterized using laboratory powder XRD and synchrotron XRD. Rietveld refinement was used to obtain unit cell dimensions which showed a correlation between C/S ratio values and the interlayer spacing in C-S-H. Pardal et al., (2009) synthesized C-S-H by mixing calcium oxide with amorphous precipitated silica and water, producing a slurry to be filtered [45]. Samples were

then washed with an alcohol-water mix and dried under vacuum for 5 days. C-S-H samples were characterised by powder XRD and energy-dispersive X-ray spectroscopy (EDX) combined TEM analysis. No further results were presented on the C-S-H structure or the relationship between ageing and degree of crystallinity.

Foley and co-workers synthesized C-S-H by mixing calcium oxide and micro-silica at a 1:1.5 $CaO:SiO_2$ ratio [9, 10]. Slurries were mixed for 7 days and then dried using two different techniques: vacuum-drying and drying at low relative humidity over a saturated lithium chloride solution. Products were characterised using powder XRD, ^{29}Si MAS NMR and SEM. Although the synthesis was carried out over 7 days the C-S-H reaction was not complete, pure C-S-H samples were not obtained and the presence of portlandite was recorded. Tränkle et al., (2013) obtained 11 Å tobermorite by microwave assisted synthesis using quartz as the Si precursor with silicic acid and calcium hydroxide at low C/S ratios (0.36–0.83 mol/mol) [46]. TEM analysis showed the formation of nano-crystalline C-S-H. Despite the high degree of crystallinity obtained, some unreacted material remained. Very recent research, combining experiment with thermodynamic calculations and molecular dynamic simulation, has shown for the first time that pure C-S-H can be produced with a C/S ratio of up to 2 mol/mol and without portlandite present. [47]. The C/S ratio is known to play a crucial role in the formation of C-S-H and influences not only the chemistry but also the compressive strength [48].

In this work a novel method to produce solid C-S-H is proposed, which simply mixes calcium hydroxide with nano-silica and deionised water, at fixed water content and room temperature without microwave assistance or applied heat and with mixing time of a few minutes. In addition, the C-S-H is solid state, which has a potential range of uses in construction and environmental contaminant remediation, which a slurry may not have. The novelty of this technique is its relative simplicity, speed, comparative low cost and formation of solid C-S-H which can be designed and characterised both mechanically and physico-chemically.

2.2 Materials and methods

2.2.1 Materials

Synthetic C-S-H phases were prepared using calcium hydroxide or calcium oxide and nano-silica, at set target C/S molar ratios. Reagent grade powdered calcium hydroxide, $Ca(OH)_2$, (CAS number: 1305-62-0, molecular mass: 74.093 g mol^{-1}) commercially available from Sigma Aldrich was used. Calcium oxide was obtained by controlled calcination of reagent grade calcium carbonate, $CaCO_3$ (CAS number 471-34-1, molecular mass: 100.0869 g mol^{-1}). Ludox TM-50 nano-SiO_2 (CAS number 7631-86-9, molecular mass: 60.08 g mol^{-1}) aqueous suspension was also purchased from Sigma Aldrich. Nano-silica particle size range is 5–20 nm. Decarbonated water was used for mixing, made by bubbling nitrogen through deionised water [42]. Component material characteristics are reported in Table 2.1.

Table 2.1: Characterisation of calcium hydroxide and nano-silica solution from the data sheet provided by the supplier

Material	Calcium hydroxide	Nano-silica
Physical state	white fine powder	suspension in H_2O
Composition	$Ca(OH)_2$: $\geq$ 95.0%	SiO_2: $\geq$ 50.0%
	S compounds: $\leq$ 0.1%	H_2O: $\geq$ 50.0%
	$CaCO_3$: $\leq$ 3.0%	
Anion traces	Cl^-: $\leq$ 0.03%	Cl^-: $\leq$ 0.05%
Cation traces	Fe: $\leq$ 0.05%	
	K: $\leq$ 0.05%	
	Mg: $\leq$ 0.05%	
	Na: $\leq$ 0.05%	
	Sr: $\leq$ 0.05%	
pH at 25 °C	12.4 (slurry)	8.5–9.5
Particle size range (nm)	-	5–20
Mass density at 25 °C (g ml^{-1})	2.24	1.40
Specific area (m^2 g^{-1})	20–41 (hydrated)	110–150

2.2.2 Synthesis process

Synthetic C-S-H phases were prepared according to the target C/S molar ratios in Table 2.2 at room temperature. Dry calcium hydroxide or calcium oxide powder was manually mixed with nano-silica suspension for 2 min at water to total solid (w/s) ratio of 2. After mixing under a nitrogen atmosphere to minimize carbonation, samples were cast into plastic moulds (2.5 × 2.5 × 2.5 cm), stored in a sealed nitrogen environment at controlled conditions (temperature of 20 ± 1 °C, RH 98 ± 2%) and cured for a maximum of 28 days. Bleeding or phase segregation of the paste was not observed. After curing for 1, 3, 7 or 28 days, samples were placed in an acetone bath for 24 hours to remove pore water and halt the hydration for accurate materials characterisation [49, 50]. The solid C-S-H produced showed hygroscopic properties similar to calcium silicate board materials (open porosity $\phi = 0.93$ and capillary absorption coefficient $A_w = 1.22$ kg m^{-2} s$^{-1/2}$) or aerated autoclaved concrete (open porosity $\phi = 0.85$ and capillary absorption coefficient $A_w = 0.13$ kg m^{-2} s$^{-1/2}$) for which *ca.* 6 min are calculated to fully saturate a sample of $15{\cdot}10^{-6}$ m^3 [51]. Hence an acetone bath prolonged for 24 hours was sufficient to saturate the sample with acetone (density = 791 kg m^{-3}). After one day, samples were dried under constant nitrogen flow for an additional 24 hours. Specimens were then stored in a vacuum-sealed bag until required. The schematic process of the synthesis is shown in Figure 2.1. Samples for TGA/DSC analysis alone were oven dried at 60 °C for 100 hours to remove pore water prior to TGA analysis. All samples were then manually ground and sieved, to obtain a homogeneous fine powder for TGA and XRD characterisation.

2.2.3 Powder X-Ray Diffraction

Powder XRD analyses were performed using a Bruker D8 Advance diffractometer with CuKα radiation over the range 5–60° 2θ, step size of 0.02° 2θ and 0.5 s step^{-1}. DiffracEva software from Bruker was used for XRD pattern evaluation and phase identification. Structural analysis was carried out at the UK synchrotron *Diamond Light Source*, using a 2D monochromatic high-energy beam (79.949 keV and $\lambda = 0.15508$ Å) on beamline I12, Joint Engineering, Environmental and Processing (JEEP). The detector geometry was calibrated using a diffraction

Table 2.2: Sample mixes (calcium hydroxide and nano-silica), target C/S ratio values and curing time.

Sample	Target C/S ratio mol/mol	Curing time days
CSH-0.81_1d	0.81	1
CSH-0.81_3d	0.81	3
CSH-0.81_7d	0.81	7
CSH-0.81_28d	0.81	28
CSH-1.00_28d	1.00	28
CSH-1.20_28d	1.20	28
CSH-1.50_28d	1.50	28
CSH-2.40_28d	2.40	28

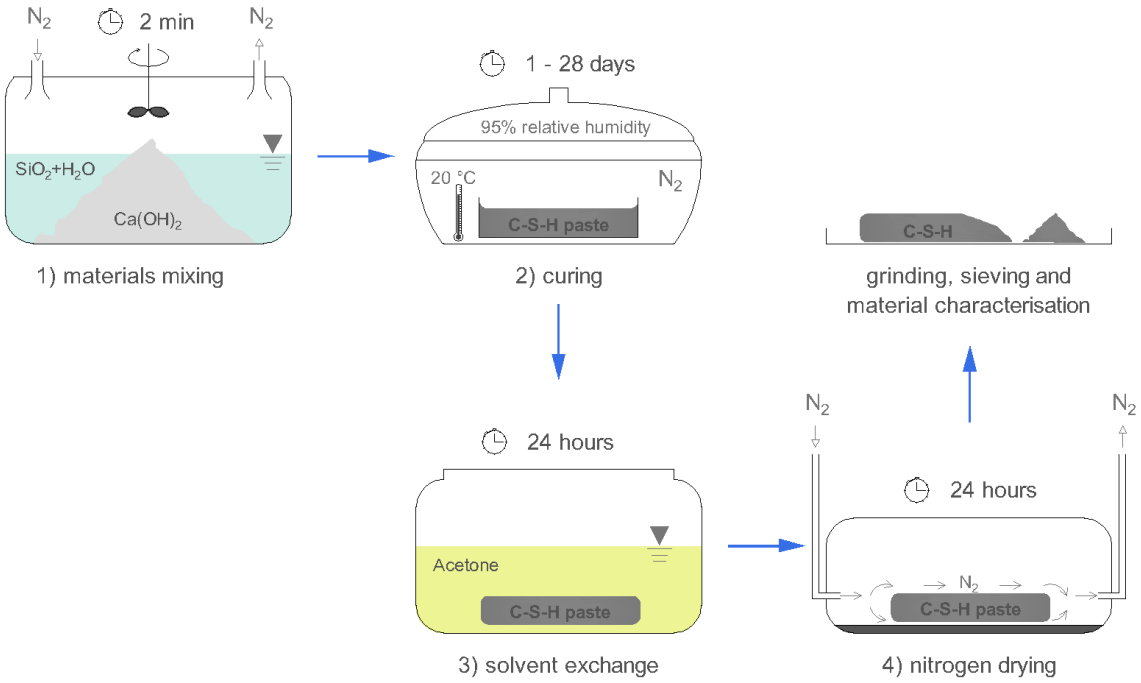

Figure 2.1: Diagram explaining the synthesis process of C-S-H phases: 1) raw materials mixing; 2) sample casting and curing under controlled environmental conditions, 3) solvent exchange in acetone bath to replace pore-water and 4) nitrogen drying at room temperature.

pattern of CeO_2 NIST SRM 674b and the program *DAWN* was used to process collected data [52]. The powdered sample was placed into a borosilicate capillary tube (⊘ 1.13 mm, height 80 mm) and sealed. Diffraction patterns were collected on samples with the lowest and the highest C/S target ratios of 0.81 and 2.40 respectively and compared with C-S-H synthesized by reacting calcium oxide with nano-silica suspension to achieve a target C/S ratio of 1.07 mol/mol. Samples were mixed according to the synthesis process described above but calcium oxide powder was used instead of calcium hydroxide. Diffraction data were collected over a Q range of 0.5–21.0 $Å^{-1}$ and analysed using *MATLAB*. High energy synchrotron XRD data allows accurate structural analysis of the C-S-H phase which is impossible to achieve using laboratory XRD. Room temperature pair distribution function (PDF) data were collected during the commissioning of the XPDF beamline (I15-1) at *Diamond Light Source*. Powder samples were sealed inside borosilicate capillaries (⊘ 0.5 mm, height 90 mm). X-ray scattering data were collected for C-S-H samples at C/S ratio of 0.81 and 1.0 mol/mol at an energy of 66.6 keV in Rapid-Acquisition PDF geometry using a Perkin Elmer XRD1611CP3 area detector [53]. CeO_2 (NIST SRM 674b) XRD pattern was used a calibration standard. The scattering data ($0.5 \leq Q \leq 20$ $Å^{-1}$) were corrected and processed into PDF data using the program *DAWN* [52].

2.2.4 Solid state NMR spectroscopy

^{29}Si MAS NMR spectra were acquired on a JEOL-600 JNM-ECZ spectrometer using a CP/MAS probe for 8 mm o.d. PSZ rotors, ν_R = 6.0 kHz and a relaxation delay of 30 s, available at Tsinghua University, Beijing, China. Chemical shifts are reported in parts per million (ppm) relative to an external sample of tetramethylsilane (TMS) using an external sample of β-Ca_2SiO_4 (δ_{iso} = -71.33 ppm) as secondary reference. The deconvolutions of the ^{29}Si MAS NMR spectra were performed by Lorentzian function fitting using the JEOL DELTA software.

2.2.5 Thermo-gravimetric analysis

Thermo-gravimetric (TG) and differential scanning calorimetry (DSC) data were collected using a NETSZCH STA 449 F1 Jupiter. Measurements were conducted on powder samples weighing 15–25 mg, under constant nitrogen flow at a heating rate of 10 °C min^{-1} from 25 °C to 1000 °C. Prior to measuring, samples were oven-dried at 60 °C for *ca.* 100 h under nitrogen flow to remove any remaining pore water and acetone [54]. Results are plotted as mass loss (%) and heat flow (mW mg^{-1}) as a function of the temperature (°C). TGA/DSC measurement results were used to calculate the actual C/S molar ratio of the samples.

2.2.6 Scanning electron microscopy

Microstructure was characterised using a scanning electron microscope (FEG-SEM, Hitachi SU6600) with energy dispersive spectroscopy (EDS, Oxford INCA-7260) and an accelerating voltage of 15–20 keV. SEM samples were prepared as follows: fresh C-S-H paste was cast into a plastic mould (⊘ 15 mm, thickness 2 mm) and templated onto a thin layer (*ca.* 0.125 mm) of muscovite mica at the bottom of the mould to produce a flat surface for analysis. After curing for 28 days, the specimen was dried under constant nitrogen flow, followed by vacuum drying and surface coating for SEM imaging purposes. This method has the distinct advantage of avoiding resin impregnation and polishing or drying at elevated temperatures, which can alter the microstructure of the sample, and the muscovite mica sheet, which is atomically flat, can be easily removed from the C-S-H sample prior to analysis.

2.3 Results and discussions

2.3.1 XRD characterisation of synthetic C-S-H

XRD analyses on C-S-H samples at C/S target ratio of 0.81 mol/mol show increased formation of C-S-H with ageing (Figure 2.2 *top*). After 1 day of curing, broad peaks at *ca.* 29.5° 2θ and 49.5° 2θ indicate the presence of C-S-H. Portlandite peaks can be observed after 1 day of curing, whereas negligible portlandite has been recorded after 3 days ($< 2\%$). After 7 days of

curing pure C-S-H has formed and the XRD pattern shows well defined reflections at *ca.* 29.5° and 32° 2θ, typical of C-S-H. Other characteristic peaks of this mineral phase can be observed at *ca.* 6°, 16.8°, 49.5° and 54.5° 2θ, in agreement with Sugiyama et al., (2008) and Foley et al., (2012) [55, 9]. Increasing the C/S ratio (Figure 2.2 *bottom*) from 0.81 to 1.00 produces peak broadening at low 2θ angles, precipitation of portlandite (C/S = 1.20 mol/mol) and peak broadening of the strongest C-S-H reflection at 29.5° 2θ, shouldered with portlandite at 28.6° 2θ (C/S = 1.50 and 2.40 mol/mol) [38, 44]. The patterns show similar peak positions to tobermorite structures. One of the main differences is the position and intensity of the basal reflection at *ca.* 7.8° 2θ, which is often shifted towards a lower angle in C-S-H compared to 11 Å tobermorite [56]. As the C-S-H may be present in an amorphous form, it might not be detected by laboratory X-ray diffractometry. Semi-quantitative analyses of XRD patterns was obtained by integrating the peaks assigned to each mineral phase present, C-S-H and portlandite. Results are reported in Figure 2.3 (*top*) and Figure 2.3 (*bottom*). Degree of crystallinity was calculated using *Bruker DIFFRAC.EVA* software. As curing time increases, the quantity of portlandite decreases and therefore the general degree of sample crystallinity decreases as one would expect (Figure 2.3 *top*), confirmed by semi-crystalline C-S-H detected by XRD. An inverse trend is observed when the C/S target ratio increases, which produces an increase in portlandite and therefore a higher degree of crystallinity (Figure 2.3 *bottom*), due to the presence of portlandite crystals. High energy synchrotron XRD patterns of C-S-H at C/S target ratios of 0.81 and 2.40 mol/mol are shown in Figure 2.4 and are compared to C-S-H obtained by mixing calcium oxide and nano-silica at a C/S target ratio of 1.07 mol/mol following the synthesis process previously described. Samples with a target C/S ratio of 0.81 mol/mol show a better fit to 14 Å tobermorite (ICSD collection code 152489 [57]) and lower crystallinity compared to the sample with C/S of 1.07. In both cases, no portlandite is present, so the degree of crystallinity is relative to pure C-S-H only. The pattern from a sample of C/S ratio of 1.07 mol/mol shows broad peaks associated with nano-crystallinity and turbostratic stacking disorder [56]. The structure includes elements of both 11 Å tobermorite (ICSD collection code 92942 [58]) and 14 Å tobermorite (ICSD collection code 152489 [57]). In the synchrotron XRD pattern of the sample with a target C/S ratio of 2.4 mol/mol, a clear

shift of the main peak (at around 29° 2θ) is observed. It is attributed to shrinkage in the crystallographic *b*-direction (*ca.* 1.0%) from omission of bridging tetrahedra. In accordance with Garbev et al., (2008) and Soyer-Uzun et al., (2012) this shift is correlated with the C/S ratio [44, 59]. Increasing the C/S molar ratio decreases the *d*-spacing of the C-S-H structure. In the sample pattern with the highest C/S molar ratio, crystalline portlandite reflections are also observed (ICSD collection code 15471). In Table 2.3 the main peak positions for C-S-H phases and the associated *d*-spacing values are reported. X-Ray structure factors are related to the total pair distribution function, *N(r)*. As described in the work of Soyer-Uzun et al., (2012) *"the integral of N(r)dr has a direct physical interpretation as the number of atoms that are present within a range (r, r+ dr) from any given atom"* [59]. Peaks located at 1.66 Å and 2.44 Å correspond to Si-O and Ca-O correlations, respectively. In samples C-S-H at C/S ratio of 0.81 and 1.0 mol/mol, it was found that an increase of C/S ratio of *ca.* 20% (from 0.81 to 1.0 mol/mol) does not influence the average Si-O and Ca-O distance but a decrease in intensity is observed. The integrated intensity can be related to the abundance of Si and Ca atoms in the C-S-H structure. Based on structural modelling, the decrease of PDF intensity is related to Si occupancy in the atomistic structure of C-S-H. In particular a decrease in intensity results from an increase in Si vacancies and omission of Si bridging tetrahedra [59, 60].

Table 2.3: C-S-H main peak positions and *d*-spacing values obtained from synchrotron XRD analysis

Sample	Target C/S ratio mol/mol	Main peak position 2θ	*d*-spacing Å
CSH-0.81	0.81	28.98	3.079
CSH-1.07	1.07	29.11	3.065
CSH-2.40	2.40	29.30	3.046

2.3.2 NMR measurements

Results of ^{29}Si MAS NMR measurements of the samples at different C/S ratio are displayed in Figure 2.5. In samples with low C/S ratio (0.81, 1.0 mol/mol) three different peaks are resolved, corresponding to end groups of SiO_4^{4-} tetrahedra (Q^1 sites, δ_{iso} = -79.5 ppm),

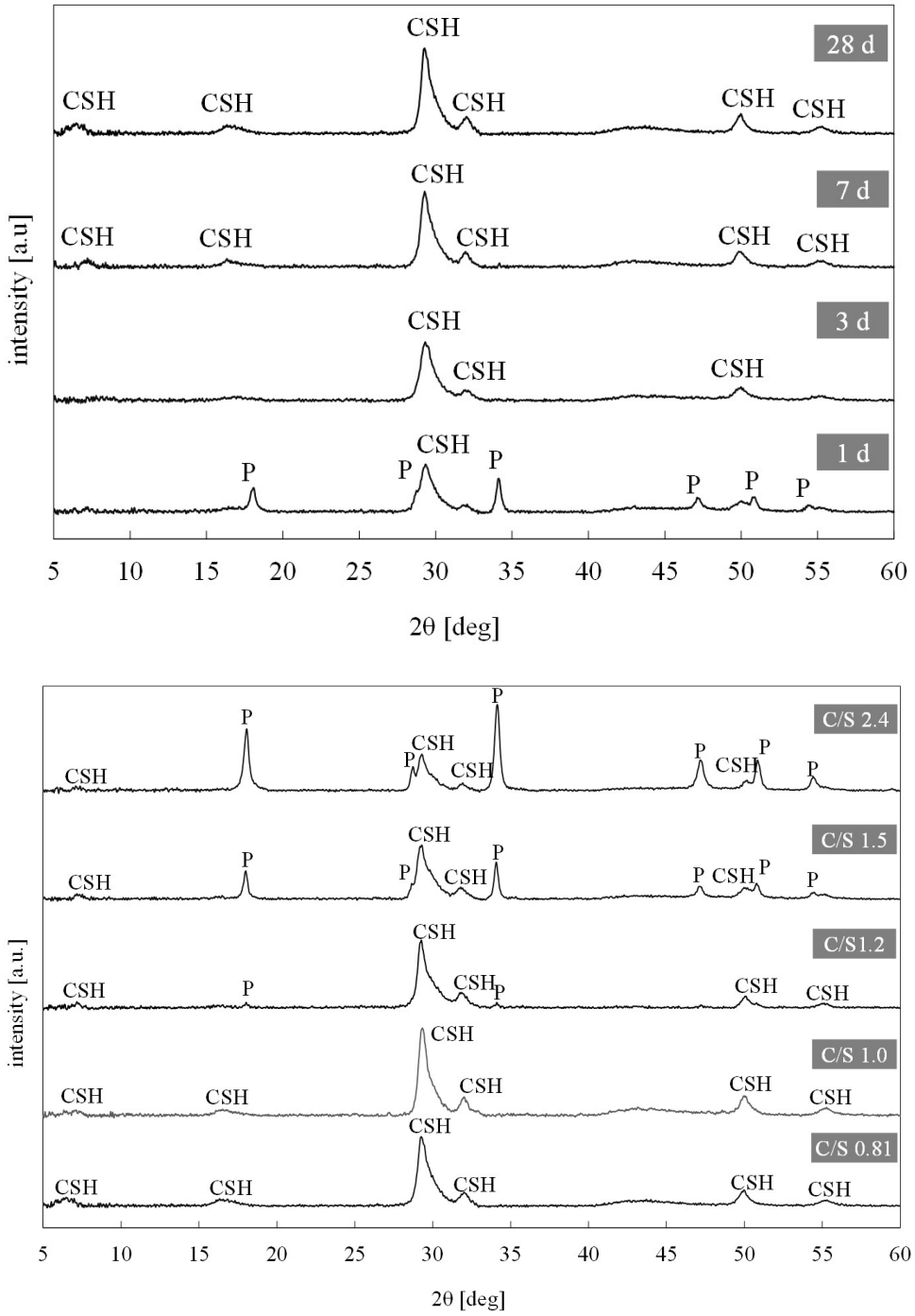

Figure 2.2: XRD patterns of sample at target C/S ratio of 0.81 at different ages (*top*) and samples cured for 28 days at different target C/S ratios (*bottom*). [P: portlandite reflection; CSH: calcium silicate hydrate reflection].

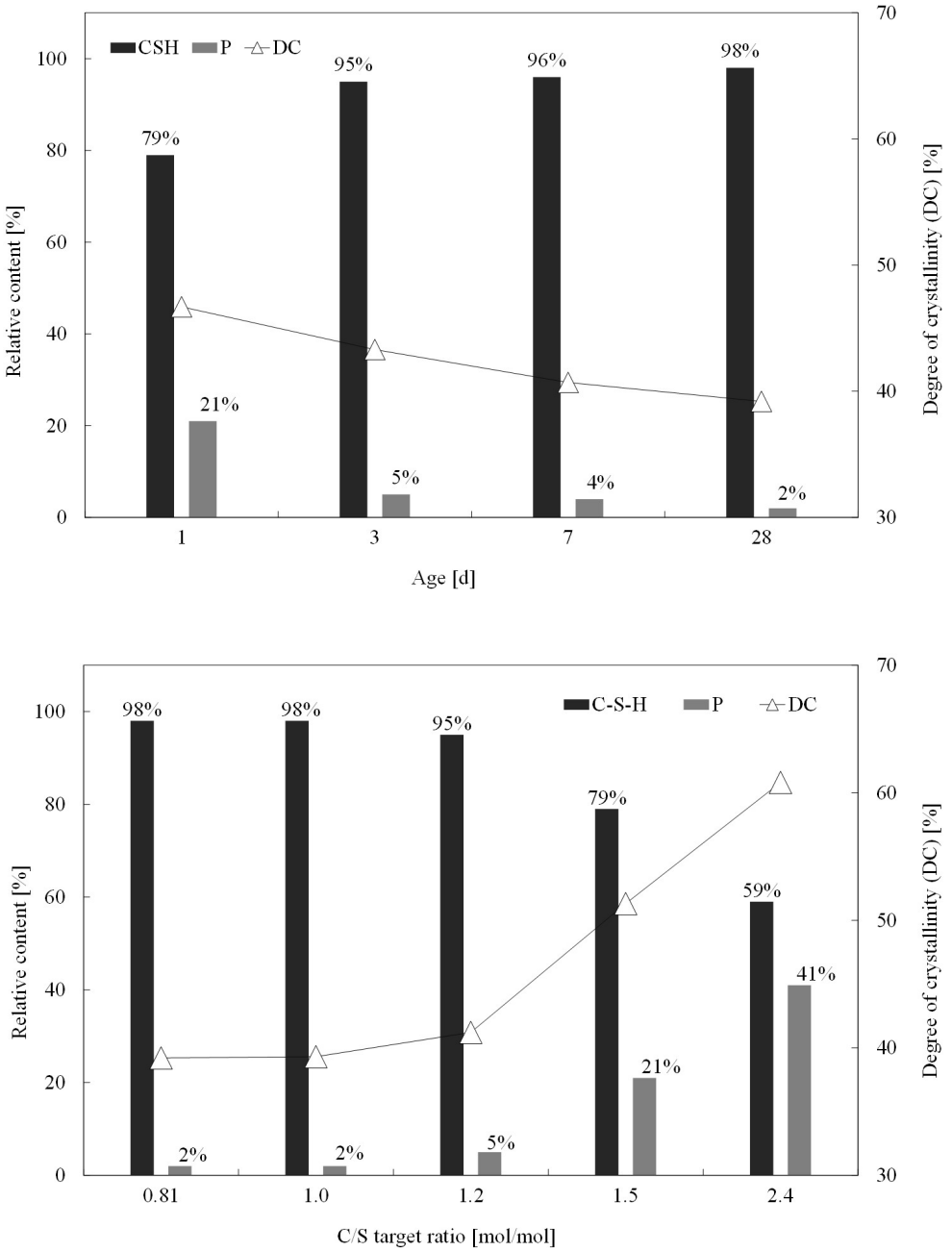

Figure 2.3: Semi-quantitative XRD analysis and degree of crystallinity of sample at C/S ratio of 0.81 as function of the age (*top*) and samples cured for 28 days at different target C/S ratios, as function of target C/S ratios (*bottom*). [P: portlandite reflection; CSH: calcium silicate hydrate reflection].

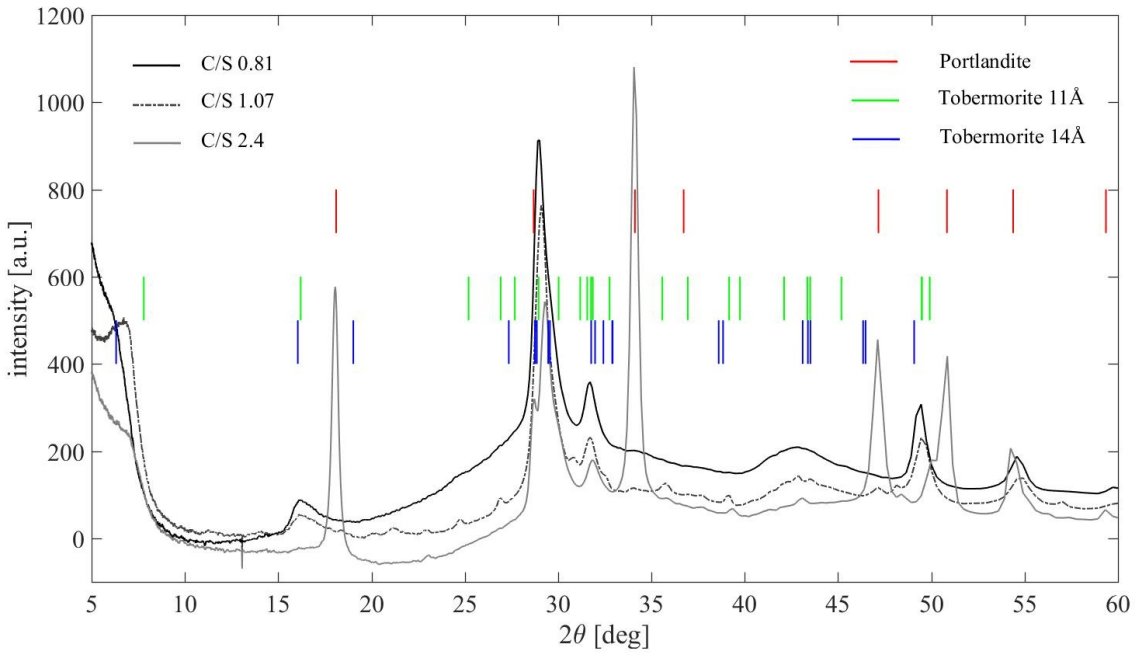

Figure 2.4: Synchrotron XRD analysis of CSH at three different C/S target ratios (0.81, 1.07 and 2.40 mol/mol) with reference diffraction peaks positions of portlandite, 11 Å tobermorite and 14 Å tobermorite.

bridging and paired SiO_4^{4-} tetrahedra (respectively Q_b^2 sites and Q_p^2 sites , δ_{iso} = -82.8 ppm and δ_{iso} = -85.2 ppm) [42, 61]. Increasing C/S ratio results in more Q^1 sites and fewer Q_b^2 sites, meaning that the silicate chains become shorter and the molecular structure of C-S-H is mainly composed of silicate dimers. The synthesised C-S-H shows a defect tobermorite-like structure in which, at higher C/S ratio, silicon is absent from bridging sites, in accordance with previous studies [62, 60, 48]. Removal of Si bridging tetrahedra leads to a maximum C/S ratio of 1.25 mol/mol [44, 54], hence at C/S ratio >1.25 precipitation of portlandite is observed, but minimal differences in the NMR spectra are detected. Furthermore, chain length values are in agreement with the view that C-S-H in samples at C/S $\leq$ 1.4 has a structure similar to 14 Å tobermorite, while mixes with C/S ratio $\geq$ 1.4 mol/mol have a Ca-rich phase intermixed with C-S-H [63]. At higher C/S ratio in fact, portlandite was observed in XRD patterns. NMR chemical shifts change to less negative values as a result of more Ca^{++} incorporation in the interlayer [64]. Deconvolution of the NMR spectra allowed us to calculate the degree of

polymerisation by calculating silica chain length (CL) using equation 2.1:

$$CL = \frac{2[I(Q^1) + I(Q_b^2) + I(Q_p^2)]}{I(Q^1)} \tag{2.1}$$

where CL is the mean chain length of SiO_4^{4-} tetrahedra and I is the relative intensity of the Q^1, Q_b^2 and Q_p^2 resonances of the C-S-H. In Figure 2.6 the chain length CL is shown as a function of the C/S target ratio and values are in agreement with other reported results [62, 64]. Increasing the C/S ratio results in shorter silicate chain length, inducing a de-polymerisation of the structure, therefore C-S-H is mainly composed of dimeric silicates [44]. Moreover, the change in relative intensity $I(Q_b^2)$ from C/S 0.81 to C/S 1.0 mol/mol is in agreement with the X-Ray PDFs results, where a decrease in PDFs intensity indicates more Si vacancies [60]. Furthermore, the exponential decrease in mean chain length, which levels out at values of *ca.* 2–3 at a C/S ratio beyond 1.5 mol/mol, is in agreement with the findings in Richardson (2014) [63].

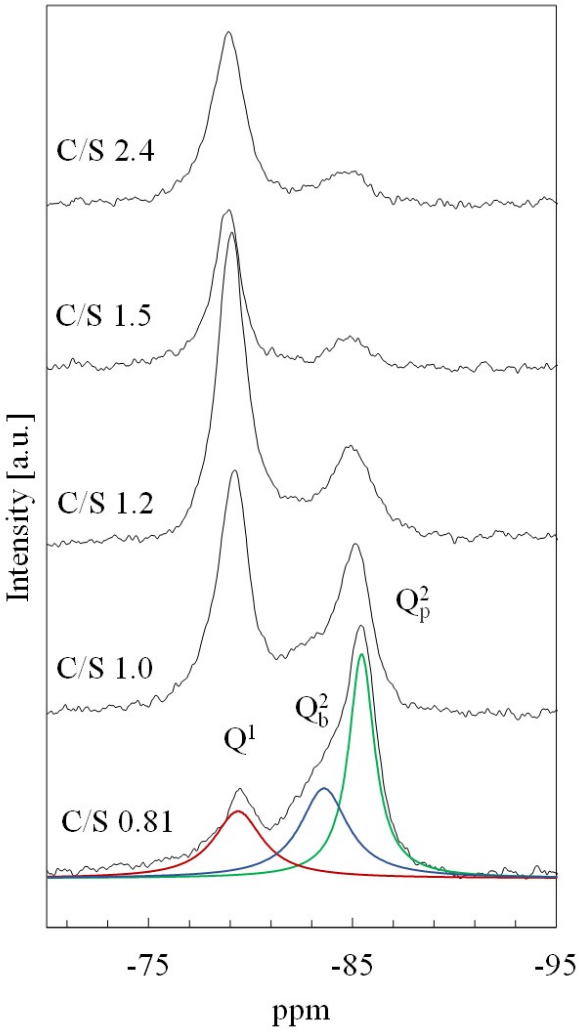

Figure 2.5: ^{29}Si MAS NMR spectra (ν_R=6.0 kHz, 30 s relaxation delay) of C-S-H samples at different target C/S molar ratios ranging from 0.81 to 2.4 mol/mol. The spectra are obtained for samples hydrated for 28 days.

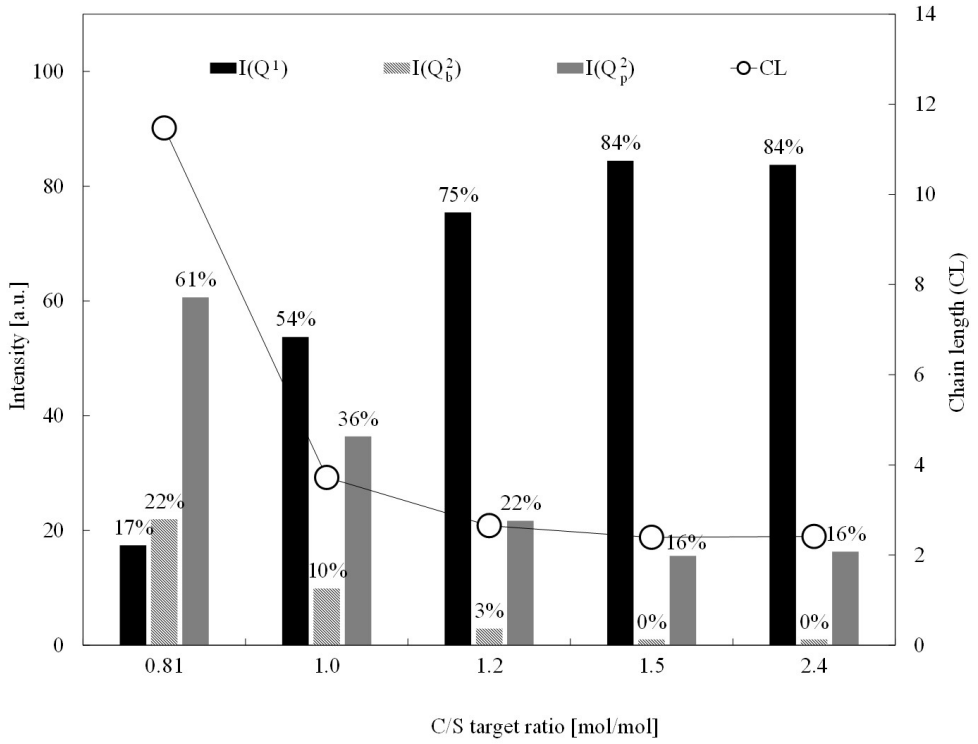

Figure 2.6: Silicate chain length (CL) of C-S-H samples at different target C/S molar ratios and relative intensities of Q^1, Q^2_b and Q^2_p sites. [Bars represent the intensity values, open circles represent the chain length value].

2.3.3 Thermo-gravimetric measurements

Results of TG measurements are given in Table 2.4. Weight loss is divided into five ranges: 25–60 °C, is the temperature range in which there is stabilisation of the nitrogen flow, 80–200 °C is the range in which evaporation of pore water and dehydration of C-S-H phase occurs, 400–460 °C, is the temperature range associated with the dehydration of portlandite and bound water loss, 560–660 °C, is attributed to the loss of CO_2 from calcium carbonate and 770–1000 °C, is attributed to the dehydration of silanol (Si–O–H) groups or transition to wollastonite for sample with target C/S ratio of 0.81 [54, 65, 66]. The temperature range chosen for calcium carbonate decomposition is lower than ranges used in other works [9, 49, 67] because we assumed carbonation has occurred at surface level in the form of amorphous calcite, which is confirmed by the absence of crystalline poly-morphs of $CaCO_3$ in the XRD patterns. TGA/DSC curves for the synthetic C-S-H aged 1, 3, 7 and 28 days are shown in Figure 2.7

(*top*) and TGA/DSC curves for the synthetic C-S-H with C/S target ratio of 0.81, 1.0, 1.2, 1.5 and 2.4 are presented in Figure 2.7 (*bottom*). Increasing the C/S ratio increases the total mass loss, in accordance with Garbev et al., (2008) [54]. DSC curves show two major endothermic peaks (respectively at 150–200 °C and 400–500 °C) and one exothermic peak at 800–850 °C. The first broad endothermic peak is associated with the dehydration of C-S-H gel [68, 54]. The area of this peak increases with ageing and decreases with increasing C/S target ratio. At the higher C/S ratios the C-S-H content is much less, as confirmed by XRD semi-quantitative analysis. The second endothermic event is associated with the decomposition of portlandite [69]. The exothermic peak at *ca.* 820 °C is due to the loss of chemically bound water and OH groups and transition to wollastonite for sample at target C/S of 0.81 [70, 39, 66]. By increasing the C/S ratio of the sample, a clear shift of this peak toward higher temperatures is observed, and it becomes a broad hump at C/S target ratio of 2.40 mol/mol, where the most amount of water is chemically bound to calcium to form portlandite. This effect is compensated by the endothermic peaks at 400–500 °C, becoming sharper and well defined at higher C/S ratios.

Table 2.4: Thermogravimetric results for each sample indicated as total weight loss, and weight loss in each thermal step.

		weight loss									
Sample	weight	total		25–60 °C		400–460 °C		530–650 °C		770–1000 °C	
	mg	mg	%	mg	%	mg	%	mg	%	mg	%
CSH-0.81_1d	14.9	2.79	18.73	0.21	1.38	0.36	2.39	0.21	1.43	0.075	0.50
CSH-0.81_3d	15.4	2.61	16.98	0.29	1.87	0.15	1.00	0.14	0.90	0.032	0.21
CSH-0.81_7d	24.2	4.92	19.93	0.61	2.50	0.27	1.12	0.23	0.92	0.064	0.26
CSH-0.81_28d	14.4	2.37	16.75	0.16	1.11	0.07	0.001	0.10	0.71	0.038	0.26
CSH-1.00_28d	15.8	2.73	17.28	0.16	1.00	0.03	0.16	0.18	1.14	0.043	0.27
CSH-1.20_28d	21.9	3.92	17.88	0.24	1.08	0.14	0.63	0.31	1.41	0.055	0.25
CSH-1.50_28d	14.2	2.67	18.80	0.24	1.72	0.02	1.16	0.19	1.31	0.048	0.34
CSH-2.40_28d	22.4	4.35	19.43	0.13	0.59	0.96	4.30	0.26	1.16	0.14	0.62

By increasing the target C/S ratio of the paste, formation of portlandite is observed. The actual C/S ratio of the C-S-H produced for each sample was calculated following the methodology developed by Garbev et al., (2008) [54]. From Table 2.4 the corrected weight loss (CWL) in mg is calculated as the difference between the bulk weight loss (BWL) (in mg),

and the amount of CO_2 (in mg) in the temperature range 530–650°C using equation 2.2:

$$CWL = BWL - CO_2 \tag{2.2}$$

Using equation 5.2, the weight loss in the temperature range of 400–460°C, $WL_{[400-460]}$ is calculated as a percentage of the BWL. This value represents also the $Ca(OH)_2$ content (wt.%) in the original sample. Thus the portlandite content (in mg) is calculated with the *tangent method*, and indicated as a percentage of the sample weight (SW) using equation 2.3.

$$WL_{[400-460]}(wt.\%) = \frac{WL_{[400-460]}}{BWL} \cdot 100 \tag{2.3}$$

$$Ca(OH)_2(mg) = \frac{SW}{100} \cdot WL_{[400-460]}(wt.\%) \tag{2.4}$$

From the stoichiometric ratios of the reaction $CaO+H_2O \longrightarrow Ca(OH)_2$ the moles (n) of CaO are calculated using equation 2.5 and the mass (in mg) of CaO using equation 2.6:

$$n_{CaO} = n_{Ca(OH)_2} = \frac{m_{Ca(OH)_2}}{M_{Ca(OH)_2}} \tag{2.5}$$

$$CaO_{[400-460]}(mg) = n_{CaO} \cdot M_{CaO} \tag{2.6}$$

where $m_{Ca(OH)_2}$ and $M_{Ca(OH)_2}$ are respectively the mass (in mg) and the molar mass of calcium hydroxide (74.093 g mol^{-1}) and M_{CaO} is the molar mass of calcium oxide (56.0774 g mol^{-1}). Using equation 2.6 it is possible to calculate moles of CO_2 from the mass loss value, $WL_{[530-650]}$, (in mg) given in table 2.4 for the temperature range 530–650°C. From the stoichiometric ratios of the reaction in equation 2.7:

$$CaO + CO_2 \rightarrow CaCO_3 \tag{2.7}$$

the mass of $CaCO_3$ (in mg) and the corresponding percentage in the total sample were calculated, respectively using Equations 2.9 and 2.10. Combining equations 2.8 and 2.5, it is then possible to calculate the amount of $CaO_{[530-650]}$, in mg, in the temperature range of calcite decomposition.

$$n_{(CO_2)} = \frac{WL_{[530-650]}}{M_{(CO_2)}} = n_{CaCO_3} = n_{CaO_{[530-350]}} \tag{2.8}$$

$$m_{CaCO_3} = n_{CaCO_3} \cdot M_{CaCO_3} \tag{2.9}$$

$$CaCO_3(wt.\%) = \frac{m_{CaCO_3}}{SW} \cdot 100 \tag{2.10}$$

where m_{CaCO_3} is the mass of calcium carbonate (in mg), M_{CaCO_3} and M_{CO_2} are respectively the molar masses of calcium carbonate (100.0869 g mol^{-1}) and carbon dioxide (44.01 g mol^{-1}). The total *[CaO+SiO_2]* mass (mg) with a target C/S molar ratio is calculated using Equation 2.11:

$$[CaO + SiO_2] = SW - CWL \tag{2.11}$$

The target C/S molar ratio is defined as:

$$C/S = \frac{CaO/M_{CaO}}{SiO_2/M_{SiO_2}} \tag{2.12}$$

where M_{SiO_2} is the molar mass of silicon dioxide (60.08 g mol^{-1}) and CaO and SiO_2 are respectively the total mass content (in mg) of calcium oxide and silicon dioxide in the starting mixing. We solved the following system of linear equations, where variables CaO^* and SiO_2, are the total masses (in mg) of calcium oxide and silicon dioxide respectively:

$$\begin{cases} CaO^* + SiO_2 = SW - CWL \\ C/S = \frac{CaO^*}{M_{CaO}} \cdot \frac{M_{SiO_2}}{SiO_2} \end{cases}$$

In order to calculate the $\overline{\text{C/S}}$ molar ratio (equation 2.14) as the difference between the total calcium oxide CaO^* in the system and the relative calcium oxide content (in mg) in portlandite and calcite temperature ranges, the actual mass content (in mg) of calcium oxide $\overline{\text{CaO}}$ reacting with SiO_2 to form C-S-H was obtained using equation 2.13.

$$\overline{\text{CaO}} = CaO^* - CaO_{[400-460]} - CaO_{[530-650]} \tag{2.13}$$

$$\overline{\text{C/S}} = \frac{\overline{\text{CaO}}/M_{CaO}}{SiO_2/M_{SiO_2}} \tag{2.14}$$

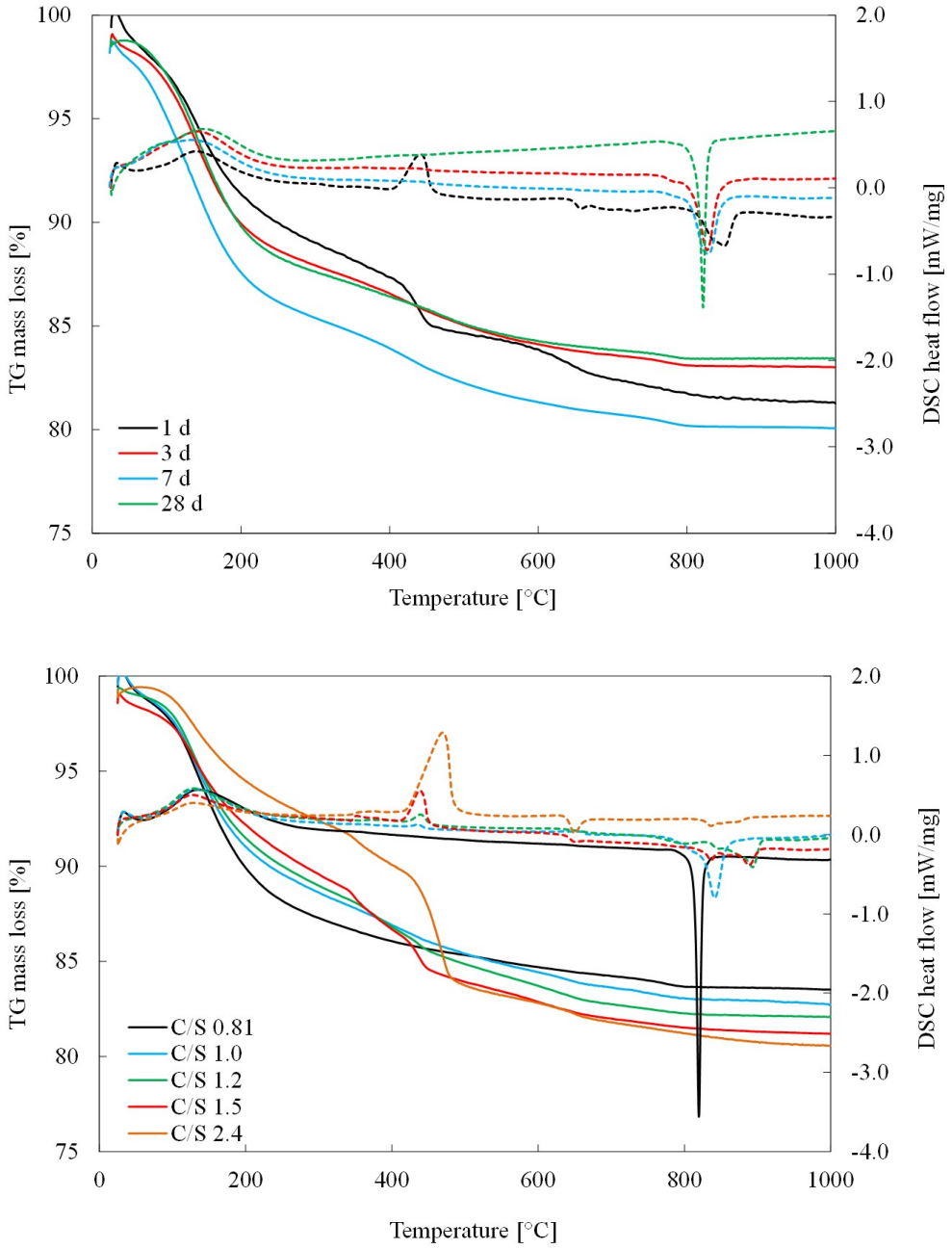

Figure 2.7: Thermal curves of sample at C/S ratio of 0.81 mol/mol at different ages (*top*) and samples cured for 28 days at different target C/S ratios (*bottom*). [TG curves: solid lines. DSC curves: dashed lines].

The calculated (measured) $\overline{\mathrm{C/S}}$ ratio for each sample is shown in Table 2.5 along with the target C/S ratio. Samples with a C/S target ratio of 0.81 aged 1 day show a well-defined step over the portlandite range and have an actual $\overline{\mathrm{C/S}}$ ratio of 0.55. This value increases with curing time to a final value of 0.79. Increasing the target C/S ratio results in precipitation of portlandite and corresponding mass loss in the TGA curves, as shown in Figure 2.7. The mixture ratios in the target range 0.81–1.00 are ideal to form pure C-S-H without precipitation of portlandite after only three days of ageing. Their final measured $\overline{\mathrm{C/S}}$ ratio lies in the range 0.79–0.95. The target and measured C/S molar ratios at 28 days are given in Table 2.5. Calculated C/S ratio for samples with target C/S ratio greater than 1.2 mol/mol are not pure C-S-H but rather a complex system of C-S-H + portlandite, as shown in the previous X-ray diffractograms and confirmed by NMR measurements. However, discrepancies between semiquantitative XRD and TGA results, in addition to the difference between calculated C/S compared to the one of the starting mixing, suggest that the reaction is not complete and some of the silica may not have reacted with the calcium present. Pure C-S-H at high C/S ratios can be achieved using a dedicated reactor and precise stoichiometry coupled with thermodynamic calculations [47]. Target C/S ratio values compared to measured $\overline{\mathrm{C/S}}$ ratio are plotted in Figure 2.8. A linear relationship between target C/S ratio and measured $\overline{\mathrm{C/S}}$ molar ratio is observed. The best fit regression line for the data is given by (equation 2.15):

$$\overline{\mathrm{C/S}} = 0.5967 \cdot C/S + 0.3589 \tag{2.15}$$

C-S-H with high C/S ratio ($\geq$ 1.3 mol/mol) is most commonly found in hydrated Portland cement rather than synthetic C-S-H, until very recent research [47] has produced pure, single phase C-S-H with C/S ratio of up to 2 mol/mol. Here, high initial C/S ratio (2.4 mol/-mol) leads to formation of C-S-H (at C/S ratio of 1.88 mol/mol) intermixed with crystalline portlandite, as shown by semi-quantitative XRD analysis (Figure 2.3). The elevated final C/S ratio coupled with the increased crystallinity of portlandite supports the capacity of C-S-H to adsorb ions and co-exist with portlandite [63, 60].

Other models based on linear regression are obtained by complementing experimental data with Bogue calculation values or TEM-EDX measurements [71, 72, 63, 73]. However, the

model presented here shows an excellent correlation between measured $\overline{C/S}$ ratio and target C/S ratio ($R^2 = 0.9908$). This feature will be very useful in predicting the actual $\overline{C/S}$ ratio from a starting mixture of raw materials.

Table 2.5: Summary of the target and calculated C/S molar ratios from thermo-gravimetric analysis

Sample	Target C/S ratio mol/mol	Calculated $\overline{C/S}$ ratio mol/mol
CSH-0.81_28d	0.81	0.79
CSH-1.00_28d	1.00	0.95
CSH-1.07_28d	1.07	1.02
CSH-1.20_28d	1.20	1.09
CSH-1.50_28d	1.50	1.28
CSH-2.40_28d	2.40	1.77

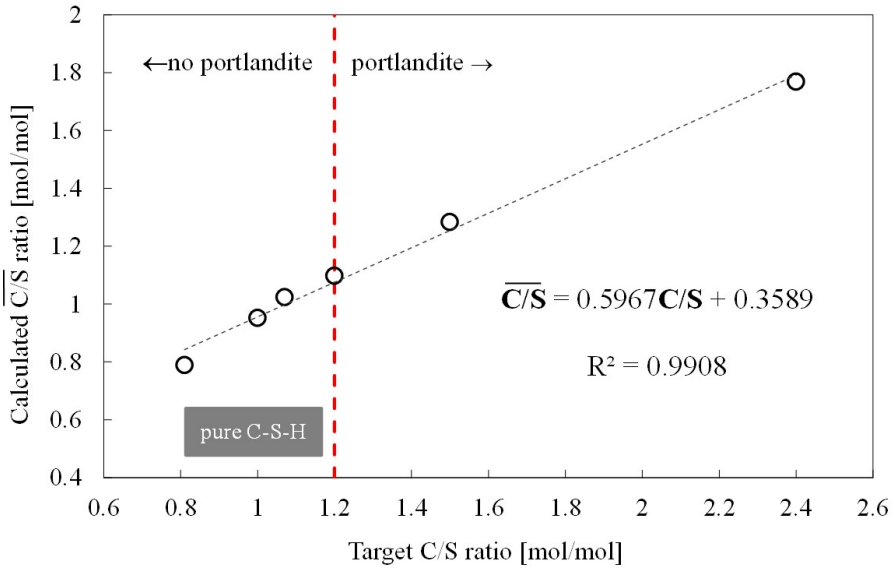

Figure 2.8: Calculated $\overline{C/S}$ molar ratio values plotted as a function of the target C/S ratio of samples aged 28 days.

2.3.4 SEM analysis

The pore structure of synthetic C-S-H is different from C-S-H phases found in hydrated Portland cement. Scanning electron microscopy images show a very porous structure, which reflects the low density of the synthesised material (Figure 2.9 *top*). EDX analysis confirmed the presence of C-S-H phases. Plate-like C-S-H structures were observed in all the samples

after 28 days of curing (Figure 2.9 *bottom*), similar to those described in Grangeon et al., (2013) [56]. As confirmed by XRD analysis, the high reactivity of nano-silica in a calcium environment produces a more ordered structure similar to tobermorite. An example of tobermorite with a plate-like structure is given in Figure 2.10 (*top*) and Figure 2.10 (*bottom*) (images extracted from Ioannou et al., (2008) [74], which show the structure of 11 Å tobermorite, the main phase present ($> 97\%$) in commercial autoclaved aerated concrete (AAC). C-S-H produced with this method present a foil-structure morphology similar to tobermorite found in autoclaved concrete, rather than needle/acicular morphology, normally found in hydrated Portland cement. The method presented in this chapter can achieve a similar micro-structure but does not require autoclaving and is suitable for large scale batch mixing. C-S-H formed during hydration of OPC at room temperature presents a needle/acicular morphology, whereas synthetic C-S-H usually forms in plate/foil structures [75].

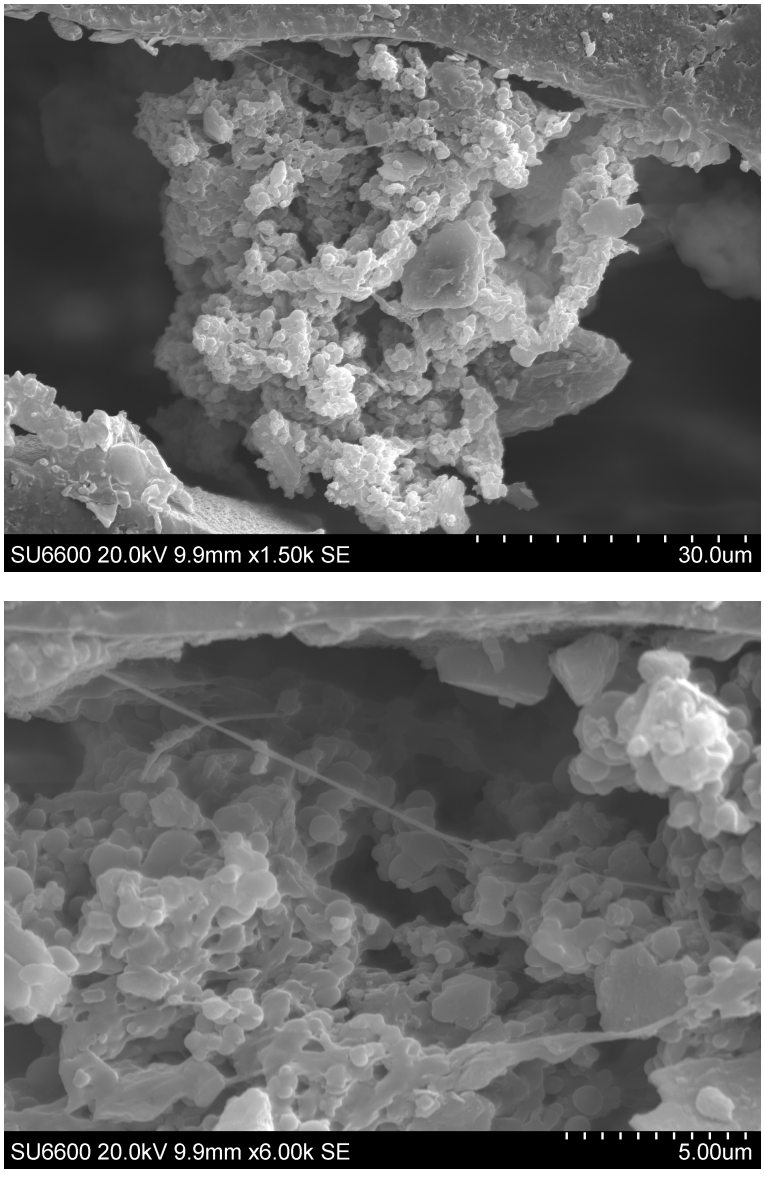

Figure 2.9: SEM image of sample CSH-0.81 at 28 days (*top*) and magnification of SEM image of sample CSH-0.81 at 28 days (*bottom*). C-S-H phase with plate-like structure.

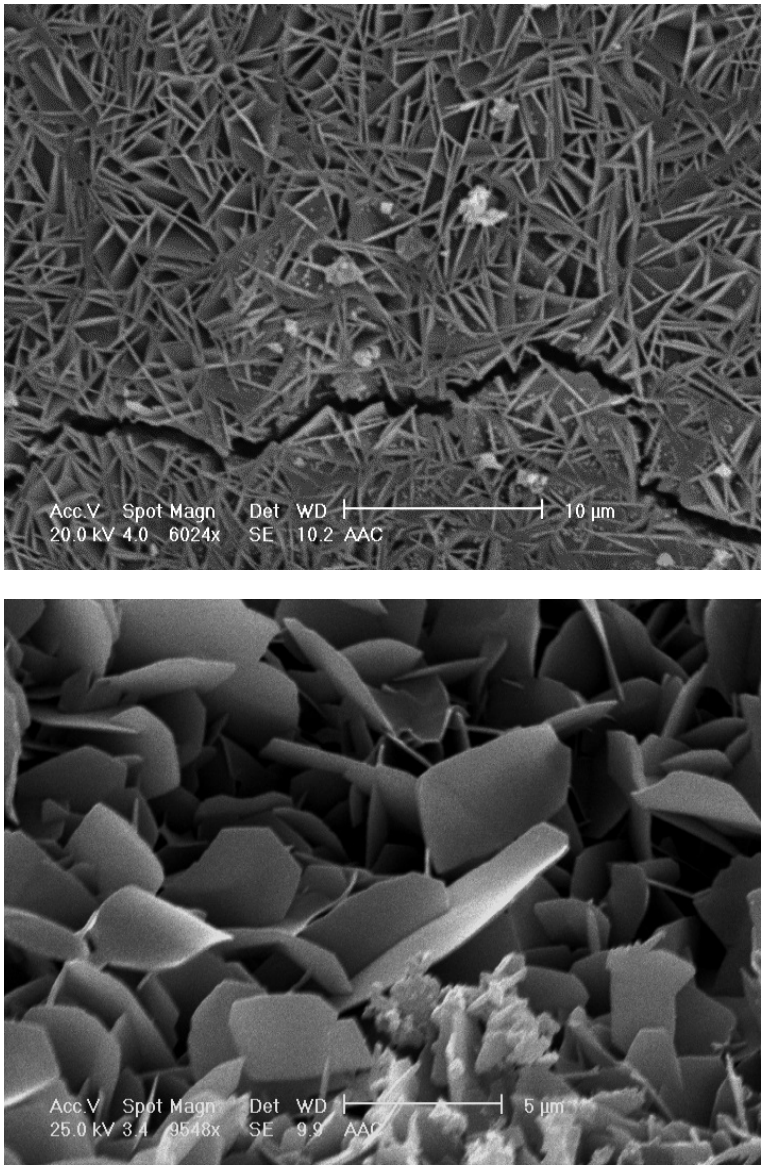

Figure 2.10: SEM image of tobermorite from aerated autoclaved concrete material (*top*) and magnification (*bottom*). Images from Ioannou et al., (2008).

2.4 Conclusions

A novel method for synthesising pure and solid C-S-H phases have been presented. C-S-H was prepared by mixing a dry source of calcium and aqueous nano-silica suspension with deionised and decarbonated water, manually and without further chemical processing, providing a simple, fast and inexpensive method for producing pure and solid C-S-H. Experiments were performed over a range of nominal C/S ratios of 0.81–2.40 mol/mol and at curing stages of 1, 3, 7 and 28 days. A combined nitrogen-solvent exchange drying method was used to dry the samples, preserving the pore structure and preventing surface carbonation. XRD characterisation showed that pure C-S-H phase formed after only 3 days, which was confirmed by TG analysis. The lower limit of measured C/S ratio was 0.68 mol/mol after 3 days of curing, starting from a C/S target ratio of 0.81 mol/mol and rising to 0.76 during 28 days curing. SEM images show the formation of C-S-H with an ordered plate-like structure similar to tobermorite, as confirmed by synchrotron XRD analysis. A linear relationship between target C/S ratio and measured $\overline{\mathrm{C/S}}$ ratio has been discovered, a useful tool to quickly calculate the actual C-S-H ratio from the target without further analytical results for the synthesis methods proposed. This processing technique is a successful approach to synthesising solid C-S-H at room temperature, from easily obtained calcium sources (calcium hydroxide and calcium oxide) and nano-silica aqueous suspension. The synthesis process has the significant advantage of being fast (7 days curing + 1 day drying), easy to develop without further equipment or complex procedures, and short manufacturing time. Importantly, it could also be upscaled to industrial batch mixing and the product would have various applications, including the construction industry and waste-water purification technologies.

Chapter 3

Effect of silica particle size on the hydration of Calcium Silicate Hydrate investigated by thermal analysis

Abstract. Calcium silicate hydrate (C-S-H) phases are central to strength development in cement and concrete, which is the world's most produced material. In this work C-S-H is made by mixing calcium hydroxide, silica and water at different calcium to silica (C/S) ratios. Two different sources of silica, silica fume and nano-silica, are used. We therefore investigate the effect of silica particle size range on the microstructure of C-S-H by means of isothermal calorimetry and thermal analysis. Results show that C-S-H prepared using silica with the lower particle size range (5–20 nm) results in heat of hydration which is nearly 3 times higher. Phase analysis and thermogravimetric measurements revealed that pure C-S-H can be formed with nano-sized silica. TG/DSC data are used to calculate the C/S final ratio and provide a mathematical description of the kinetics of hydration.

3.1 Introduction

Increasing awareness surrounding climate change and greenhouse gas emissions has brought researchers to develop alternative materials aimed at controlling the environmental impact of manufacturing industries. Ordinary Portland cement (OPC) is responsible for *ca.* 5–7% of the total anthropogenic CO_2 emissions [22]. In recent years OPC has been partially replaced by the addition of waste by-products such as fly ash and amorphous silica [76, 77, 78, 79, 16]. Fly ash is very well established in the cement industry as an environmentally friendly replacement of OPC up to 35 wt.%, without compromising mechanical and physical properties of concrete [80]. Amorphous silica, such as silica fume and nano-silica, has also been investigated in recent years. Silica fume is a by-product of the silicon and ferro-silicon industry, with a nominal particle size range of 100–1000 nm, while commercial nano-silica is *ad-hoc* synthesised from sodium silicate using a sol-gel technique. However, recent investigations have explored the production of 'green' nano-silica from waste dunite with a comparatively lower environmental footprint [81].

Silica fume has been proven to enhance the mechanical strength of Portland cement, reduce permeability and thermal conductivity [82, 83, 79], and increase pozzolanic reactivity [84]. On the other hand, nano-silica is more effective in enhancing strength because of the additional calcium silicate hydrate (C-S-H) produced [78]. Its higher reactivity is due to the lower particle size range: its high specific surface area acts as a nucleation site for the growth of C-S-H phases [85, 86].

Thermal analytical techniques are extremely useful not only in understanding the hydration kinetics of OPC, but also in modelling the results to tailor cement paste for specific applications. Kumar et al., (2012) studied the effect of fly ash on the hydration of OPC by isothermal calorimetry and found that the addition of 20 wt.% of fly ash and 5 wt.% of $Ca(OH)_2$ accelerates significantly the hydration process [87]. Accelerating the hydration of mineral phases in OPC (i.e. alite, C_3S and belite, C_2S), influences the setting time and strength development of concrete, beneficial in some applications where those parameters have to be maximised.

Wei et al., (2012) studied TG/DSC curves of hydrated cement modified by silica fume and found that silica fume accelerates the early hydration of OPC and could stabilize the content of ettringite and therefore inhibit damage to the set OPC from delayed ettringite formation (DEF) [84]. However, when silica-fume is combined with fly ash, the overall effect is a delayed hydration [88]. Oltulu and Sahin (2014) studied the pore-structure development of cement mortars containing silica fume and other nano-powders. The addition of nano-silica resulted in an increased amount of C-S-H and other hydrated products [89]. Thermogravimetric analysis and calorimetry data have been used to determine the pozzolanic reaction of fly-ash-cement pastes and validated results were useful in establishing a model for the hydration of cement [90, 91].

Although it is possible to find many experimental studies on the beneficial effects of amorphous silica added to OPC, very little research has been conducted on the effect of silica particle size on the formation of C-S-H phase, which is responsible for early strength and hardening [8]. This is partly due to the difficulty of accurately quantifying C-S-H content when it is found among other hydrated products [8]. Nonetheless, the C-S-H formed in OPC by hydration of alite (C_3S) and belite (C_2S) is morphologically different from synthetic C-S-H. In the first case C-S-H assumes the typical needle-shape, whereas in synthetic formation it is free to grow and expand in a more ordered structure, similar to tobermorite or jennite [61].

In this work C-S-H was isolated from other mineral phases present in OPC and studied its hydration reaction by thermal analysis. We synthesised C-S-H by reacting calcium hydroxide with silica and varying the calcium to silica (C/S) ratios. The effect of the silica particle size on the hydration of C-S-H was investigated using two different silica sources: silica fume (particle size range 100–1000 nm) and nano-silica (particle size range 5–20 nm). We defined a linear relationship between silica particle size and hydration kinetics and show how the final C/S ratio of the hydrated paste can be determined.

3.2 Materials and methods

3.2.1 Materials

C-S-H phases were synthesised using reagent grade calcium hydroxide powder, aqueous suspension of nano-silica, and silica fume. Calcium hydroxide, $Ca(OH)_2$, was purchased from Sigma Aldrich (CAS number 1305-62-0). Ludox TM-50 nano-SiO_2 (CAS number 7631-86-9) with a particle size range 5–20 nm was purchased from Sigma Aldrich. Nano-silica particle size range is 5–20 nm. Powdered silica fume SF920D (Elkem Microsilica, Norway, CAS number 69012-64-2), with a nominal particle size range 100–1000 nm was used. To minimise carbonation during the mixing process, deionised and decarbonated water was used [42]. Physiochemical properties of the starting materials are reported in Table 3.1. X-ray patterns shown in Figure 3.1 demonstrate the amorphous nature of the silica fume and nano-silica particles used.

Table 3.1: Characterisation of calcium hydroxide, nano-silica suspension Ludox TM-50 (NS), and silica fume SF920D (SF)

Material	Calcium hydroxide	Nano-silica (NS)	Silica fume (SF)
Form	white fine powder	suspension in H_2O	powder
Assay	$Ca(OH)_2$: $\geq$ 95.0%	SiO_2: $\geq$ 50.0%	SiO_2: $\geq$ 90.0%
	S compounds: $\leq$ 0.1%	H_20: $\geq$ 50.0%	
	$CaCO_3$: $\leq$ 3.0%		
Anion traces	Cl^-: $\leq$ 0.03%	Cl^-: $\leq$ 0.05%	
Cation traces	Fe: $\leq$ 0.05%		
	K: $\leq$ 0.05%		
	Mg: $\leq$ 0.05%		
	Na: $\leq$ 0.05%		
	Sr: $\leq$ 0.05%		
pH at 25 °C	12.4 (slurry)	8.5–9.5	-
Particle size range (nm)	-	5-20	100–1000
Density at 25 °C (g cm^{-3})	2.24	1.40	2.2–2.3
Specific area (m^2 g^{-1})	20–41	110–150	15–30

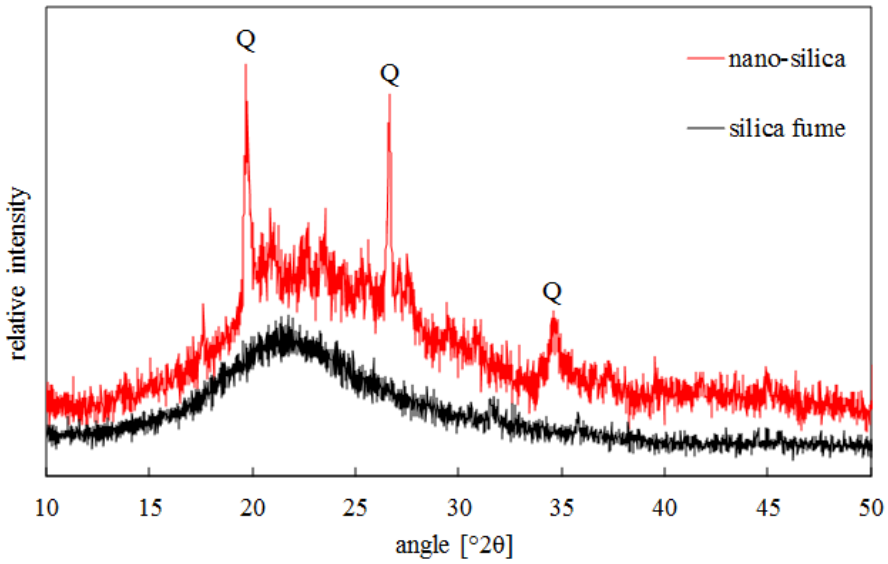

Figure 3.1: X-ray diffractogram of amorphous silica fume and nano-silica, showing single broad hump and weak quartz reflections. [Q: quartz].

C-S-H paste was manually mixed in a nitrogen environment at room temperature. Calcium hydroxide, silica (either silica fume or nano-silica) and water were mixed at a liquid to solid (l/s) ratio of 2.0. Two different calcium to silica (C/S) ratios, respectively 0.81 and 2.4 mol/mol, were investigated, as reported in Table 3.2. Specimens were cast in cubic moulds, stored in a sealed environment at 20 °C, RH 98 ± 2% and cured for 28 days. After curing, the samples were demoulded and immersed in an acetone bath for 24 hours to arrest the hydration process [49, 50] then placed in a drying chamber under a constant nitrogen flow. Solvent exchange drying method was used to preserve the micro-structure for SEM imaging and no carbonation was detected from XRD analysis [92]. All samples were then manually ground and sieved, to obtain a homogeneous fine powder for further material characterisation.

Table 3.2: Sample mixes, silica source (silica fume, SF or nano-silica, NS) and target C/S ratio.

Sample	Silica source SF or NS	Initial C/S ratio mol/mol
SF-2.4	SF	2.4
SF-0.81	SF	0.81
NS-2.4	NS	2.4
NS-0.81	NS	0.81

3.2.2 Material characterisation and thermal analysis

Powder XRD analyses were performed using a Bruker D8 Advance diffractometer with Cu K-α radiation over the range 5–60° 2θ, step size of 0.02° 2θ and 0.5 s step^{-1}. DiffracEva software from Bruker was used for XRD pattern evaluation and phase identification. Semi-quantitative analysis was carried out using Matlab, by integrating the area of the peak assigned to each mineral phase present. The samples were also characterised by Raman spectroscopy, using a Renishaw InVia spectrometer equipped with a 20 mW He-Ne laser (633 nm). Raman shifts were recorded over a 9 point map (200 × 200 μm) and wave-number range of 100–4000 cm^{-1}, using the × 20 objective lens. The exposure time was 10 s, and each spectrum was accumulated three times. Specific heat flow and heat of hydration of C-S-H paste were measured using an isothermal calorimeter (I-Cal 4000 HPC, Calmetrix). Fresh paste (*ca.* 60 g) was cast into a cylindrical container and placed into the calibrated calorimeter, at a constant temperature of 21 ± 2 °C. The heat flow was recorded over 200 hours. Samples were mixed externally, hence the first 5–10 min of detected heat flow were not taken into account for further calculations. Thermo-gravimetric (TG) and differential scanning calorimetry (DSC) data were collected using a NETSZCH STA 449 F1 Jupiter. Measurements were conducted on 10–20 mg powder samples, under constant nitrogen flow at a heating rate of 10 °C min^{-1} from 25 °C to 1000 °C. Results are plotted as mass loss (%) and heat flow (mW mg^{-1}) as a function of the temperature (°C). TG measurement results were also used to calculate the final C/S molar ratio of the samples, according to the methodology reported in *Chapter 2*.

3.3 Results and discussions

3.3.1 XRD characterisation and Raman spectroscopy

XRD analyses on all the samples showed mainly portlandite and semi-crystalline C-S-H, reported in Figure 3.2. The diffractograms show similar peak positions to C-S-H(I) [54]. XRD patterns of C-S-H samples made at the higher C/S ratio (2.4 mol/mol) revealed the presence of crystalline portlandite (reflections at *ca.* 18°, 28°, 34°, 47°, 51° and 55° 2θ), and broad humps

at 29° and 32° 2θ, reflections typical of C-S-H. Diffractograms of samples mixed at C/S ratio of 0.81 mol/mol showed the presence of portlandite when silica fume is used, while pure C-S-H is obtained when nano-silica is used. Semi-quantitative XRD analyses show that samples prepared at C/S ratios of 2.4 mol/mol using nano-silica have a lower content of portlandite than samples with the same target C/S ratio but made with silica fume, as described in Figure 3.3. This is because of the smaller particle size and higher specific surface area of nano-silica, which provides more nucleation sites for the formation of C-S-H and dissolution of portlandite. At high C/S ratio (2.4 mol/mol), although portlandite is present in both samples, the phase content of C-S-H in NS samples (*ca.* 59%) is nearly double that of SF samples (*ca.* 32%), as shown in Figure 3.3. The Raman spectra of the samples are reported in Figure 3.4. The first low frequency bands in the range 200–325 cm^{-1} correspond to the Ca-O lattice vibrations in calcium compounds (carbonate and hydroxide), while the band in the range 325–380 cm^{-1} is due to the Ca-O lattice vibrations in C-S-H gel and portlandite [94, 95]. The latter (at 350 cm^{-1}) is stronger in samples at high C/S ratio, and shouldered by Ca-O vibration in C-S-H band (at 327 cm^{-1}) in sample NS-2.4. The peak in the domain 440–480 cm^{-1} can be attributed to the internal deformation of SiO_4^{4-} tetrahedra, and is detected only in samples made with nano-silica. The strong peak in the range 660–670 cm^{-1} is assigned to bonding Q^2 tetrahedra, indicating a higher degree of polymerisation and present only in the samples made with nano-silica, suggesting the higher reactivity of nano-silica in producing C-S-H with a tobermorite structure, and more C-S-H content as confirmed by semi-quantitative XRD. The band at 850–1015 cm^{-1} can be assigned to the symmetric stretching of SiO_4^{4-} tetrahedra in Q^1 and Q^2 dimers and chains. The band at 1070–1090 cm^{-1} is the symmetric stretching of CO_3^-, visible in samples with C/S ratio of 2.4 mol/mol, while the bands at approximately 1600 cm^{-1} and 3300 cm^{-1} are characteristic of water H-O-H bending and O-H stretching respectively [96, 97]. The high calcium content sample, NS-2.4, appears to have a smaller and broader Si-O-Si Q^2 vibration compared to NS-0.81. Partly this is due to the formation of portlandite which has a broad band centred at c. 675 cm^{-1} compared to the sharp C-S-H band at c. 680 cm^{-1} but also due to the presence of Q^1 silicate dimers. Garbev et al., (2007) found that samples with C/S $\geq$ 1.0 had band broadening due to a lower degree of polymerisation which

is further confirmed by the broader and smaller band of NS-2.4 and SF-2.4 [95]. The lower C/S ratio of NS-0.81 produces a more tobermorite-like structure (shown in Figure 3.4). The Ca-O bonds in samples SF-2.4 and NS-2.4 appear to be weaker and more easily affected by air-exposure, resulting in the formation of carbonated products on the air-exposed surface of the sample (peaks at 240–280 and 1070–1090 cm^{-1}). Moreover, samples prepared with nano-silica have a Raman spectrum more comparables to tobermorite than those prepared with silica fume [96].

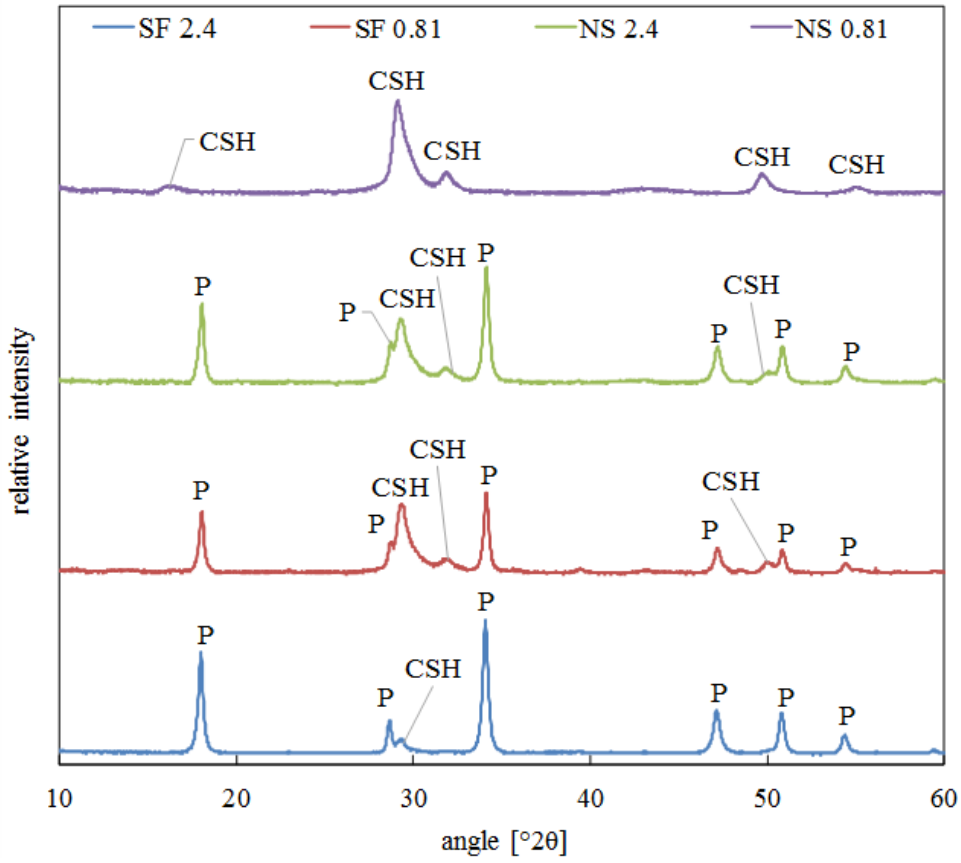

Figure 3.2: XRD patterns of samples obtained reacting silica fume (SF) or nano-silica (NS) with calcium hydroxide. [P: portlandite reflections; CSH: calcium silicate hydrate reflections].

3.3.2 Isothermal calorimetry and thermal analysis

Figure 3.5 shows the heat flow development of the samples measured by isothermal calorimetry. The first peak (I) appears at the very beginning of the measurement for all the samples, as

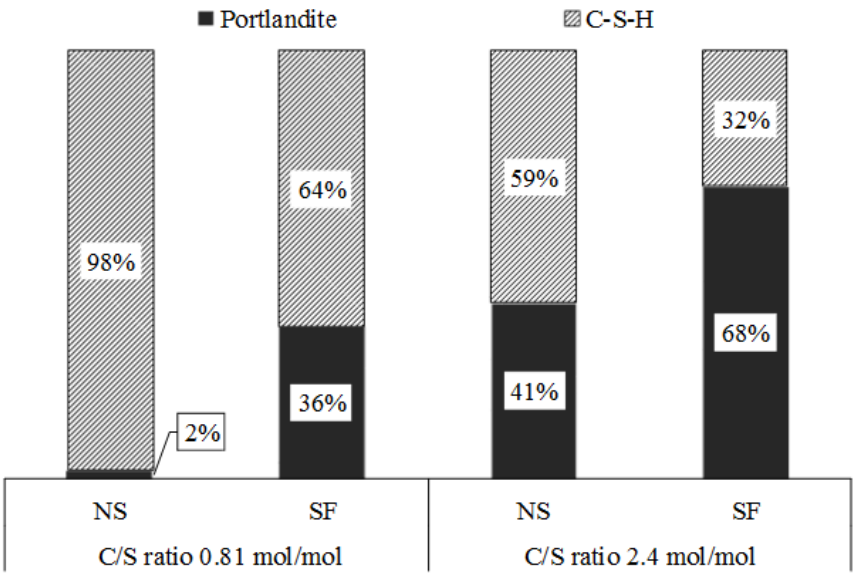

Figure 3.3: Semi-quantitative analysis of samples made using either silica fume (SF) or nano-silica (NS) at calcium to silica (C/S) ratio 0.81 and 2.4 mol/mol.

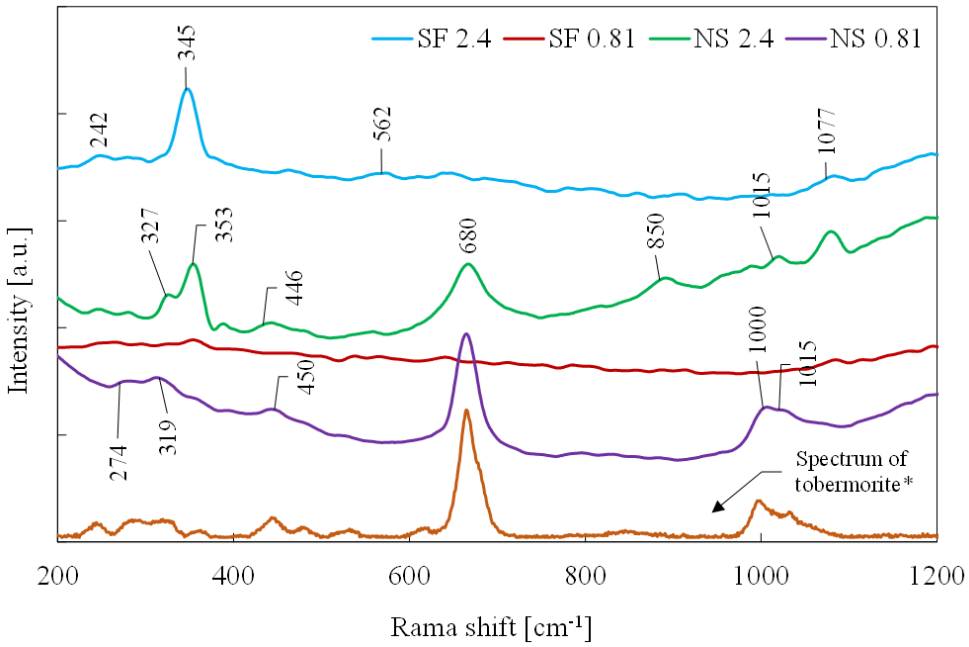

Figure 3.4: Raman spectra of the samples. [*Raman spectrum of tobermorite, RRUFF ID R060147.2].

shown in Figure 3.5A; it corresponds to particle wetting and dissolution, the chemical reaction which leads to the formation of hydrated phases. It reaches its maximum within 5 min, irrespective of the silica source used or C/S ratio, which is the typical rate of heat evolution in cementitious system [87]. The second peak (II) is the induction period and appears after 15-25 hours of hydration for samples NS-0.81 and NS-2.4. The induction period corresponds to the polymerisation of dissolved species into new crystal structures. The greater particle size of silica fume inhibits the formation of C-S-H and therefore acts as a retardant, but a weak broad peak is detected after ca. 50 hours of hydration for sample SF-0.81, while SF-2.4 converges into a straight line. This is in agreement with the semi-quantitative XRD data, where samples with silica fume have the lowest content of C-S-H. Calculations of the cumulative heat released over 200 hours are shown in Figure 3.6. Samples mixed using nano-silica at C/S 0.81 mol/mol have the highest total heat, ca. 230 J g^{-1}, in agreement with literature values for Portland cement and alite [98, 99, 100].

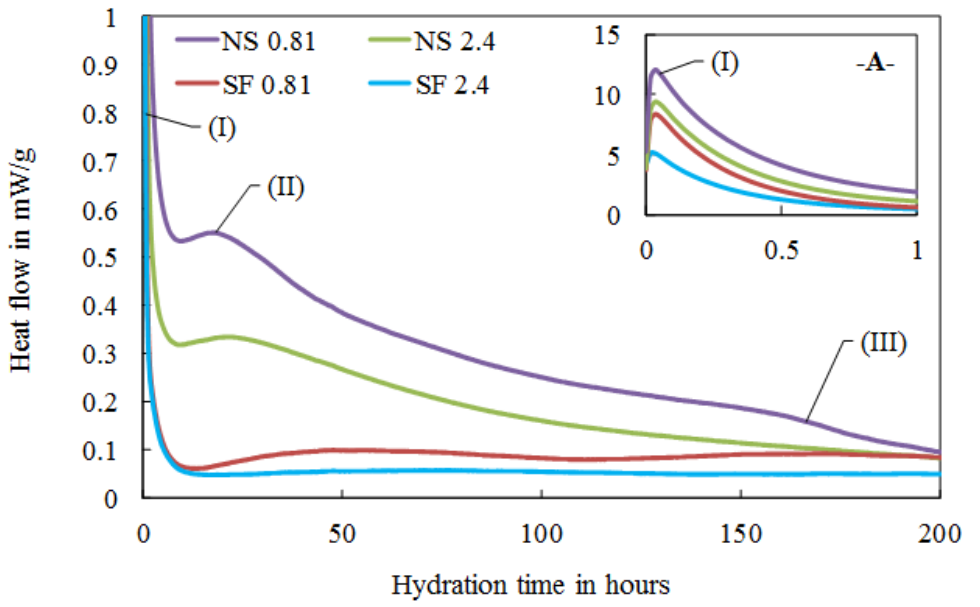

Figure 3.5: Heat flow measured by isothermal calorimetry over a hydration time of 0–200 hours and (-A-) magnification of the range 0–1 hours. (I) the initial period, (II) the induction period, (III) the acceleration period. Increasing the C/S ratio retards the second maximum in heat evolution (II) at ca. 30 h, which is retarded further in samples made with silica fume, at ca. 50 h.

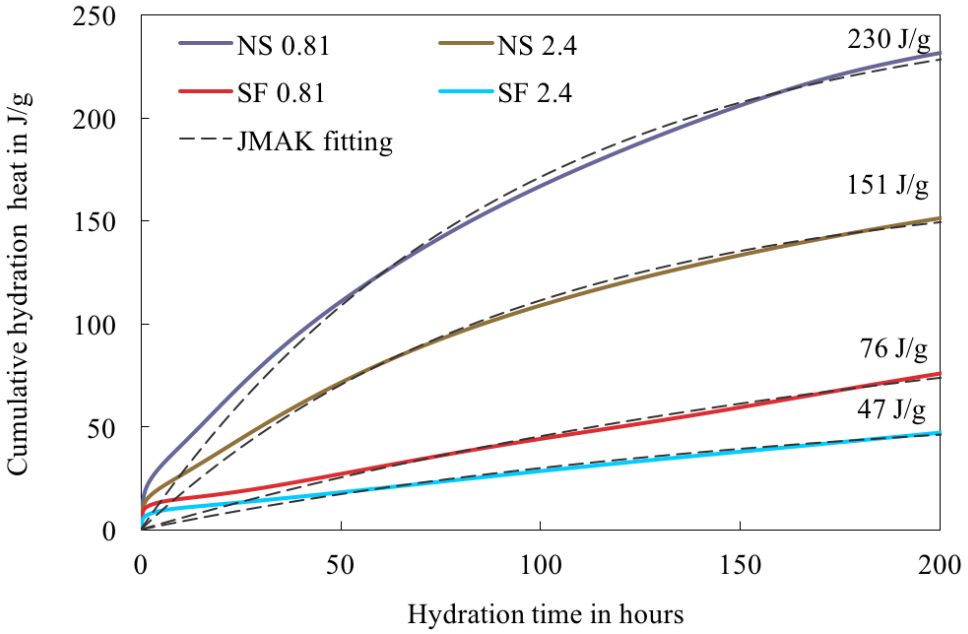

Figure 3.6: Cumulative heat release in the first 200 hours of reaction, calculated from heat flow curves.

The heat of hydration is an important parameter, relevant to different applications such as curing temperature, reactivity with other compounds and mechanical durability. Predicting the hydration kinetics has been of interest over the past 50 years and several models and simulations have been proposed. The JMAK equation based on nucleation and growth kinetics [101, 102, 103], was extensively used to model the formation of C-S-H in Portland cement hydration and tricalcium silicate (C_3S) hydration, until further improvements led to a better fit of hydration kinetics data. Assuming a constant nucleation rate and growth rate, with adequate morphological considerations, the JMAK equation can be derived into the so called boundary nucleation and growth (BNG) model [104], which is very well suited to fitting $CaCl_2$ accelerated C_3S hydration, but not pure C_3S or Portland cement. In recent years mathematical models have been coupled with hydration simulations to accurately simulate the complex hydration kinetics as well the microstructural development, strength and porosity. It is worth mentioning the Jennings and Johnson microstructure simulation model [105], in which for the first time it was attempted the 3D representation of Portland cement particles and distribution upon hydration as a function of time, incorporating some mechanistic aspects. Later, van Breuguel

developed a 3D microstructure simulation called HYMOSTRUC (HYdration, MOrphology, and STRUC development) [106]. Like the Jennings and Johnson simulation model, HYMOSTRUC does not account for phase chemistry, calcium to silica ratio or initial particle size of the C_3S or C_2S. Other simulation models (CEMHYD3D and HydratiCA) include the 3D digitisation of cement paste images into a cubic lattice [107], or the direct simulation of dissolution, diffusion and nucleation of new phases respectively using probabilistic rules to simulate microstructural changes [108]. While more recent simulation models such as μic [109] are suited to investigate the effect of particle size at the microstructure level, they do not account for solution phase chemistry.

In this paper we focused simply on a mathematical model that describes and predicts the formation of C-S-H from the reaction of a binary mix of calcium hydroxide and silica, accounting for the silica particle size and the initial stoichiometry (i.e. C/S ratio). While the models aforementioned are derived from experimental data of hydration of Portland cement paste or C_3S, here we propose a model purely for describing the hydration kinetics of a much simpler system, where only C-S-H and portlandite are formed. Hence, the cumulative heat released shown in Figure 6.4 can be described by the JMAK equation as shown in equation 3.1:

$$X(t) = 1 - e^{-(kt)^m} \tag{3.1}$$

where *X(t)* is the volume fraction that has hydrated at time t, k is a combined rate constant that includes the rates of growth and nucleation, and m describes the rate control and the crystal morphology [90]. The equation describes adequately the nucleation and growth reaction and fits calorimetry data quite well [110, 111, 112], in the case of pure C-S-H. However, in the JMAK equation there are no specific parameters which account for the effects of particle size, specific surface area, and the stoichiometric C/S ratio on the hydration kinetics [8, 90]. Nevertheless, the equation can still be used to account for the effect of particle size coupled with the C/S ratio, given the following assumptions:

- phase boundary kinetics is the rate controlling mechanism, rather than a diffusion controlled reaction;
- since the mixing was conducted outside the calorimeter, the first 10 min of the measure-

ment (peak I in Figure 3.5A) are not to be taken into account: hence, it is assumed that the function increases monotonically;

- particle size range and initial C/S ratio are interdependent parameters.

Based on the above assumptions, the JMAK equation for the cumulative heat of hydration (fitted for each sample and shown in Figure 6.4, dashed lines) is given in equation 3.2:

$$E(t) = \Delta \cdot (1 - e^{-k(t-t_0)^m}) \tag{3.2}$$

where *E(t)* is the cumulative heat released at time t in J g^{-1}, Δ accounts for particle size and initial C/S ratio combined, k is the rate constant, m describes the crystal morphology, fixed at 1, and t_0 is the initial measurement corresponding to particle wetting and dissolution. The coefficients of the fitting are reported in Table 3.3. The goodness of the fitting is estimated through the calculation of the correlation factor r^2, with has results in the range 0.9605–0.9918. k value is 0.01 for C-S-H made with nano-silica and 0.005 for C-S-H made with silica fume. The k value represents the rate of hydration and, as previously highlighted, nano-silica hydrates faster than silica fume, regardless of the target C/S ratio of the system. The k value can then be described as a function of the average particle size of the starting silica according to the equation 3.3:

$$k = -0.011\overline{ps} + 0.011 \tag{3.3}$$

where $\overline{ps}$ is the average particle size (0.02 μm for nano-silica and 0.5 μm for silica fume). The parameter Δ combines the effect of particle size and C/S ratio simultaneously. It is proportional to the specific surface area of the silica source and inversely proportional to the calcium content (or to the initial C/S ratio). For sample NS-0.81 and NS-2.4 Δ values are 257 and 169 respectively. For sample SF-0.81 and SF-2.4 Δ value is respectively 121 and 65. As shown in Figure 3.7 an increase of the C/S ratio (from 0.81 to 2.4 mol/mol) has a greater impact on samples made with nano-silica and their cumulative total heat of hydration: the higher reactivity of nano-SiO_2 enables the formation of C-S-H with an higher calcium content, compared to C-S-H formed with silica fume, as later discussed. In support of this, a decrease of the specific surface area (inversely proportional to the average particle size) results in a

lower Δ value, as shown in Figure 3.8, where Δ value is plotted against the average particle size of the silica source. Assuming a linear relationship and fixing one of the two variables, either $\overline{ps}$ or C/S, it is possible to calculate the Δ value as a function of the other one as reported in equations 3.4 and equations 3.5. Furthermore, applying a multi-linear regression for modelling the relationship between Δ and C/S and $\overline{ps}$, it is possible to calculate the value of Δ as a function of the $\overline{ps}$ and C/S, described in equation 3.6 and shown in Figure 3.9. The regression model gives Δ values similar to those derived from the JMAK fitting in equation 3.2, and a coefficient of multiple correlation R^2 of 0.959.

$$\begin{cases} \Delta_{NS} = -55.3C/S + 301.8 \\ \Delta_{SF} = -35.2C/S + 149.5 \end{cases} \tag{3.4}$$

$$\begin{cases} \Delta_{0.81} = -282.3\overline{ps} + 262.7 \\ \Delta_{2.4} = -216.7\overline{ps} + 173.3 \end{cases} \tag{3.5}$$

$$\Delta = 291 - 46C/S - 248\overline{ps} \tag{3.6}$$

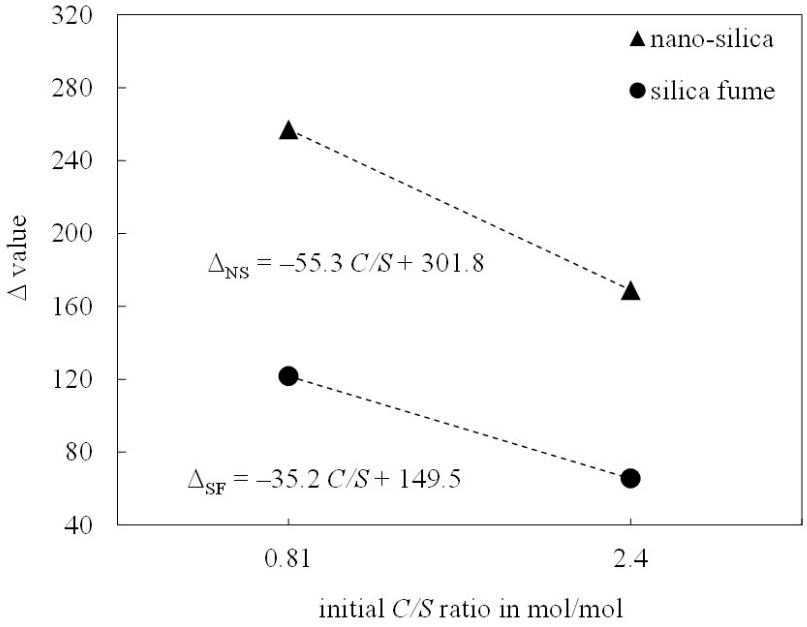

Figure 3.7: Value of Δ as a function of the initial C/S molar ratio.

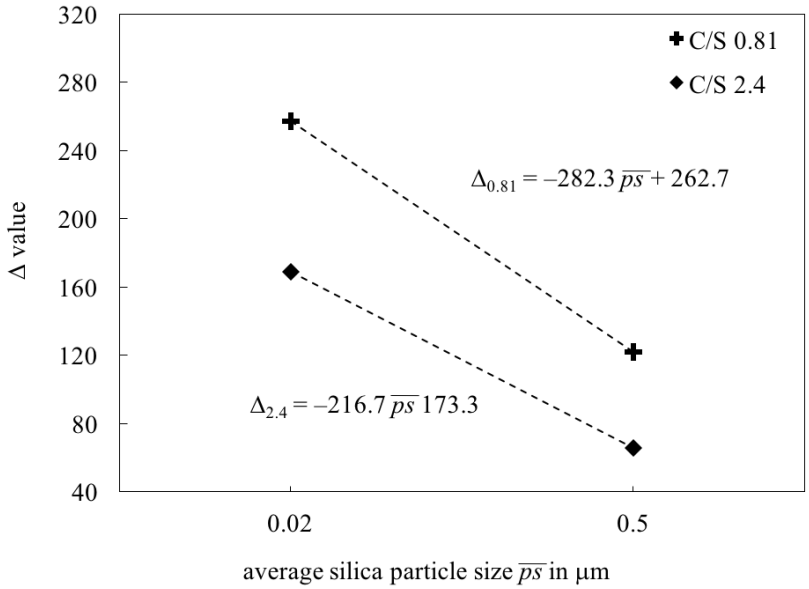

Figure 3.8: Value of Δ as a function of the average particle size of the silica source.

Table 3.3: Values of the modified JMAK model

Sample	C/S [mol/mol]	$\overline{ps}$ μm	JMAK fitting [eq. 3.2–3.3] Δ	k	r^2	Δ-model [eq. 3.6] Δ	R^2
NS-0.81	0.81	0.02	257.0	0.011	0.9918	249	0.959
NS-2.4	2.4	0.02	168.9	0.011	0.9923	176	0.959
SF-0.81	0.81	0.5	121.7	0.005	0.9715	130	0.959
SF-2.4	2.4	0.5	65.5	0.006	0.9605	57	0.959

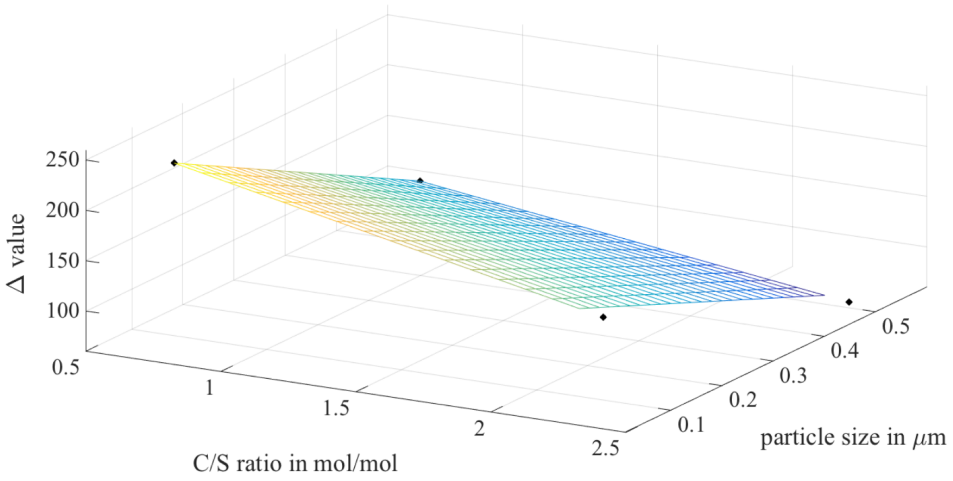

Figure 3.9: Value of Δ as a function of the average particle size of the silica source and the target C/S ratio.

TG/DSC curves of the samples are presented in Figure 3.10. Thermogravimetric curves are typical of C-S-H with a total weight loss of *ca.* 30–35%. The first thermal step is observed in the range 25–200 °C and corresponds to the evaporation of pore and capillary water and dehydration of C-S-H [54, 78]. The second weight loss occurs in the thermal step between 350–550 °C and is associated to the dehydroxylation of portlandite. The thermal step in the range 600–700 °C may be attributed to the loss of CO_2 from calcium carbonate, due to the surface carbonation of samples during instrument operations [54]. TG data and DSC responses are summarised in Table 3.4. Samples made with nano-silica present higher C-S-H content than samples made with silica fume, with a total mass loss in the range 20–30%, proportional to the content of C-S-H and pore water. In agreement with previous semi-quantitative XRD analysis, at the same initial stoichiometric C/S ratio, nano-silica promotes the formation of C-S-H and no $Ca(OH)_2$ is detected in the mix NS-0.81. Additionally, the portlandite content, proportional to the mass loss, in %, in the range 350–550 °C, is higher in samples made with silica-fume, and is up to 12 wt.%. Differential scanning calorimetry curves show the first endothermic event at *ca.* 80 °C, corresponding to the formation of C-S-H and evaporation of pore water. The integrated peak area is greater in sample NS-0.81 (603 J g^{-1}) than sample SF-0.81 (586 J g^{-1}). Correspondingly, the endothermic event at *ca.* 430 °C, associated with the decomposition of $Ca(OH)_2$, is greater in samples with higher C/S ratio and larger silica particle size range (sample NS 2.4, 195 J g^{-1}; sample SF-2.4, 533 J g^{-1}). Furthermore, the higher C/S ratio causes a shift of the DSC peak respresenting portlandite breakdown towards higher temperature, and close to the peak centre of pure portlandite, at 460 °C, indicating an increase in degree of crystallinity of portlandite and loss of bound water (up to *c.* 550 °C). The DSC response of sample NS-0.81 exhibits a narrow exothermic peak at around 800 °C, attributed to the crystallisation of wollastonite [70, 113, 39, 66].

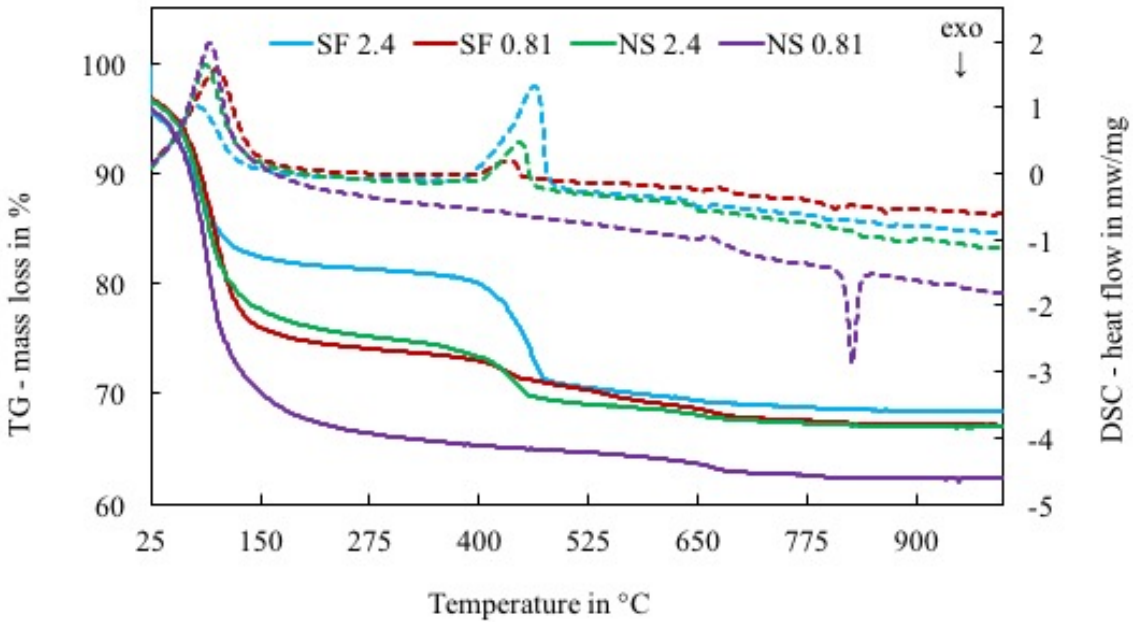

Figure 3.10: TG/DSC curves of samples obtained reacting silica fume (SF) or nano-silica (NS) with calcium hydroxide. [TG measurement in solid lines, DSC response in dashed lines.

Table 3.4: TG/DSC data for all samples. DSC peak information (peak height, centre and integrated area) and TG mass loss in the range of C-S-H (25–200 °C) and portlandite (350–550 °C). *ND: peak not detected.

Sample		Temperature range C-S-H (25–200 °C)				Temperature range $Ca(OH)_2$ (350–550 °C)			
		DSC peak			TG	DSC peak			TG
silica	C/S mol/mol	centre °C	height mW/mg	area J/g	mass loss %	centre °C	height mW/mg	area J/g	mass loss %
SF	0.81	99	1.58	586	-23	436	0.19	66.4	-4
	2.4	78	1.02	320	-14	464	1.32	533	-12
NS	0.81	93	1.99	603	-30	ND*	ND*	ND*	-1
	2.4	88	1.65	496	-21	446	0.47	195	-7

TG data were used to calculate the C/S ratio of hydrated sample (final C/S ratio), according to the methodology reported in *Chapter 2*, equations 2.2–2.14. Results are reported in Table 3.5. Using nano-silica instead of silica fume as the silica source, results in an overall higher final C/S ratio. This reflects the higher reactivity of nano-silica and its capability to form additional C-S-H and could explain the greater contribution of C/S in Δ-values. However, the lower final C/S ratio compared to the one of the starting mix suggests that the reaction is not complete and some of the silica may not have reacted with the calcium present. The C/S ratio plays a key role in the hydration kinetics of Portland cement and its strength development

[14]. In hydrated OPC, it varies in the range 0.6–2.0 mol/mol, and many authors have found that mortar and concrete pastes modified by the addition of pozzolanic nano-particles produce a denser C-S-H with a lower C/S ratio [114, 115, 116]. Results presented here show an opposite trend: smaller particles increase the C/S ratio of C-S-H. This is due to the enhancing reactivity of nano-silica compared to that of silica fume. C/S ratio is a key parameter for specific application and not only in cement industry: C-S-H can be crystallographically tailored to incorporate radionuclides or heavy metals into its structure [39, 40], or could be expanded to increase porosity and be used in waste-water treatment as an adsorbent material [117, 118]. Hence, understanding and predicting C-S-H formation and its C/S ratio in Portland cement mortar and concrete is important, especially when additional components, such as fly ash or fine silica, are added.

Table 3.5: Initial and final C/S molar ratio of samples, calculated from thermogravimetric analysis

Sample	C/S molar ratio	
	initial mol/mol	final mol/mol
SF-0.81	0.81	0.64
NS-0.81	0.81	0.79
SF-2.4	2.4	1.58
NS-2.4	2.4	1.77

3.4 Conclusions

In this work the effects of silica particle size on the C-S-H hydration kinetics are presented. C-S-H paste was synthesised using calcium hydroxide, silica and water at low and high C/S ratio, respectively 0.81 and 2.4 mol/mol. Two different sources of silica were used: silica fume (particle size range of 100–1000 nm) and nano-silica (particle size range of 5–20 nm). XRD and Raman data showed that increasing the silica particle size range resulted in precipitation of portlandite, reducing the purity of the C-S-H produced. Measured heat flow showed that silica fume decelerates the hydration, and the cumulative heat of hydration is 3 to 5 times greater in C-S-H made with nano-silica. For the first time, a kinetic model was defined to

describe the hydration of C-S-H, accounting for particle size and C/S ratio. The model fits calorimetric data and provides information to understand the stoichiometry of C-S-H based on silica particle size. We found that the rate of hydration of samples made with nano-silica is 50% greater than samples made with silica fume.

Furthermore, the stoichiometry of the starting mixing, assessed by the means of the Δ-value, has a greater impact on samples made with nano-silica ($\Delta_{NS-0.81} - \Delta_{NS-2.4} = 88$) than samples made with silica fume ($\Delta_{SF-0.81} - \Delta_{SF-2.4} = 56$). Further investigation will be conducted to validate the kinetic model proposed in multi-compound systems such as OPC-nano-silica and OPC-silica fume, and other nano-powdered additive to OPC.

Chapter 4

In-situ XRD studies on hydrothermal synthesis of Calcium Silicate Hydrate: the influence of temperature on stoichiometry

Abstract. In this study synthetic calcium silicate hydrate (C-S-H) is prepared under hydrothermal conditions at 110 °C at calcium to silica (C/S) ratios in the range of 0.81–1.5 mol/mol. *In-situ* synchrotron XRD measurements allow to investigate the influence of C/S ratio on the crystallisation rate of C-S-H. Experimental findings show that the relative high synthesis temperature (in the range of 60–110 °C) affects the final C/S ratio of hydrated C-S-H compared to that one produced at room temperature. Structural investigations also revealed that C-S-H has an anisotropic behaviour under temperature, with an expansion along the *b*-axis of *ca.* 1.2%. Furthermore, elastic properties of portlandite crystals were used to localise the excess in calcium in hydrated C-S-H structure under different C/S ratios.

4.1 Introduction

Portland cement constitutes one of most used materials in the world. It is largely employed in construction industry, in conservation and restoration operations, and ultimately in solidification/stabilisation treatment of polluted soils and immobilisation of heavy metals and radioactive waste [119, 120, 121, 122, 123]. The versatility of ordinary Portland cement (OPC) and its constituents has attracted the attention of worldwide researchers, who have attempted artificial synthesis of its hydrated compounds, particularly calcium silicate hydrate (C-S-H) phases such as tobermorite, xonotlite, wollastonite etc. In hydrated ordinary Portland cement (OPC), calcium (aluminum) silicate hydrates, C-(A)-S-H, are the most important mineral phases, responsible for early strength and hardening [8].

The mixing of cement and the environmental conditions under which it is done, have been proven to affect the physical properties and mechanical performances. Kim et al., (1998) found that an increase of curing temperature up to 40 °C resulted in an enhanced early-age compressive strength but eventually a lower later-age strength [124]. Gallucci et al., (2013) studied the chemical development of CEM I-42.5 cured at temperatures in the range 5–60 °C [125]. They found that cement cured at high temperature is higher in porosity compared to that which is cured at low temperature, due to densification of C-S-H, affecting mechanical properties and durability. These findings were recently confirmed by Bahafid et al., (2017), using a class G cement cured up to 90 °C [126]. Class G cement is widely used in the oil-well construction industry, where the temperature gradient along the depth could affect hydration and compromise the durability of the cement walls. Hydration temperature must also be taken into account in nuclear waste immobilisation. In storage and deep geological disposal, radioactive waste are disposed of at a temperature near 200 °C [127], at which major changes in the mineralogy occur [128, 129].

To better understand how temperature influences the hydration of cement, particularly the formation of C-S-H compounds, their crystallinity degree and reactivity, researchers have attempted hydrothermal synthesis of these mineral phases by varying temperature, pressure and calcium to silica (C/S) ratio. Back in the 50's Assarsson et al., (1956) investigated the

close dependency between temperature and C/S ratio and how those two parameters lead to morphologically different structures [130], later confirmed by Okada et al., (1994) using ^{29}Si NMR spectroscopy on hydrothermally formed C-S-H [131]. C-S-H was synthesised at the temperature of tobermorite–xonotlite crossover by Hartmann et al., (2015). It was found that crystallisation behaviour is highly affected by the temperature and the C/S ratio. Particularly, an increase in calcium content retarded the formation of C-S-H at 180 °C [132]. Rios et al., (2009) studied C-A-S-H hydrothermally formed at 175 °C by X-Ray diffraction and nuclear magnetic resonance. Presence of semi-crystalline C-S-H was found along with hydrogarnet and tobermorite. Kikuma et al., (2011) studied the hydrothermal formation of tobermorite by means of *in-situ* XRD measurements at temperatures up to 190 °C. It was found that although the water to solid (w/s) ratio does not influence the kinetics of tobermorite formation, the silica particle-size affects the dissolution and crystallisation curves [133]. High-energy time-resolved XRD is an extremely useful tool to understand structural changes induced by autoclaving conditions. XRD Bragg positions can be used to calculated the growth-rate of semi-crystalline C-S-H or tobermorite [128, 134, 135]. Hydrothermal synthesis process is useful for investigating alternative applications of calcium silicate phases. Tobermorite fibres were synthesised from incinerated municipal waste to produce a highly porous material (porosity in the range 0.1–10 μm) which have the potential to be used as an adsorbent material in waste-water treatment [117]. Jiang et al, (2011) investigated hydrothermally synthesised xonotlite to produce light-weight insulation materials, with thermal conductivity of 0.049 W m^{-1} K^{-1})[136].

While hydrothermal formation of crystalline calcium silicate phases (i.e. tobermorite, xonotlite, wollastonite etc...) has been investigated, little attention has been given to the formation and kinetics of semi-crystalline C-S-H and its crystal structure in hot and wet environments. The aim of this work is to provide experimental evidence of the influence of relative low hydrothermal temperature (60–110 °C) on the structure of C-S-H in the context of varying the C/S ratio. Although lab-XRD is a useful technique for semi-quantitative analysis, it is not powerful enough (*ca.* 30 keV) for rapid in-situ studies for large core samples. We used synchrotron time-resolved X-ray diffraction (higher intensity/temporal resolution and

higher energy of up to 80.845 keV) to investigate changes in C-S-H structure and define a mathematical model to predict the final C/S ratio from a given initial stoichiometry and temperature of synthesis. This is an important and useful tool to tailor the C-S-H structure to specific applications, from waste-water treatments to nuclear waste immobilisation, where high temperature will interfere with cement properties.

4.2 Materials and methods

4.2.1 Materials

C-S-H phases were synthesised using reagent grade calcium hydroxide powder and aqueous suspension of nano-silica, at set target C/S molar ratios. Calcium hydroxide (CAS number: 1305-62-0, molecular mass: 74.093 g mol^{-1}), $Ca(OH)_2$, and Ludox TM-50 nano-SiO_2 (CAS number 7631-86-9, molecular mass: 60.08 g mol^{-1}) were purchased from Sigma Aldrich (particle size range 5–20 nm). To minimise carbonation during mixing, deionised and decarbonated water were used for mixing [42]. Starting material physiochemical properties are reported in Table 4.1.

Table 4.1: Characterisation of calcium hydroxide and nano-silica suspension Ludox TM-50 used for the synthesis of C-S-H.

Material	Calcium hydroxide	Nano-silica
Form	white fine powder	suspension in H_2O
Assay	$Ca(OH)_2$: $\geq$ 95.0%	SiO_2: $\geq$ 50.0%
	S compounds: $\leq$ 0.1%	H_20: $\geq$ 50.0%
	$CaCO_3$: $\leq$ 3.0	
Anion traces	Cl^-: $\leq$ 0.03%	Cl^-: $\leq$ 0.05%
Cation traces	Fe: $\leq$ 0.05%	
	K: $\leq$ 0.05%	
	Mg: $\leq$ 0.05%	
	Na: $\leq$ 0.05%	
	Sr: $\leq$ 0.05%	
pH at 25 °C	12.4 (slurry)	8.5–9.5
Particle size range (nm)	-	5–20
Density at 25 °C (g cm^{-3})	2.24	1.40
Specific area (m^2 g^{-1})	20–41 (hydrated)	110–150

C-S-H samples were prepared according to the methodology described in *Chapter 2*. Specimens were manually mixed in a nitrogen environment at high pH-values and room temperature. Calcium hydroxide, nano-silica and decarbonated and deionised water were mixed at a liquid to solid (l/s) ratio of 2.0. C-S-H pastes were mixed at different calcium to silicate (C/S) ratios and temperatures, as reported in Table 4.2. Hydrothermal synthesis was conducted firstly in our laboratories, in order to investigate a wide range of mixes and duration of synthesis (from 3.5 to 12 hours), referred to as *ex-situ* experiments. After the synthesis, samples for TGA/DSC analysis were oven dried at 60 °C for 100 hours to remove pore water prior to TGA analysis [54]. All samples were then manually ground and sieved, to obtain a homogeneous fine powder for further material characterisation. *In-situ* XRD experiments were conducted at Diamond Light Source (UK), on C-S-H samples at two different C/S ratio and fixed synthesis temperature (110 °C). Such values of temperature where chosen to simulate environmental conditions in cement and concrete infrastructure in oil extraction or deep geological storage of low and medium-level radioactive waste.

Table 4.2: Sample mixes, target C/S ratio values (in mol/mol), synthesis duration (in hour) and temperature (in °C).

Sample	Target C/S ratio mol/mol	Time hours	Temperature °C
CSH-0.81-H	0.81	3.5	110
CSH-1.0-H	1.00	3.5	110
CSH-1.2-H	1.20	3.5	110
CSH-1.5-H	1.50	3.5	110
CSH-0.81-L	0.81	12	60
CSH-1.5-L	1.50	12	60

4.2.2 *Ex-situ* hydrothermal synthesis and characterisation

Hydrothermal synthesis was carried out using a stainless steel pressure vessel (Parr Instrument company, series 4750) with volume 29.4 cm^3, as shown in Figure 4.1. Freshly mixed paste (*ca.* 17 g) was poured into a pre-heated polytetrafluoroethylene (PTFE) liner (internal volume of 10 cm^3, 24 mm outer ⌀ and 65 mm in total length) and inserted into the vessel. The vessel was then placed into a pre-heated oven at the synthesis temperature, 60 °C or 110 °C for 12

or 3.5 hours respectively. The water pressure during synthesis was calculated to be 0.2 bar and 1.45 bar respectively at 60° and 110 °C. At the end of the synthesis, the specimen was in a solid state, and finely powdered for XRD characterisation. Powder XRD analyses were performed using a Bruker D8 Advance diffractometer with CuKα radiation over the range 5–60° 2θ, step size of 0.02° 2θ and 0.5 s step^{-1}. DiffracEva software from Bruker was used for XRD pattern evaluation and phase identification. Semi-quantitative analysis was carried out using Matlab by integrating the area of the peaks assigned to each mineral phase present [93]. Prior to thermo-gravimetric analysis, samples were dried at 60 °C for *ca.* 100 hours to remove pore water [54]. Thermo-gravimetric (TG) and differential scanning calorimetry (DSC) data were collected using a NETSZCH STA 449 F1 Jupiter. Measurements were conducted on 18–23 mg powder samples, under constant nitrogen flow at a heating rate of 10 °C min^{-1} from 25 °C to 1000 °C. Results are plotted as mass loss (%) and heat flow (mW mg^{-1}) as a function of the temperature (°C). TGA/DSC measurement results were used to calculate the actual C/S molar ratio of the samples, according to the methodology used in *Chapter 2*.

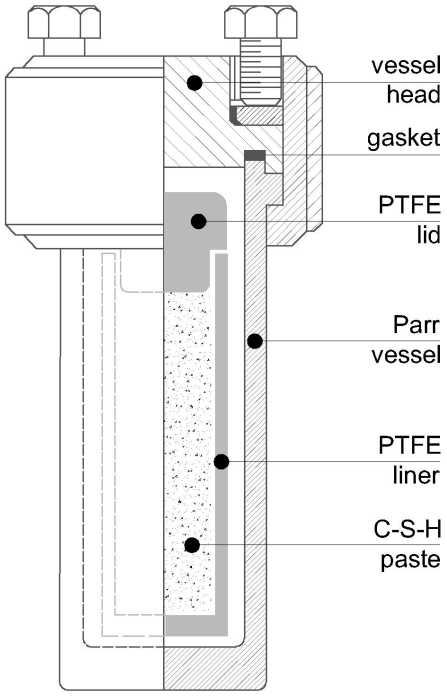

Figure 4.1: Pressure vessel used for *ex-situ* hydrothermal synthesis (Parr Instrument - part number 4750).

4.2.3 In-situ time-resolved synchrotron XRD measurement

In-situ XRD measurements were carried out at the UK synchrotron Diamond Light Source, using a 2D monochromatic high-energy beam (80.845 keV and λ=0.15336 Å) on the Joint Engineering, Environmental and Processing (I12-JEEP) beamline. The X-ray beam size was 1×1 mm^2. X-ray diffraction images were collected in transmission geometry with a large-area 2D detector (Pixium RF4343; Thales). The exposure time for collection of a single diffraction image was 60 seconds. The precise energy calibration was defined by measuring a CeO_2 standard (NIST Standard Reference Material 674b) at five various standard-to-detector distances with the relative difference of 100 mm between two detector positions following the approach of Hart et al., (2013) [137]. Then, a standard sample was measured again to calibrate absolutely the sample-to-detector distance, the orthogonality of the detector with respect to the incoming beam, and the position of the beam centre on the detector. 2D patterns were radially integrated into the Q-space to obtain intensity curves, I(Q), using DAWN software [52]. Data were then converted into the 2θ space corresponding to a laboratory Cu-anode source applying equation 4.1:

$$2\theta = 2asin\frac{Q\lambda_{Cu}}{4\pi} \tag{4.1}$$

where λ_{Cu} is 1.542 Å and Q is the Q-space value.

The heating chamber used was specifically designed for synchrotron *in-situ* experiments and built by Pascoe Engineering Ltd as shown in Figure 4.2. The chamber constitutes a heating block (120×120×110 mm) made of aluminium and equipped with six cartridge heaters (9 mm ⌀ and 90 mm in length) connected to an external controller. The inner chamber sits inside the heating block and consists of a parallelepiped of 84 cm^3, made from stainless steel, and a temperature resistant gasket and lid. The cell was tested and certified for maximum operational conditions of 6 bar and 10 hours. Two fused quartz windows (20 mm ⌀ and 2 mm in thickness) are welded onto each side-wall of the inner cell and aligned with the window holes in the heating block. Two thermocouples, J-type and K-type, are inserted into the heating block and the inner cell through the lid to monitor the temperature of the sample during the

XRD measurement. C-S-H paste was poured into a PTFE liner (15 mm ⊘, 55 mm high and 9.7 cm^3) and placed into the inner cell. The temperature of the sample was kept at 110 ± 5 °C for 3.5 hours. XRD patterns were collected every 60 seconds over the duration of the experiment.

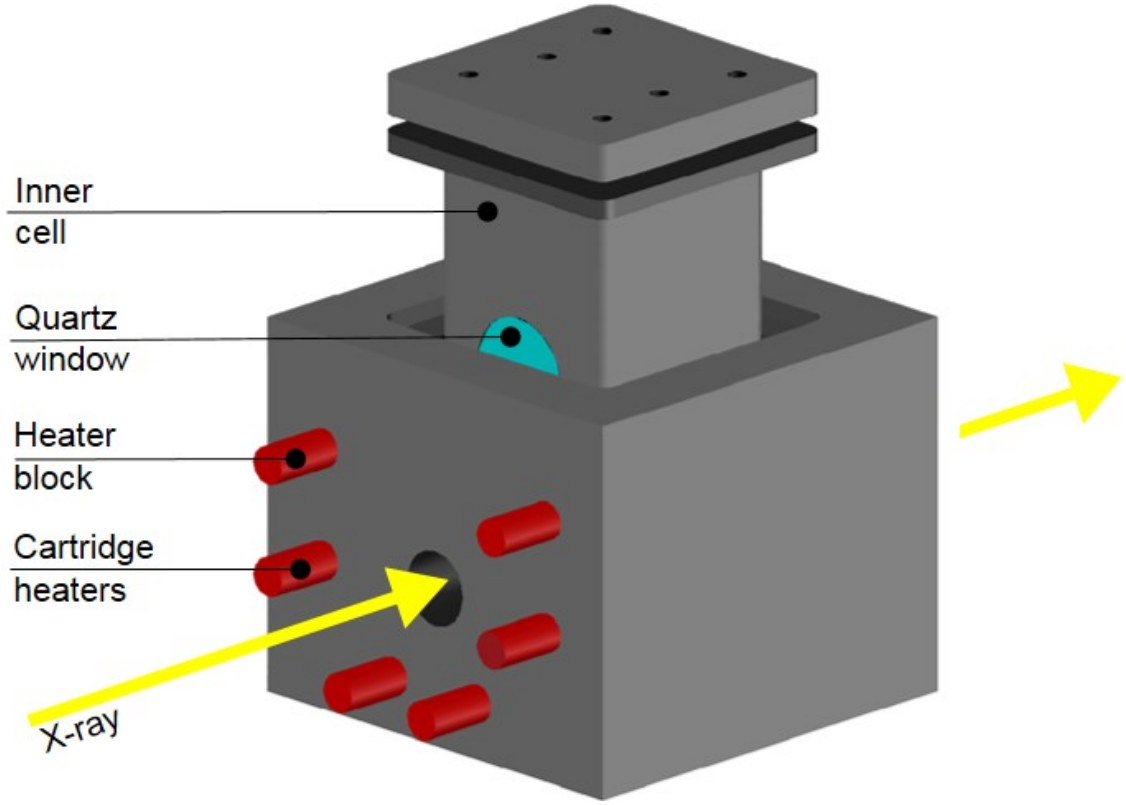

Figure 4.2: Heating chamber used for *in-situ* synchrotron XRD measurements: block with six cartridge heaters, inner cell with fused quartz windows.

4.3 Results and discussions

4.3.1 XRD characterisation and thermal analysis

Laboratory XRD measurement on the sample synthesised at 60 °C for 12 hours at target C/S ratio 0.81 mol/mol shows the formation of pure C-S-H. Broad peaks are observed in the range *ca.* 15–20° 2θ, and *ca.* 40–60° 2θ. The narrow peak at 29.5° 2θ is the main reflection of C-S-H, as shown in Figure 4.3 (*top*). At higher target C/S ratio (1.5 mol/mol) crystalline portlandite is detected (ICSD collection code 15471). Increasing the temperature of the synthesis to 110

°C while decreasing the duration (3.5 hours) results in the formation of pure C-S-H at the lowest target C/S ratios (0.81—1.0 mol/mol). An increase of the C/S ratio to higher values (1.2–1.5 mol/mol) results in broadening of the C-S-H major reflections and precipitation of portlandite, in agreement with previous studies [55, 93], and detailed in Figure 4.3 (*bottom*). The patterns show similar peak positions to C-S-H(I) [66]. Semi-quantitative XRD analysis performed on all the samples, suggests that synthesis temperature influences the formation and purity of C-S-H phases compared to those formed under ambient conditions. In previous work reported in *Chapter 2*, samples with target C/S ratio of 1.2 mol/mol show a relative content of C-S-H of 95%: increasing the temperature to 110 °C the C-S-H content decreases to 83%. Samples with target C/S ratio of 1.5 mol/mol under ambient conditions have a relative C-S-H content of 79%: it decreases to 76% and 69% respectively for synthesis at 60° and 110 °C. Values of C-S-H and portlandite (P) relative content are reported in Figure 4.4 (*top*) and 4.4 (*bottom*).

TG/DSC curves of C-S-H synthesised at 60 °C and 110 °C are presented in Figure 4.5 (*top*) and Figure 4.5 (*bottom*). Samples which have a target C/S ratio of 0.81 mol/mol are typical of C-S-H with a total weight loss of *ca.* 15%. Increasing the C/S ratio, a clear weight loss step at *ca.* 400 °C is present, corresponding to the dehydration of portlandite. The DSC response exhibits an endothermic peak associated with the dehydration of portlandite and an exothermic peak at *ca.* 800 °C, attributed to the loss of Si-O-H groups [70, 39] for samples at high C/S ratio, and to transition to wollastonite for sample at C/S ratio of 0.81 mol/mol. Samples made at target C/S ratio 0.81 and 1.0 mol/mol show no endothermic episodes regardless the synthesis temperature. Samples with higher C/S ratio (1.2 and 1.5 mol/mol) have greater overall weight loss (ca. 25%) and exhibit an additional endothermic event at *ca.* 680 °C. This is associated with traces of CO_2 released by decarbonation of amorphous $CaCO_3{\cdot}(H_2O)$, due to surface carbonation during the operation of the instrument [66, 54].

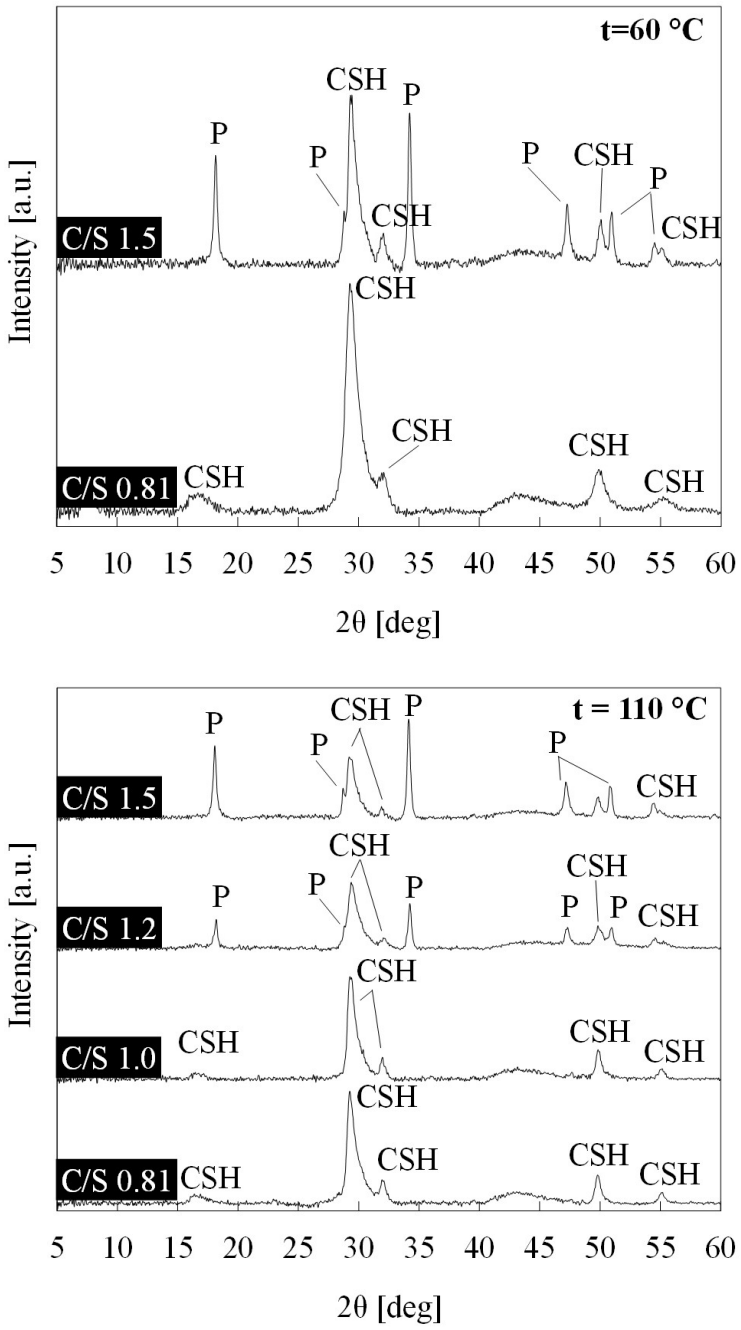

Figure 4.3: XRD patterns of samples (target C/S ratio of 0.81 and 1.5 mol/mol) synthesised at 60 °C (*top*) and samples (target C/S ratio of 0.81–1.5 mol/mol) synthesised at 110 °C (*bottom*). [P: portlandite reflection/phase; CSH: calcium silicate hydrate reflection/phase]

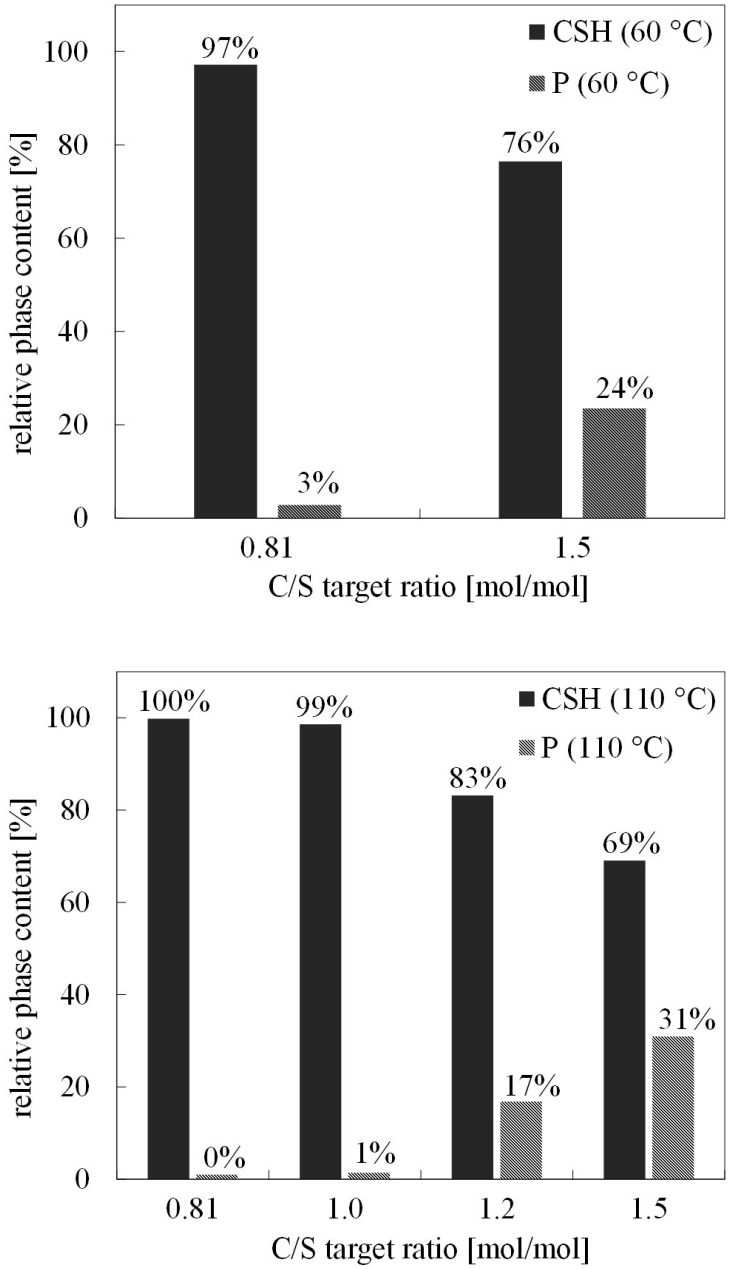

Figure 4.4: XRD relative phase content obtained by semi-quantitative analyses on samples made at 60 °C (*top*) and samples made at 110 °C (*bottom*). [P: portlandite reflection/phase; CSH: calcium silicate hydrate reflection/phase].

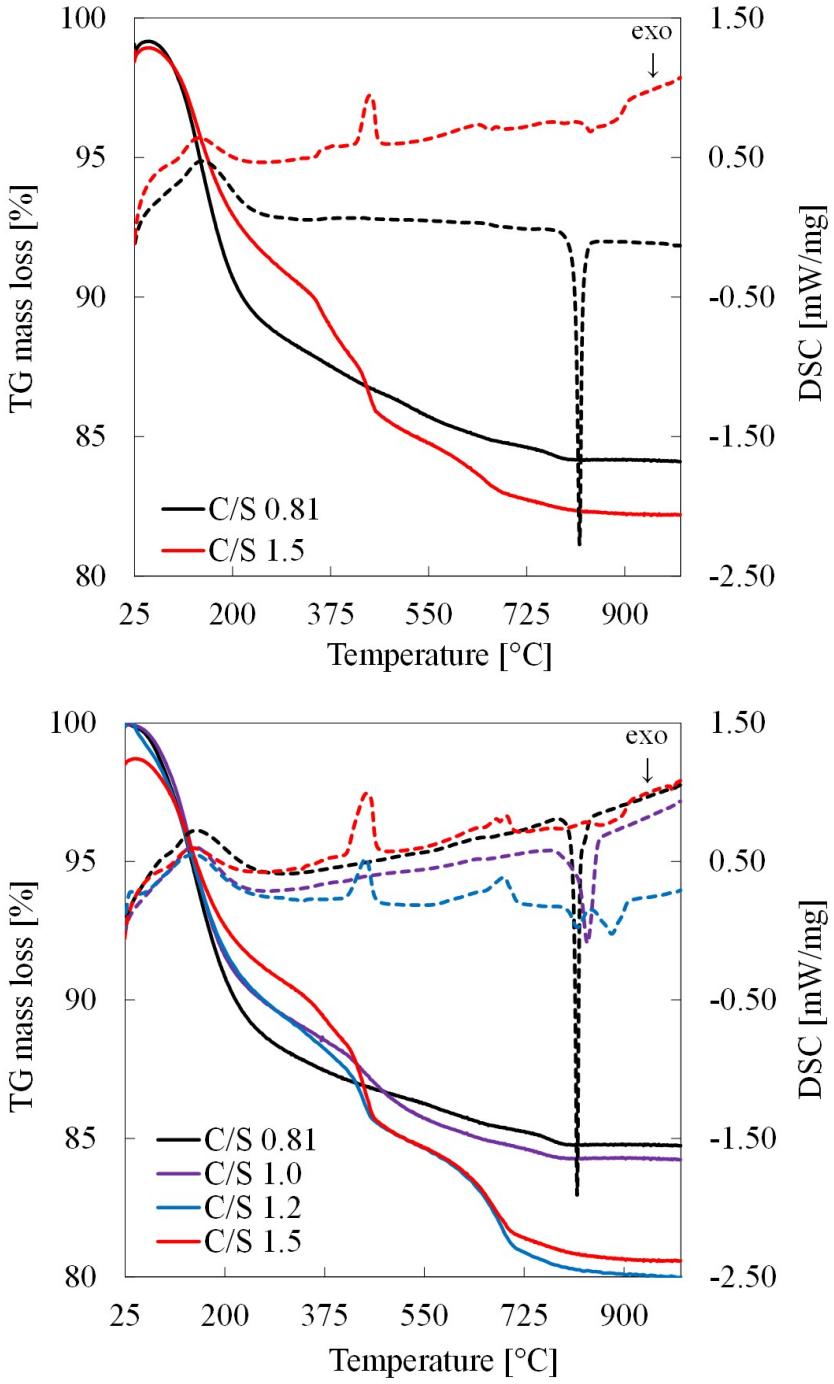

Figure 4.5: TG/DSC curves of samples at different target C/S ratios synthesised at 60 °C (*top*) and samples synthesised at 110 °C (*bottom*). [TG curves in solid lines, DSC curves in dashed lines].

4.3.2 Modelling the C/S ratio as function of temperature

TG weight loss was used to calculate the actual C/S ratio of the C-S-H produced in each sample. We followed the methodology described in *Chapter 2*, equations 2.2–2.14. In Figure 4.6 the actual C/S ratios is plotted as a function of the target C/S and the temperature of the synthesis. Increasing the hydrothermal formation results in a lower C/S ratio for the same initial stoichiometry. A linear relationship between target and calculated C/S ratios in the range 0.81–1.5 mol/mol is observed for synthesis at room temperature (20 ± 1 °C) as reported in *Chapter 2* and in agreement with literature [38, 73]. This feature is also observed for synthesis at 60 °C and 110 °C. The best fit regression line is given by the equation 4.2:

$$\overline{\mathrm{C/S}} = \mu(T) \cdot C/S + \epsilon(T) \tag{4.2}$$

where $\overline{\mathrm{C/S}}$ is the calculated C/S ratio, μ(T) is the gradient, and ϵ(T) is the y-axis intercept, the former is inversely proportional to the temperature (T) and the latter directly proportional to the temperature (T). μ(T) is dimensionless and could represent the effect of the temperature on the stoichiometry of the system, while ϵ(T) could represent a stoichiometric correction factor taking into account the kinetic reaction of C-S-H formation and the synthesis temperature. Assuming a linear relationship between the two parameters and the temperature as shown in Figure 4.7, μ(T) and ϵ(T) are fitted as shown in equation 4.3 and equation 4.4:

$$\mu(T) = -\alpha \cdot T + \gamma \tag{4.3}$$

$$\epsilon(T) = \beta \cdot T + \delta \tag{4.4}$$

where α is the reciprocal temperature ($^{\circ}\mathrm{C}^{-1}$), γ is a constant, β is the specific C/S ratio per degree Celsius in mol/(mol °C) and along with δ, in mol/mol, take into account the stoichiometry of the chemical reaction of C-S-H formation. The fit yielded the following parameters: $\alpha = 0.0015$, $\beta = 0.0008$, $\gamma = 0.7371$, and $\delta = 0.2123$. The model is based on a linear relationship between C/S ratio and temperature, in agreement with the study of Bahafid et al., (2017) [126]. This assumption is valid only within the temperature range (*ca.*

–5°+150 °C) in which the formation of C-S-H is physically possible. The lower temperature limit is reported to be –5 °C, at which point the paste freezes and the water needed for the chemical reaction to form C-S-H [$xCa(OH)_2 + ySiO_2 + zH_2O \rightarrow xCaO{\cdot}ySiO_2 \cdot (x+z)H_2O$] starts crystallising into ice. The higher temperature limit is calculated at the intersection of the two lines, imposing the condition $\mu(\mathrm{T}) = \epsilon(\mathrm{T})$, for which T = 220 °C. This is the temperature above which C-S-H transforms into tobermorite at ambient pressure or xonotlite [128, 133, 56] and loss of bound water occurs. Comparing the experimental data with results obtained from the three-equations, the maximum error observed was $< 2.0\%$. Increasing formation temperature

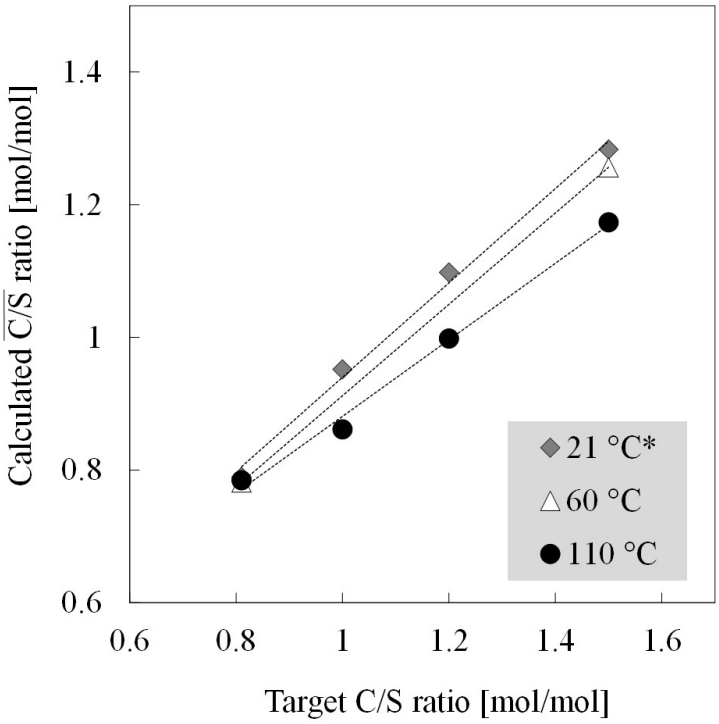

Figure 4.6: Calculated $\overline{\mathrm{C/S}}$ molar ratio values plotted as a function of the target C/S ratio of samples at different synthesis temperatures. (*)Data are compared to values obtained from synthesis at room temperature (21 °C) reported in *Chapter 2*.

produces C-S-H with a lower C/S ratio compared to synthesis at room temperature. C-S-H formed hydrothermally has a reduced interlayer distance that decreases further with increasing temperature explains the lowered C/S ratio and the higher excess of portlandite compared to room temperature. This is in agreement with the previous semi-quantitative results.

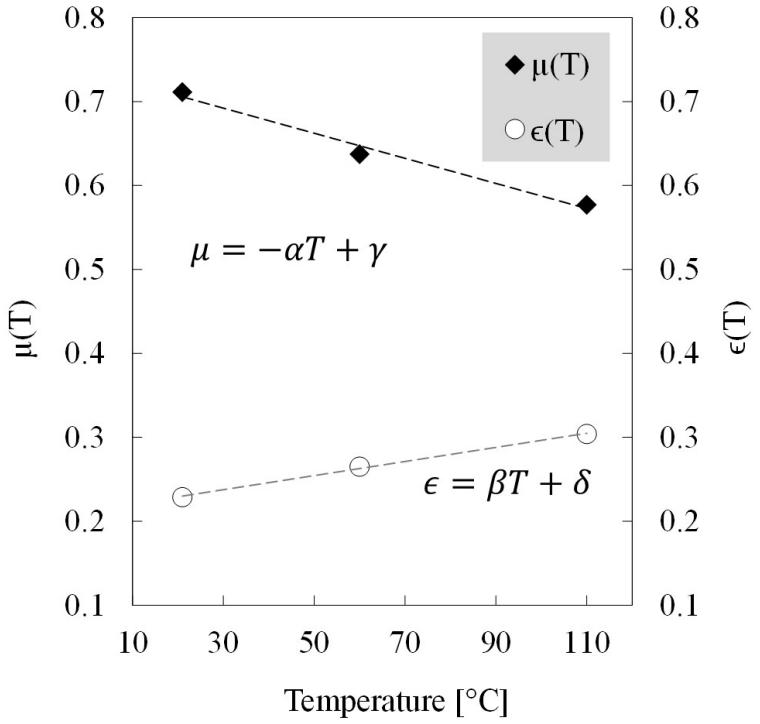

Figure 4.7: Values of coefficients μ and ϵ as a function of temperature calculated at 21°, 60° and 110 °C.

4.3.3 Phase evolution during the synthesis process

Time-resolved synchrotron XRD patterns for C-S-H at C/S 0.81 mol/ mol and 1.2 mol/mol synthesised at 110 °C are shown in Figures 4.9, 4.10, 4.11 and 4.12. For phase identification and data analysis, the background induced by the heating chamber and the fumed-silica glass windows was removed. However, reflections (indicated with *), from the PTFE liner, are present in the XRD patterns. Subtraction of those peaks would have compromised the overall quality of the data and so are not removed. During the synthesis of sample at C/S ratio 0.81 mol/mol the temperature slightly oscillated from 109 °C to 115 °C during the whole period of the measurement. It means the temperature was constant at 112.5 ± 2.5 °C. For the sample at C/S ratio of 1.2 mol/mol, the starting temperature was around 140 °C. It monotonously decreased to 110 °C during first 25 min of the experiment and then oscillated between 110 and 115 °C in the same way as observed for the previous sample. The temperature profiles of both samples are reported in Figure 4.8.

For the sample with target C/S ratio 0.81 mol/mol, only crystalline portlandite is found

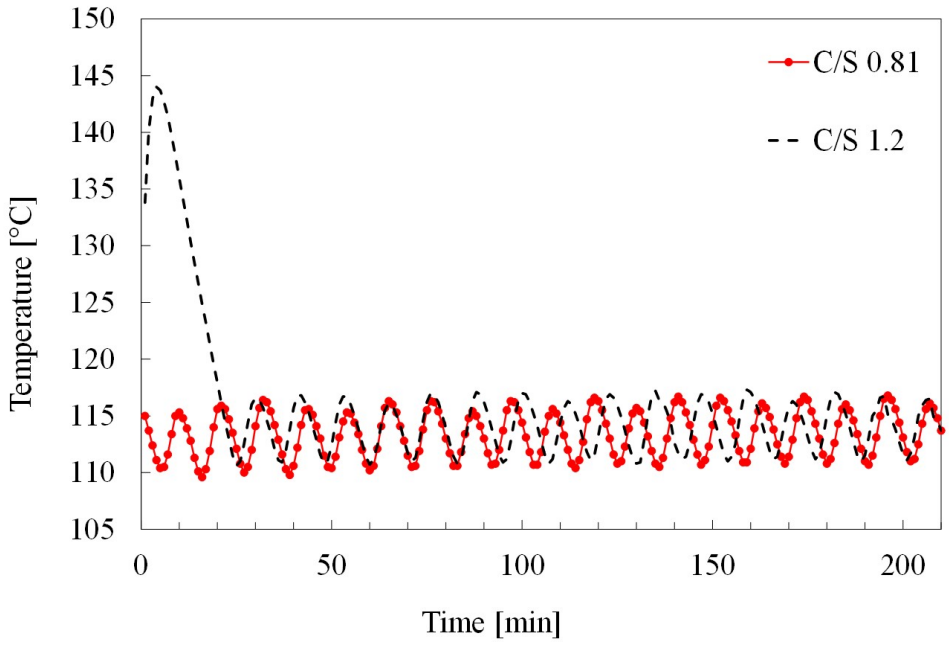

Figure 4.8: Temperature profile during the synthesis of samples at C/S ratio 0.81 and 1.2 mol/mol.

at the initial stages of synthesis (ICSD 64950, [138]) but starts to visibly decrease after 10 min, eventually disappearing completely. C-S-H forms after 10 min, as an amorphous phase, shouldering portlandite reflections, P(001), P(2-10) and P(2-11), and then rapidly increases in intensity until the end of the synthesis. In the sample with target C/S ratio 1.2 mol/mol, portlandite reflections decrease more slowly and are still observed at the end of the experiment. C-S-H starts forming after 15–20 min, rapidly grows and remains constant until the end of the experiment. The velocity of C-S-H and portlandite growth or dissolution is calculated from peak heights in each time resolved XRD pattern and then normalised.

Results are plotted for the two major reflections of portlandite, P(101) at *ca.* 34.5° 2θ and P(102) at *ca.* 47° 2θ, and two major reflections of C-S-H at *ca.* 29.2° 2θ, regarded as CSH(110) and *ca.* 49.5° 2θ, regarded as CSH(020) [139]. Figure 4.13 (*top*) shows the dissolution of portlandite plotted against the growth of C-S-H for sample at C/S 0.81 mol/mol. The saw-tooth effect observed in Figure 4.14 is due to a ring current oscillation occurred during data collection. Portlandite decreases rapidly in intensity within the first 25 min and then decreases with a slower rate. C-S-H grows rapidly from the beginning of the synthesis to $t \sim 30$ min and then increases slowly until the end of the process. The formation of C-S-H

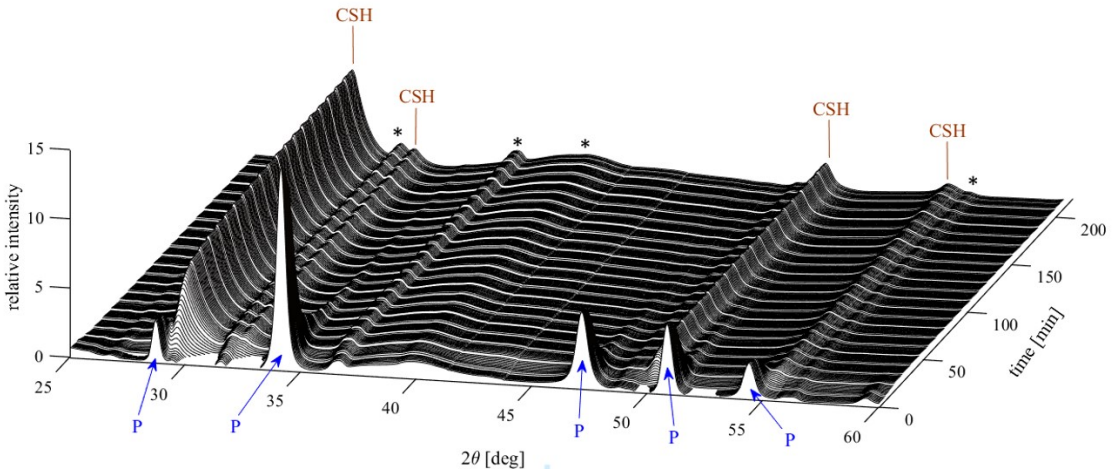

Figure 4.9: 3D Stack of time-resolved *in-situ* XRD patterns for sample with target C/S ratio 0.81 mol/mol synthesised at 110 °C. [CSH: reflections from calcium silicate hydrate phase. P: reflections from portlandite. (*) reflections associated with the PTFE sample holder]

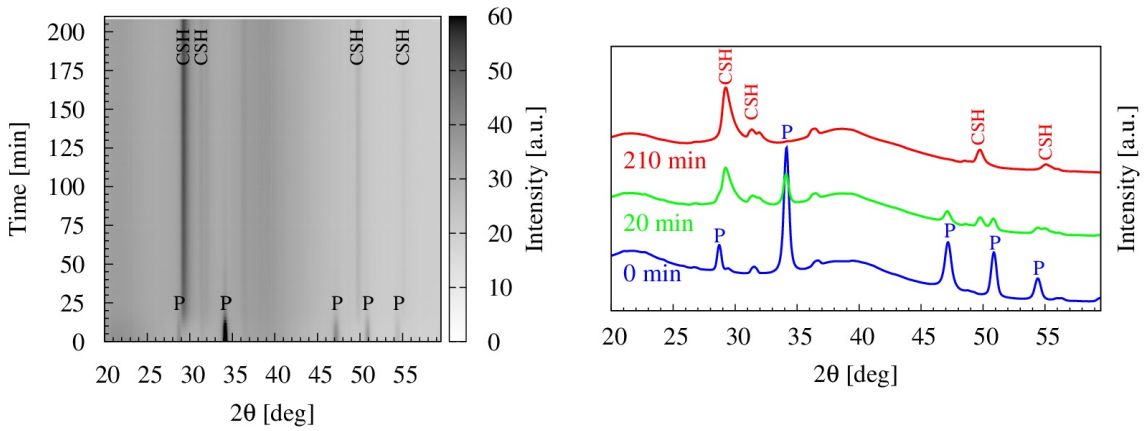

Figure 4.10: The contour plot of 3D XRD patterns collected during the annealing of the sample with C/S ratio 0.81 at 110 °C (*left*) and selected 1D intensity curves after 0, 20 and 210 min of annealing (*right*).

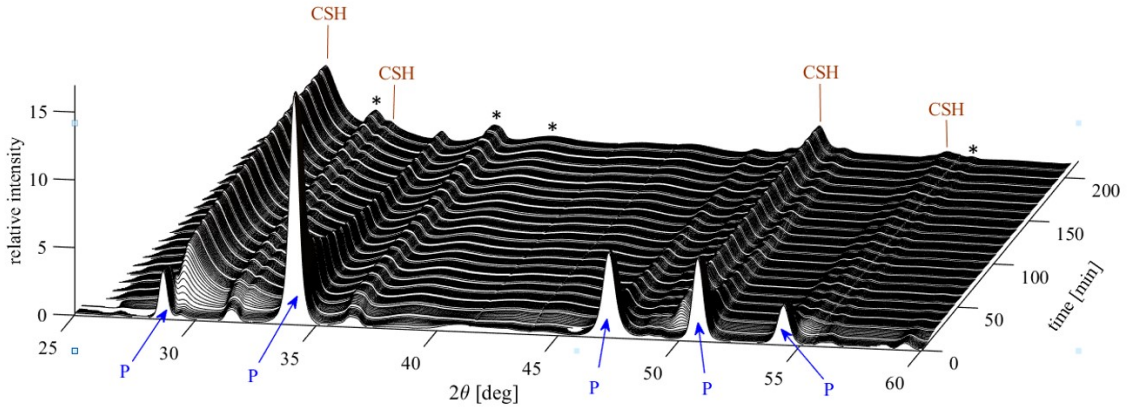

Figure 4.11: 3D Stack of time-resolved *in-situ* XRD patterns for sample with target C/S ratio 1.2 mol/mol synthesised at 110 °C. [CSH: reflections from calcium silicate hydrate phase. P: reflections from portlandite. (*) reflections associated with the PTFE sample holder]

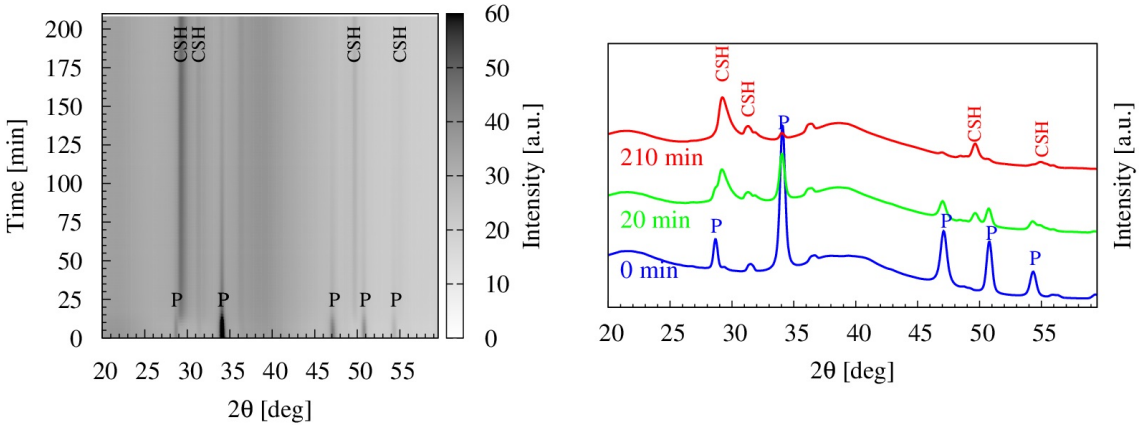

Figure 4.12: The contour plot of 3D XRD patterns collected during the annealing of the sample with C/S ratio 1.2 at 110 °C (*left*) and selected 1D intensity curves after 0, 20 and 210 min of annealing (*right*).

follows a nucleation and growth process, the former associated with the formation of broad peaks, the latter responsible for peak-narrowing [128]. An increase in calcium content (C/S ratio at 1.2 mol/mol) affects C-S-H growth: both C-S-H reflections start increasing with a delay of *ca.* 10 min, and at 30 min a slight difference in the rates of growth is observed, as shown in Figure 4.13 (*bottom*). The rate of increase of the reflection CSH(110) appears to be slightly greater than that of of CSH(020), suggesting that the presence of more Ca ions inhibits the crystal growth along the *b*-axis, in agreement with Grangeon et al., (2016) [140] and Tajuelo et al., (2017) [66]. C-S-H growth and portlandite dissolution rates were fitted using the Avrami (or JMAK) function (equation 4.5) [90]:

$$I_n(t) = A(1 - e^{(k(t-t_0))^m}) \tag{4.5}$$

where $I_n(t)$ is the normalised intensity of the XRD reflections, proportional to the volume fraction that has transformed at time t, A is a proportional coefficient, m reflects the growth/-dissolution dimensionality and mechanism, and k is a rate constant that takes into account the rates of growth and nucleation or dissolution process. The kinetic relationship was used to fit C-S-H growth and portlandite dissolution. In the first case m was fixed at 1, assuming that: (a) C-S-H is growing in sheets or platelets, based on SEM evidence in reported in *Chapter 2* and elsewhere [75, 51]; (b) diffusion is the growth mechanism and it is rate-controlled, and (c) the type of nucleation is for site saturation. k and A were allowed to vary and t_0 varied in the range 8–12 min. In the second case m and k were allowed to vary and A was fixed at 1. Parameter values are given in Table 4.3. The rate constant k for CSH(020) with C/S ratio at 1.2 mol/mol is 0.04 min^{-1}, smaller than that for 0.81 mol/mol, indicating a lower rate of growth along the *b*-axis. Similarly, portlandite tends to dissolve more slowly when it is present in greater quantities with values of k *ca.* 10 times smaller.

To consider the effect of temperature and C/S molar ratio on the crystallographic structure of C-S-H, the XRD diffraction peak position of C-S-H and portlandite were observed. Calcium silicate hydrate structure varies with Ca and Si content, synthesis condition and temperature. The lattice parameters vary too and shifts in Bragg peak position are often reported [128, 135, 56]. Figures 4.14 (*top*), 4.14 (*centre*) and Figure 4.14 (*bottom*) show respectively the

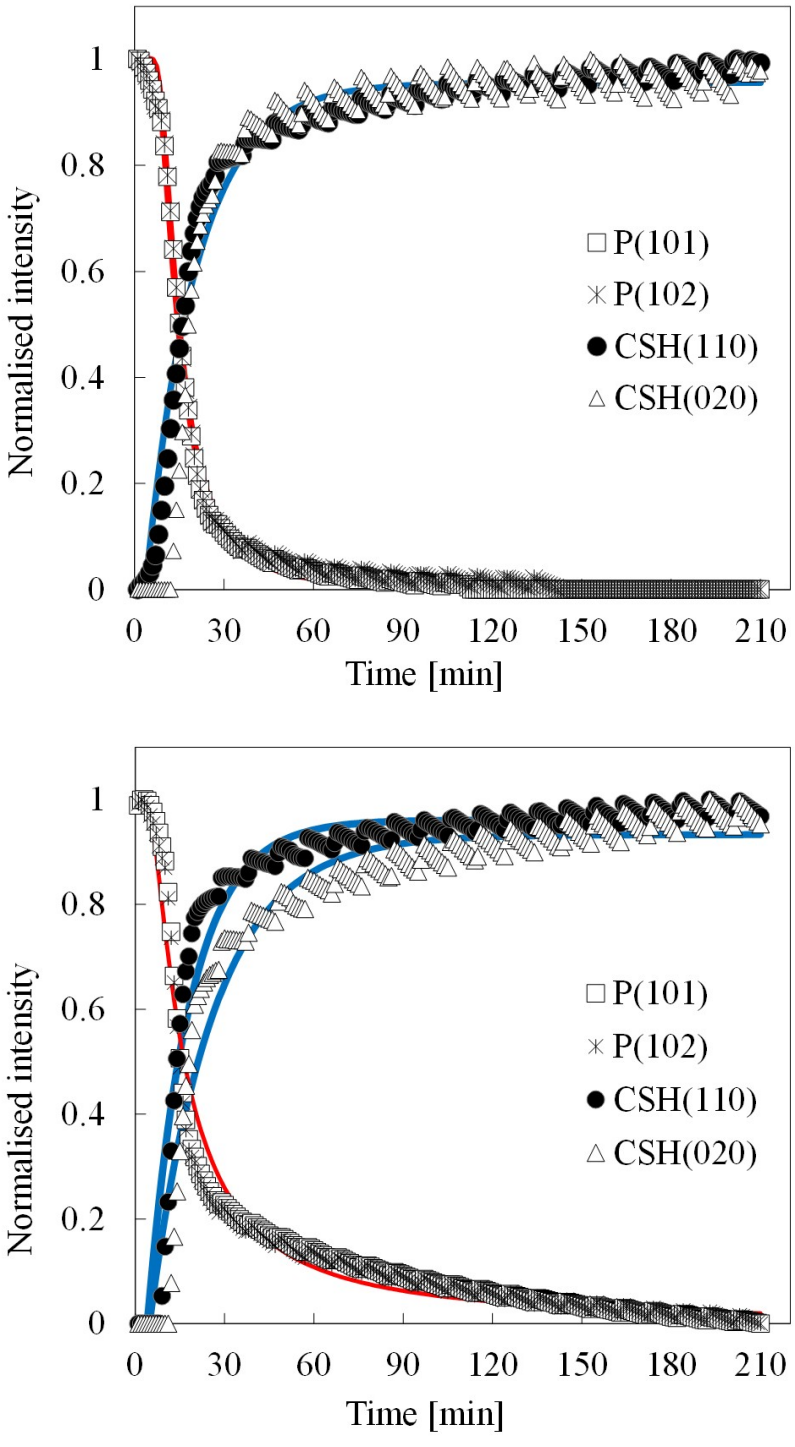

Figure 4.13: Time dependence of normalised peak intensity for sample with target C/S ratio 0.81 mol/mol (*top*) and sample with target C/S ratio 1.2 mol/mol (*bottom*). [P, portlandite reflections; CSH, calcium silicate hydrate reflections. Data were fitted using equation 4.5 for C-S-H growth (blue line) and portlandite dissolution (red line)].

Table 4.3: Values of the parameters of Avrami equation used to fit the normalised intensity curves of portlandite and C-S-H reflections.

Bragg reflection	C/S mol/mol	A -	k t^{-1}	m -	t_0 min	R^2 -
CSH(110)	0.81	0.96	0.05	1	0	0.95
CSH(020)	0.81	0.96	0.05	1	12	0.94
CSH(110)	1.2	0.96	0.04	1	8	0.95
CSH(020)	1.2	0.93	0.04	1	11	0.95
P(101)	0.81	1	522	-2.5	0	0.99
P(102)	0.81	1	425	-2.4	0	0.99
P(101)	1.2	1	34	-1.4	0	0.97
P(102)	1.2	1	32	-1.4	0	0.98

d-spacing of C-S-H reflections (110), (200) and (020), (in Å), as function of time (in min). Values are compared to peak positions of C-S-H synthesised at room temperature (red dashed lines). For C/S ratio 0.81 and 1.2 mol/mol,reflection CSH(020) stabilises at a constant value (higher than that of C-S-H synthesised at room temperature) until the end of the process (Figure 4.14 *bottom*), whereas a monotonic decrease in the reflection CSH(200) is observed, as shown in Figure 4.14 (*centre*). In both cases, however, the elevated temperature causes a shift of the peak position toward higher *d*-spacing, suggesting that the C-S-H structure is under lateral extension, more evident in the *b*-direction 4.14 *bottom*. Further extension (*ca.* +0.3%) is caused by an increase of Ca content (C/S ratio 1.2 mol/mol). The main and strongest reflection CSH(110) increases with time, from 3.054 Å to 3.059 Å at the end of the synthesis for sample at C/S ratio of 0.81 mol/mol, and from 3.054 Å to 3.061 Å for sample at C/S ratio of 1.2 mol/mol, with an extension of *ca.* +0.2 ± 0.02% to that of C-S-H synthesised under ambient conditions (3.047 Å).

Figure 4.15 shows the peak position of portlandite and a magnification of one peak at *ca.* 47° 2θ. As the reaction proceeds peaks shift toward lower 2θ angle (higher *d*-spacing), in accordance with literature; Fukui et al., (2003) described the thermo-elastic properties of portlandite under temperature and pressure increase and an equation of state for portlandite was obtained via *in-situ* XRD measurements. Xu et al., (2007) found that gradually increasing the temperature from 308 K to 643 K of $Ca(OD)_2$ powder resulted in an anisotropic volumetric expansion of the unit-cell mainly along the *c*-axis [141]. In this work a Monte Carlo simulation

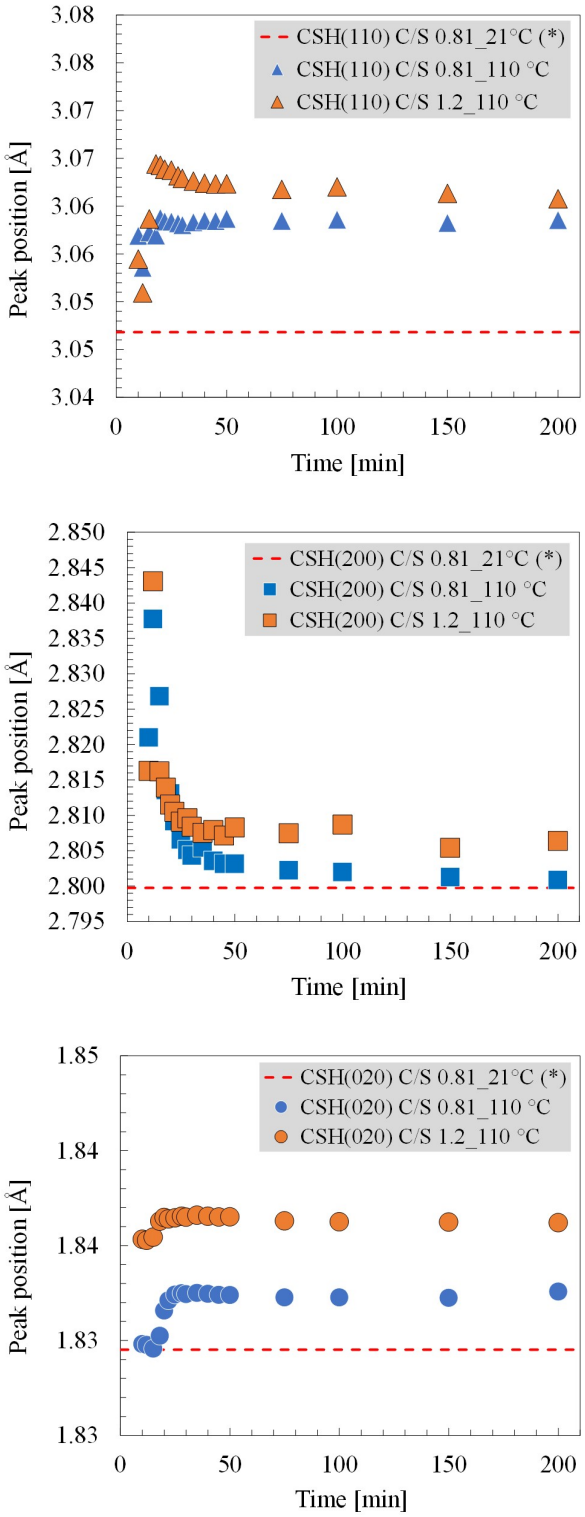

Figure 4.14: Time dependence of diffraction peak position of C-S-H d_(110) (*top*), d_(200) (*centre*) and d_(020) (*bottom*). (*)Peak position of C-S-H reflection in sample with C/S ratio of 0.81 mol/mol, cured for 28 days at 21 °C.

by McMaille was used to calculate the portlandite unit-cell parameters [142]; results are presented in Table 4.4. In the sample synthesised at C/S ratio 0.81 mol/mol, calcium hydroxide is rapidly consumed to form C-S-H and thermal expansion is limited to the first 60 min of the synthesis, after which no portlandite is detected (volumetric expansion of +0.41%). In sample at C/S 1.2 mol/mol, a higher volumetric expansion (+0.9%) was observed, due to the excess of unreacted calcium hydroxide. The coefficient of volumetric thermal expansion (α_v) of portlandite was calculated using the equation 4.6:

$$ln(\frac{V}{V_0}) = \int \alpha_v dT \tag{4.6}$$

where V_0 is the initial unit-cell volume (54.777 Å^3) at initial temperature T_0 = 21 °C (294.15 K), V is the volume measured at the time t (min) and temperature T (K).

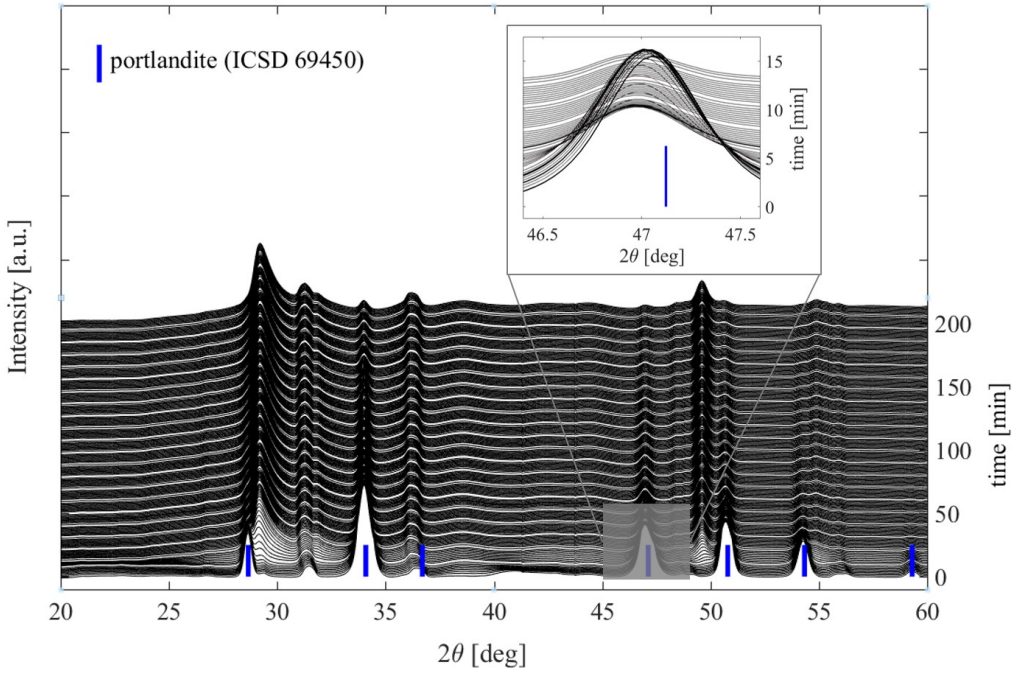

Figure 4.15: Stack of XRD plots of sample at C/S 1.2 mol/mol synthesised at 110 °C. Magnification of XRD position at 46.4-47.6°2θ and peak profile of Portlandite reflection P(102)

The value calculated for the coefficient of thermal expansion of portlandite, α_v, for the sample synthesised at C/S ratio 1.2 mol/mol is $4.48 \cdot 10^{-5}$ K^{-1}, smaller than that reported in the work of Fukui et al., (2003), $5.49 \cdot 10^{-5}$ K^{-1} [143]. This could indicate that the excess of

Table 4.4: Summary of crystallographic parameters of $Ca(OH)_2$ obtained using McMaille for indexing powder diffraction patterns.

Parameters		ICSD 64950	sample C/S 0.81		sample C/S 1.2	
temperature (°C)		21	115	110	140	110
time (min)		-	1	50	1	50
Space group	P-3 m 1					
Lattice parameters (Å)	a	3.589	3.5912	3.5973	3.5982	3.6
α=β=90°	b	3.589	3.5912	3.5973	3.5982	3.6
γ=120°	c	4.911	4.8981	4.9084	4.9263	4.9254
Unit-cell volume (Å^3)	V	54.7832	54.777	55	55.138	55.282

Ca^{++} precipitates as $Ca(OH)_2$, which is included in the interlayer of C-S-H, where is not free to expand to its maximum. This finding supports the experimental observation of Grangeon et al., (2016): increasing the C/S ratio results in a decreased basal spacing and structural evolution of C-S-H, where Si bridging tetrahedra are omitted and interlayer Ca^{++} ions start coordinating to form interlayer $Ca(OH)_2$ resembling portlandite [140]. However, in the present *in-situ* experiment observation of the basal spacing (at around 7° 2θ) was not possible, due to instrument settings. From the semi-quantitative results afore-presented, the sample with C/S ratio 1.2 mol/mol synthesised at 110 °C has a relative content of portlandite *ca.* 17%, higher than the one synthesised at room temperature (*ca.* 5%); this indicates that a significant amount of Ca^{++} in excess has been included in the C-S-H interlayer as $Ca(OH)_2$, limiting its thermal expansion when increasing target C/S ratio from 0.81 mol/mol to 1.2 mol/mol at 110 °C, in agreement with the results presented in Grangeon et al., (2016) [140]. Hence temperature plays a key role on C-S-H formation and structural evolution, portlandite could be used as an indirect indicator of structural changes in C-S-H. Grangeon et al., (2013) stated that synthesis temperature has no significant influence on the three-dimensional structure of C-S-H [56]. In the present work, however, a thermal expansion of C-S-H (i.e. lateral extension along a-axis and b-axis) was observed, with respect to samples synthesised at 21 °C. This could suggest an anisotropic behaviour of the C-S-H structure under hydrothermal conditions described as a decrease (or self-compression) of the interlayer spacing, due to omitting Si bridging tetrahedra, and a thermal expansion along the a and b-axis.

4.4 Conclusions

C-S-H was hydrothermally synthesised at 60° and 110 °C at varying C/S ratio, respectively 0.81 and 1.2 mol/mol. The syntheses were conducted *ex-situ*, using university laboratory facilities and post-analysis (lab-XRD, TG/DSC) and modelling, and *in-situ* by means of synchrotron X-ray radiation for time-resolved diffraction pattern acquisition. Particularly, C-S-H growth and portlandite dissolution were monitored by synchrotron *in-situ* XRD measurements. The following conclusions can be drawn from this study:

- An increase in synthesis temperature results in a decrease of final C/S ratio: a three-equations model was defined to predict the C/S ratio from a given initial stoichiometry and synthesis temperature.
- Higher target C/S ratio results in a lower rate of C-S-H formation, at the same temperature.
- $Ca(OH)_2$ X-ray fingerprints were used as indirect measurement of the C-S-H structure and its anisotropic behaviour under hydrothermal conditions.

Results here presented are valuable for further research, especially modelling and investigation [144, 145] of elastic properties of C-S-H hydrothermally synthesised.

Chapter 5

Low-pressure silica injection for porosity reduction in cementitious materials

Abstract. The durability of building materials is related to the presence of cracks as they provide a fast pathway to the transport of liquid and gases through the structure. Restoration and preservation of historic buildings has been investigated through the application of novel cementitious materials, using nanoparticles such as nano-silica and silica fume. The small particle size range and the high reactivity of nanoparticles allow them to interact with calcium sources naturally present in construction materials, forming binding and strengthening compounds such as calcium silicate hydrate. Nanoparticles act as a crack-filling agent, reducing the porosity and increasing the durability of existing materials. In this study it is described the injection of nano-silica using low water pressure in hydrated cement paste. This novel technique can tailor mechanical and hydraulic properties of existing building materials using a simple and non-destructive procedure.

5.1 Introduction

Most of the built environment uses cement or concrete in some way, and many historic buildings constructed in 1950's and later suffer from crack formation, water penetration and damage mechanisms such as alkali-silica reaction. Cracking in concrete and mortar is an inevitable phenomenon of ageing and erosion. Thus, material characteristics such as porosity, permeability and strength are altered during ageing. Hardened concrete and cement contain two important mineral phases: calcium hydroxide (portlandite) and C-S-H, the former has a defined crystalline structure, the latter is semi-crystalline [146]. C-S-H is the phase responsible for strength development in concrete and can form up to 70% of the total volume of hardened concrete [38]. C-S-H is produced by hydration of C_3S and C_2S (impure tricalcium silicate and dicalcium silicate respectively) which are present in cement clinker. Pozzolanic materials such as fly ash, slag, rice husk ash and silica fume can also be added, resulting in the production of more of C-S-H and improved mechanical performance [147, 24]. The formation of cracks and increased porosity from leaching in concrete and cement paste presents an easy pathway for the ingress of moisture. Gaps and cracks can be reduced by treating with nanoparticle consolidants. In the work presented here, the injected silica reacts with portlandite naturally present in hydrated cement paste to form new C-S-H and reduce the porosity of the system. The result is increased durability and life-time [148, 149, 150, 151]. Research on partial replacement of cement clinker with nano-silica [152] found that increasing the quantity of nano-silica replacing cement from 3% to 5% vol. results in higher mechanical strength of mortar through acceleration of the hydration reaction and the filler effect of nano-particles. In addition, the hydrated paste had a dense and compact texture and an absence of portlandite crystals was observed, suggesting that most of the calcium hydroxide reacted with the nano-silica added [152, 153, 76]. Nano-silica addition to cement paste increases C-S-H formation and accelerates hydration of unreacted alite (C_3S), due to the high reactivity of small particles [154]. An average water penetration depth of 14.6 cm in concrete made with fly ash and cement under low applied pressure was observed, whereas a water penetration depth of 8.1 cm in concrete mixed with nano-silica under high pressure was recorded, confirming the improvement in water

penetration resistance with nano-silica addition [153]. It was concluded that the pozzolanic reaction of fly ash in the presence of nano-silica produces C-S-H faster and earlier compared to OPC with fly ash but no nano-silica. Qing et al., (2007) report little acceleration in the setting time of fresh paste with increasing nano-silica content, but some enhancement of compressive strength. Pozzolanic reactivity of nano-silica is higher than silica fume, due to the smaller particle size and higher specific surface area [76]. Varying the nano-silica content (3, 6, 9, and 12 wt.%) in mortar produces an increase in strength correlated with a decrease in calcium hydroxide content. The heat of hydration is also increased by addition of nano-silica due to the rapid hydration of silicates [155]. Nano-silica surface treatments have been investigated using electro-kinetic deposition, nanoparticle coating, brushing etc. A reduction in permeability was observed by Cardenas et al (2006), for low alkali cement paste with 0.8 w/c ratio and impregnated with colloidal alumina by electro-phoresis [148]. Pore size refinement by reduction in pore volume of treated samples with higher w/c ratio was also observed. The effect of curing temperature on hardened cement paste treated with nano-silica and tetraethyl orthosilicate (TEOS) in sealed and unsealed condition was studied [149]. They found that mortar samples cured at 50 °C and treated with nanosilica/TEOS show a reduction in water absorption compared to samples cured at 20 °C. High temperature curing contributes to production of additional C-S-H gel and reduction of calcium hydroxide, which results in capillary pores becoming smaller and finer gel pores. The transport properties of cement pastes with varying w/c ratio and surface treated with nano-silica and TEOS were also investigated. The water absorption and water vapour permeability is decreased by incorporation of nano-silica and TEOS in mortar with higher w/c ratio. Hardened mortar surface treated by nano-silica using electro-migration, showed reduced cumulative porosity and a higher rate of pozzolanic reaction was confirmed by the portlandite content [150]. While the application of nano-particles to cement and concrete surfaces has been shown to have beneficial effects on cement durability, very little research has been conducted on developing low cost and non-destructive techniques for concrete surface treatment. The aim of this work was to investigate a non-destructive and easily applied conservation treatment for cement and concrete, which is relevant to infrastructure conservation, ranging from buildings to bridges

and more specialist applications in nuclear waste containment ponds. In this study the effect of nano-silica and silica fume injection in hardened cement paste was investigated by quantitative analysis of hydration products (C-S-H and portlandite) present.

5.2 Materials and methods

5.2.1 Materials

The experiments were carried out on pure hardened cement paste, using ordinary Portland cement CEM II/A-L, class 42.5 N purchased from Lagan Cement (physiochemical properties are listed in Table 5.1) and deionized water. Nano-silica (NS) suspension LUDOX TM-50 (CAS number 7631-86-9) and silica fume (SF) (CAS number 69012-64-2) ELKEM microsilica SF920D were used. Their chemical properties are detailed in Table 5.2.

Table 5.1: Characteristic of CEM II/A-L (Class 42.5 N) Portland cement (according to the certificate of conformity, test method BS EN 196-2).

Components	CEM II
Clinker	80–94%
Gypsum added	4.0%
Limestone	6–20%
Chemical composition (>0.2%)	
SiO_2	18.2%
Al_2O_3	4.5%
Fe_2O_3	2.6
CaO	64.0
MgO	1.3
SO_3	2.3
Na_2O	0.23
Density (kg m^{-3})	3100
Specific area (m^2 g^{-1})	0.41
Compressive strength at 28 day (MPa)	57.5

Table 5.2: Characteristics of nano-silica (NS) aqueous suspension and silica fume (SF).

Components	NS	SF
State	suspension in H_2O	powder
Chemical composition (>0.2%)		
SiO_2	50%	99.9%
Water	50%	-
Particle size diameter (nm)	5–20	100–1000
Density (g cm^{-3})	1.4	2.2–2.3
Specific surface area (m^2 g^{-1})	110–150	15-30

5.2.2 Sample preparation

Cement samples were prepared mixing Portland cement and deionized water at a water to cement (w/c) ratio of 0.41. Cement and water were mixed in a rotary mixer according to BS EN 196-1:2005. Cement paste was cast into plastic moulds (35mm ⌀ and 4mm thickness, disc-shaped) and cured under controlled conditions (RH 98 ± 2% and temperature of 21 ± 2 °C). After 28 days, cement discs were oven-dried at 60 °C for *ca.* 100 hours, until mass change was negligible. Drying temperature of 60 °C was chosen because it does not affect the pore-structure and mineralogy of the cement paste [156, 157, 158, 92].

5.2.3 Experimental design

Nano-silica injection was carried out by varying three parameters: injection period, percentage of nano-silica injected and silica particle size (NS or SF) using a constant applied pressure head. Silica solutions were prepared using nano-silica stock suspension or solid silica fume, mixed with deionized water. In order to investigate how the penetration depth in the disc varies with nano-silica content, three different percentages (10, 15 and 20 wt.%) were used, for a total injection time of 14 days. The effect of injection time was determined by keeping cement discs under hydrostatic injection for 7, 14 and 28 days with 10 wt.% nano-silica colloidal suspension. To compare the reactivity and effect of particle size on penetration depth, samples were injected with 10% and 20% of silica fume for the period of 14 days (Table 5.3). The cement disc was fixed in place at the bottom of a PVC pipe of 2 m length and 40 mm internal diameter (Figure 5.1), the pipe was then clamped vertically in a retort stand. The solution of

nano-silica at a given concentration was slowly poured into the pipe from the top, to minimize the density gradient. The length of pipe used gives a constant hydrostatic pressure of 20 kPa at the bottom of the pipe, where the OPC specimen is placed. After filling the pipe, a plastic cap was placed at the top of the pipe to avoid evaporation of the suspension. At the end of the injection period the disc was removed and oven-dried at 60 °C for *ca.* 100 hours, until no change in weight was recorded. The sample weight was recorded before and after the injection to quantify the mass of silica added to the pores.

Table 5.3: Experimental data and sample detail of each mix using either nano-silica (NS) or silica fume (SF).

Sample	Injected silica NS or SF	Silica content wt.%	Injection period days
S10-7	NS	10	7
S10-14	NS	10	14
S15-14	NS	15	14
S20-14	NS	20	14
S10-28	NS	10	28
SF10-14	SF	10	14
SF20-14	SF	20	14

5.2.4 Microstructural analysis

The capability of injected silica to react with portlandite, calcium hydroxide (CH), present in the hydrated cement paste to form additional calcium silicate hydrate (C-S-H) was determined by the quantity of calcium hydroxide and calcium silicate hydrate in the treated hydrated cement paste compared with the control sample by thermogravimetric analysis (TGA). An average of *ca.* 20 mg was sampled from the cross section of the disc and powdered. Thermal analyses were conducted at a heating rate of 10 °C min^{-1} from 25 °C to 1000 °C under nitrogen gas flow, using a Netzsch simultaneous analyser. Mineralogical composition of silica injected specimens was analysed by powder X-ray diffraction (XRD) technique using a Bruker D8 Advance diffractometer, from 5° to 60° 2θ, at a rate of 1° min^{-1} and a step size of 0.02° 2θ. To determine silica entrainment through the pores, sample disc mass was recorded before

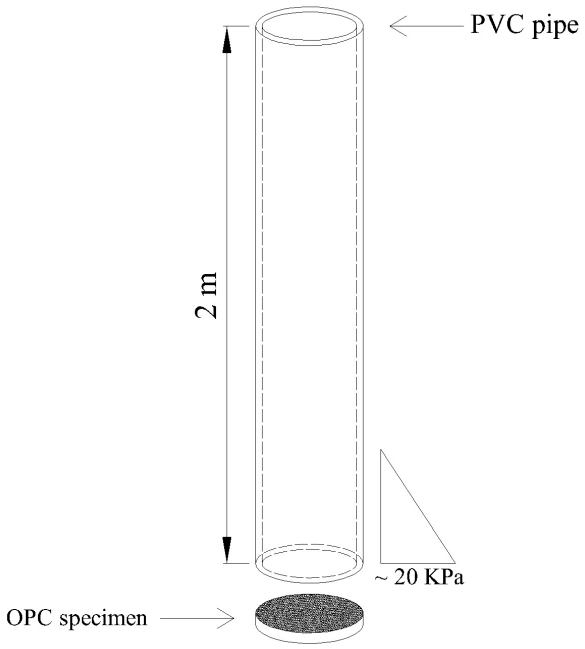

Figure 5.1: Experimental set-up model of the OPC disc and the injection column. Graphic representation not in scale.

and after silica injection, by oven drying at 60 °C. The disc was then broken into several parts. Open porosity (φ) was estimated by measuring the total water content in each sample (in three replicates) after oven-drying at 60 °C and overnight saturation in a vacuum chamber. Open porosity was calculated using equation 5.1:

$$\varphi = \frac{m_s - m_d}{V \cdot \varrho} \tag{5.1}$$

where φ is the open porosity, m_s is the sample water saturated mass (kg), m_d is the sample dried mass (kg), V is the volume of the sample (m^3) and ϱ is the density of the water at 20 °C (kg m^{-3}). The open porosity value is the average of three measurements. Microstructural analysis of samples was characterized using Scanning Electron Microscopy (FEG-SEM, Hitachi SU6600) and Energy Dispersive Spectroscopy (EDS, Oxford INCA-7260) with an accelerating voltage of 10–15 kV. All samples were resin impregnated, polished and gold coated. The penetration depth of the silica after injection was also estimated by SEM imaging (Figure 5.2).

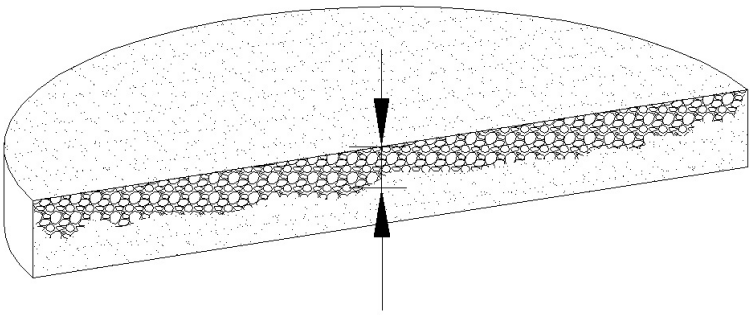

Figure 5.2: Model of silica penetration depth (indicated between black arrows) on OPC disc-shaped specimen after injection.

5.3 Results and discussions

5.3.1 Weight change and porosity measurements

Mass measurements showed that after 14 days of injection of nano-silica the mass increase is directly proportional to the silica concentration in the solution (Figure 5.3). This observation indicates that the silica is not simply filling the pores but has reacted with the portlandite forming additional hydrated phases. At a given nano-silica content in the pipe of 10 wt.%, the sample mass shows an increase reaching 2.0 wt.% mass gain after 28 days (Figure 5.3). A comparison between nano-silica and silica fume show the effect of particle size on the injection: doubling the concentration of nano-silica results in a mass increase of *ca.* +1.2%, whereas doubling the silica fume content results in an increase of *ca.* +0.3%. This is probably due to the low particle size range of nano-silica (5–20 nm), able to penetrate into smaller pores. Open porosity (φ) measurements show that an increase in nano-silica content in the solution produces a significant decrease in porosity of *ca.* 30%, from the initial value (sample OPC, $\varphi = 0.30$) to the highest concentration at 20 wt.%. (sample S20-14, $\varphi = 0.20$), as shown in Figure 5.4. Injection of silica-fume, on the other hand does not produce a significant porosity reduction [76]. Injection time at the lowest nano-silica content (10 wt.%) shows a reduction in porosity of *ca.* 20%, from the initial value (sample OPC, $\varphi = 0.30$) to the longest injection time (sample S10-28, $\varphi = 0.24$) as shown in Figure 5.4.

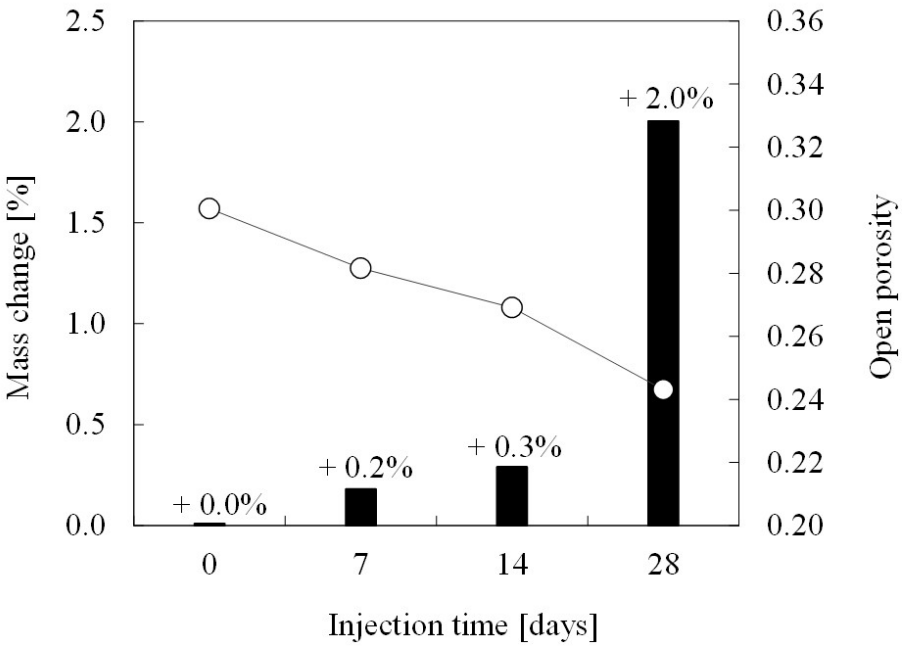

Figure 5.3: Influence of injection time on mass increase and open porosity using a 10 wt.% nano-silica suspension. Bars represent mass change and open circles represent porosity values.

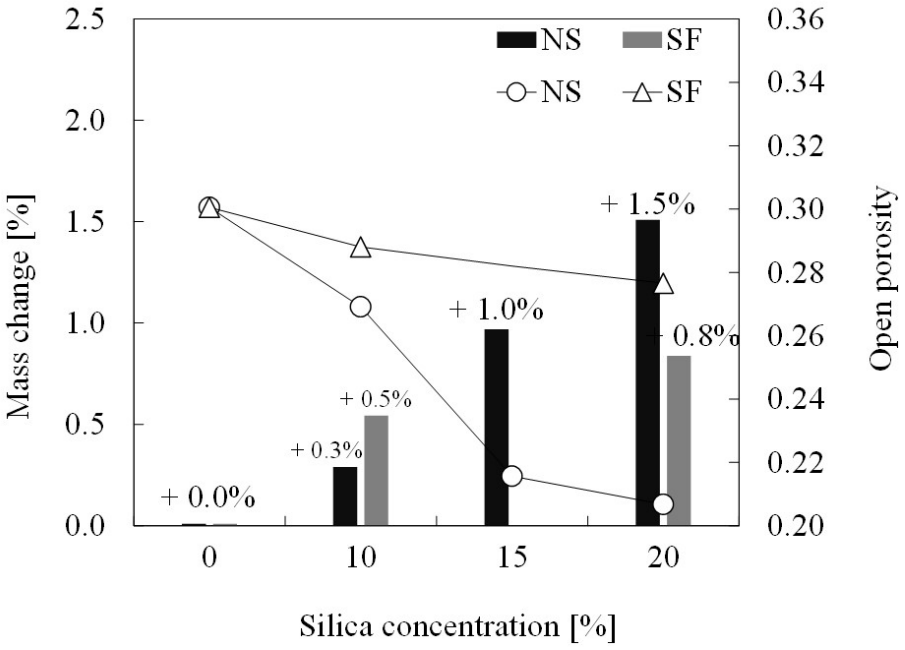

Figure 5.4: Influence of silica concentration on mass increase and open porosity after injection for 14 days. Bars represent mass change and open circles represent porosity values.

5.3.2 Thermogravimetric analysis and XRD analysis

Figure 5.5 shows the thermogravimetric (TG) curves for selected samples. The mass loss is in % with respect to temperature (25–1000 °C). All samples show TG curves typical of Portland cement, having maximum mass loss from room temperature to 200 °C. The mass loss in the range 80–150 °C is attributed to C-S-H gel, calcium aluminum silicate hydrate (C-A-S-H) gel, ettringite and other minor compounds [159, 160, 113]. The thermogravimetric step in the range 400–460 °C is assigned to portlandite dehydration, $Ca(OH)_2$. Mass loss over the range 530–660 °C may be attributed to the loss of CO_2 from any calcium carbonate present. All samples show a slight mass loss in the range 700–780 °C due to the dehydroxylation of silanol Si-O-H groups [160, 44] or transition to wollastonite [66].Table 5.4 shows the TG values in the C-S-H and portlandite range calculated using the equation 5.2:

$$m = m_{T_i} - m_{T_f} \tag{5.2}$$

where m is the mass loss in % in the defined temperature range (T_i–T_f), m_{T_i} is the mass loss at the initial temperature T_i and m_{T_f} is the mass loss at the final temperature T_f.

Table 5.4: Summary of the thermal steps from thermogravimetric measurements for each sample, indicated as mass loss %.

	C-S-H	$Ca(OH)_2$	Water
Sample	80–150 °C %	400–460 °C %	30–550 °C %
OPC	2.89	3.35	14.21
S10-7	2.80	2.70	13.68
S10-14	3.02	2.68	14.09
S15-14	3.04	1.96	11.34
S20-14	3.09	2.03	11.99
S10-28	2.81	2.15	12.09
SF10-14	2.80	2.25	12.72
SF20-14	3.01	2.09	12.61

Figure 5.9 shows the reduction of portlandite as it reacts with nano-silica to form additional C-S-H, which can be quantified by XRD analysis. This reduction of *ca.* 40% from the initial

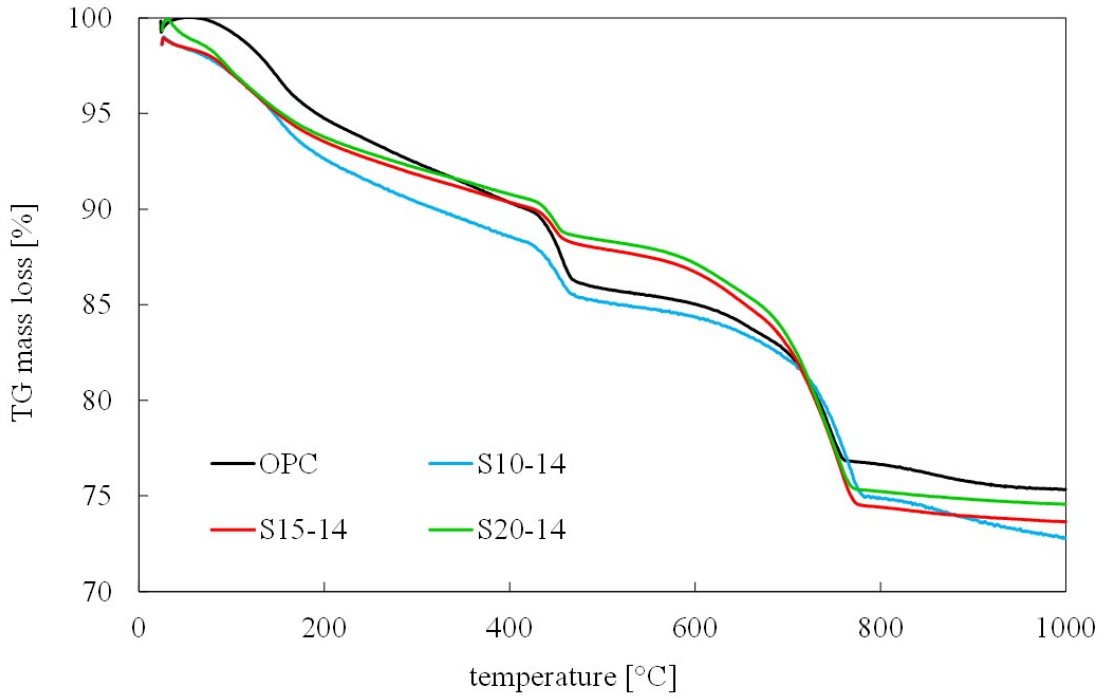

Figure 5.5: Thermogravimetric (TG) curves of OPC control sample and S10-14, S15-14 and S20-14 samples.

portlandite content is higher compared to the values found in literature [148, 150], due to a longer treatment time and higher applied pressure. There is no evidence of increased portlandite reduction when the nano-silica suspension concentration is increased beyond 15 wt.% in the injecting solution. The total increase of C-S-H formed, *ca.* 20% with respect to the original value, is over-estimated, due to the presence of other minor compounds in the same temperature range (80–150 °C). Accurate estimation is given in semi-quantitative analyses of XRD patterns. Figure 5.10 suggests that the ideal injection period is 14 days, producing a portlandite reduction of *ca.* 40%. TG analysis of nano-silica and silica fume for 14 days injection time show that both materials offer a comparable portlandite reduction at the highest concentration (20 wt.%).

XRD analysis of the injected samples (Figure 5.6) show a progressive decrease in intensity of portlandite and calcium aluminate phases reflections. Calcium aluminate phases (C_3A, peak at *ca.* 11.5° 2θ), present in the original clinker reacted with nano-silica forming additional C-S-H or C-A-S-H, observed at *ca.* 15.5° 2θ. As shown in Figure 5.7 and Figure 5.8, the

XRD patterns are plotted as intensity difference compared to the OPC control sample. One can see the effect of silica concentration on the intensity of reflections. Decrease of the main reflection intensity of portlandite (peak at *ca.* 18° 2θ) and increase in C-S-H reflections (*ca.* 29.4–32.5° 2θ) are shown in Figure 5.8. Semi-quantitative analyses on XRD pattern were carried out by integrating the area of the peaks corresponding to each mineral phase. Results are shown in Figure 5.9 and Figure 5.10. A reduction in portlandite content of *ca.* 40% from the blank sample using the highest silica concentration (20 wt.% solution) has been calculated, confirming the value obtained by thermogravimetric analysis. A total 15% additional C-S-H formed after 14 days, in accordance with the TGA values.

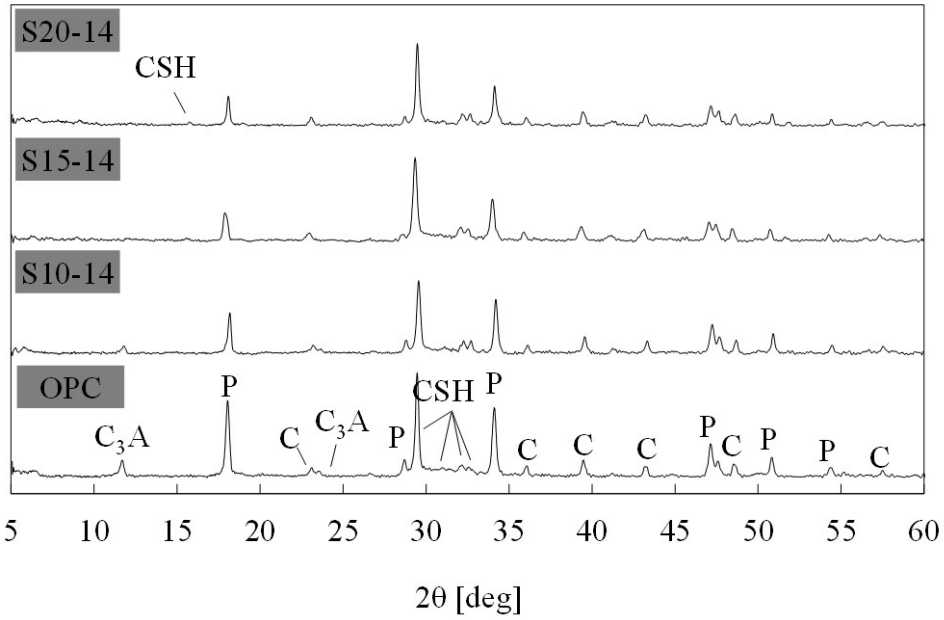

Figure 5.6: XRD analysis of selected samples. List of the major mineral phases. [P: portlandite; C: calcite; C_3A: calcium aluminate; CSH: calcium silicate hydrate].

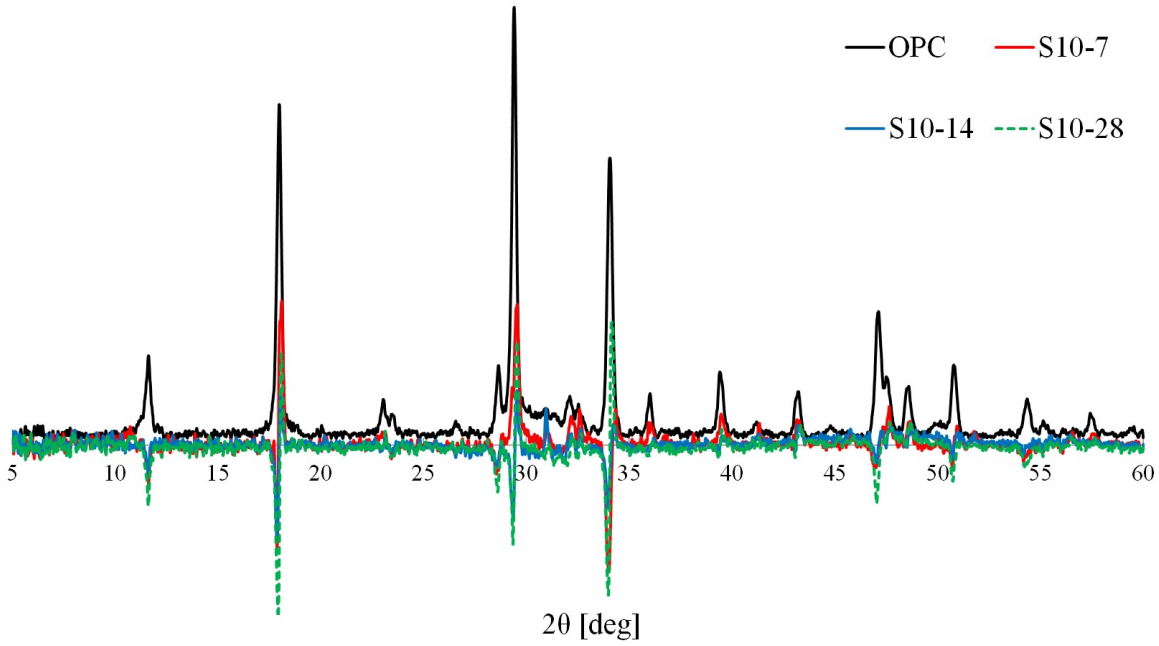

Figure 5.7: Differential plot of XRD patterns of selected samples. Effect of silica concentration on peak intensity.

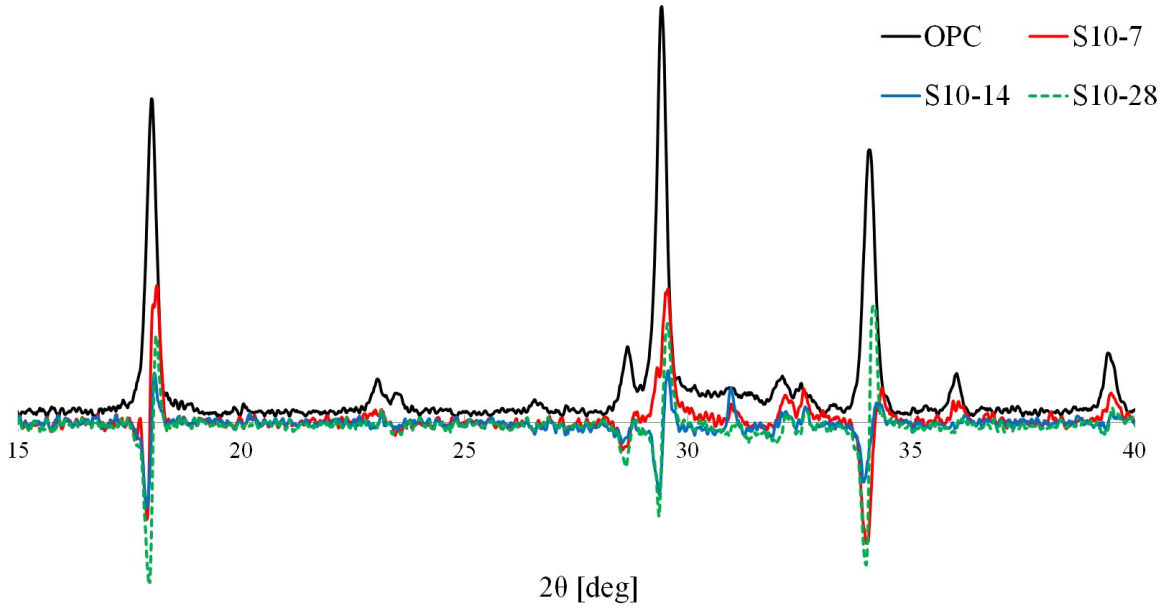

Figure 5.8: Magnification of Figure 5.7. Differential plot of XRD patterns of selected samples. Effect of silica concentration on peak intensity.

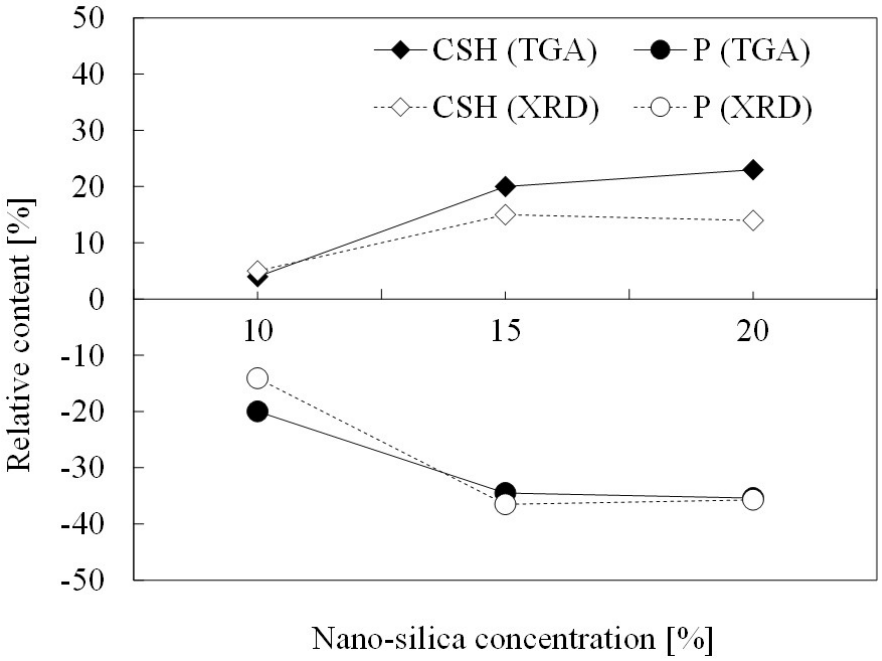

Figure 5.9: Effect of nano-silica solution wt.% on relative increase of C-S-H and decrease of portlandite (P) compared to the OPC control sample for 14 days of injection. Comparison between TGA results and semiquantitavive results based on XRD data

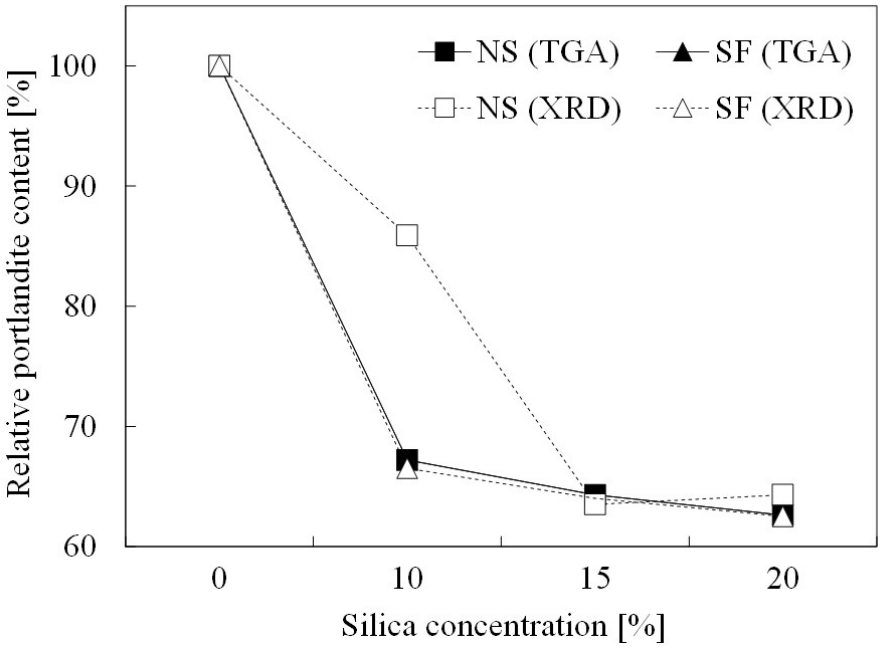

Figure 5.10: Effect of silica particle-size and percentage on the portlandite relative content after 14 days of injection. Comparison between TGA results and semi-quantitative results based on XRD data

5.3.3 SEM analysis and water transport

Back scattering scanning electron miscroscopy (BSE-SEM) images show qualitative information about the silica penetration depth, measured along the direction of silica injection (horizontally left to right in the BSE images), as a arithmetic mean value of 10 measurements in the central area of the cross section. With increasing nano-silica content an increase of penetration depth was observed, due to particle diffusion: *ca.* 500 μm, 630 μm and 740 μm respectively for samples S10-14, S15-14 and S20-14, as shown in Figure 5.11, Figure 5.12 and Figure 5.13. To understand particle penetration depth flow through the blank specimen and linear particle diffusion were calculated. Using Darcy's law (equation 5.3) flow through the blank specimen can be calculated in $m^3\ s^{-1}$.

$$Q = k_s \frac{\Delta h}{L} A \tag{5.3}$$

where k_s is the saturated hydraulic conductivity ($m\ s^{-1}$), L is the thickness of the specimen (in mm), A is the cross sectional area of the sample (962 mm^2) and Δh is the hydraulic head (2000 mm). The value of k_s ($1{\cdot}10^{-13}$ $m\ s^{-1}$) was taken from Christensen et al. [161] for hardened cement paste aged 28 days with w/c ratio of 0.47. The water permeability varies with the degree of saturation, it is assumed that the sample is fully saturated during the injection. However the samples were oven dried before and after the injection and the hydraulic conductivity could be several orders lower than a fully saturated sample. The volumetric flow through the sample is 0.416 $mm^3\ days^{-1}$. After 14 days the calculated total volume of water in the blank specimen is 0.058 cm^3, which is considerably less than the pore volume of the sample, 1.1545 cm^3 and explains why water does not penetrate through the blank specimen after 14 days. The flow velocity in cm/day is $4.32{\cdot}10^{-4}$ indicating that the penetration depth of water into a blank specimen would be 0.06 mm (60 μm) after 14 days. Particle diffusivity was calculated using the Stokes-Einstein equation (equation 5.4):

$$D = \frac{k_B T}{6\pi\eta r} \tag{5.4}$$

where D is the diffusivity of a particle in a straight line ($m^2\ s^{-1}$), k_B is the Boltzmann's constant, T is the temperature in kelvin, r is the radius of the smallest particle size (5 nm diameter) and η is the viscosity of the carrier medium, which is water in this case (Pa·s).

Calculated particle diffusivity is $9.82 \cdot 10^{-11}$ m^2 s^{-1}. Using the equation 5.5, it is possible to calculate the distance travelled, x, as function of the diffusivity D and time t.

$$x = \sqrt{D \cdot t} \tag{5.5}$$

The distance travelled after 14 days by the smallest particle is 344 μm. This value does not take into account the tortuosity (ξ) of the structure. If it is assumed $\xi = 3$ [162], then the distance travelled by the smallest particle is 115 μm which fits reasonably well with the penetration depth of 500–740 μm estimated using SEM images. From mass measurements after particle infiltration and after careful drying of the specimen, the lowest calculated porosity reached is 0.284. The measured open porosity values correlate well with C-S-H production. From TGA analysis and semi-quantitative XRD results it is possible to calculate the volume of C-S-H gel produced (using a C-S-H density value of 2.6 from Allen et al., [163]) and the calculated open porosity of sample S20-14 reduces to 0.21 by pore closing. The measured open porosity of the blank specimen and sample S20-14 are 30% and the 21 % respectively. We suggest the lower measured porosity may result from silica and precipitated C-S-H creating pockets of isolated pores. The reactivity of nano-silica with portlandite has been confirmed through SEM images, TGA and semi-quantitative XRD: particles move through the pores by diffusion, precipitate on portlandite crystals and react with calcium hydroxide forming additional C-S-H or C-A-S-H. Unreacted nano-silica was also observed, lying on the surface of cement paste or occluding pores and void space.

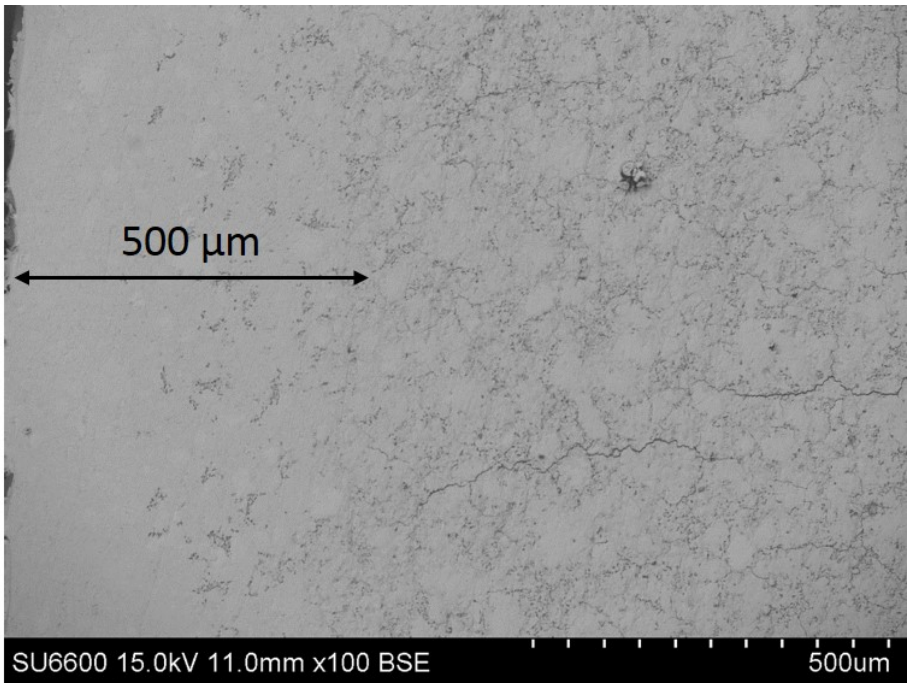

Figure 5.11: BSE-SEM image of samples S10-14 and silica-front measurement.

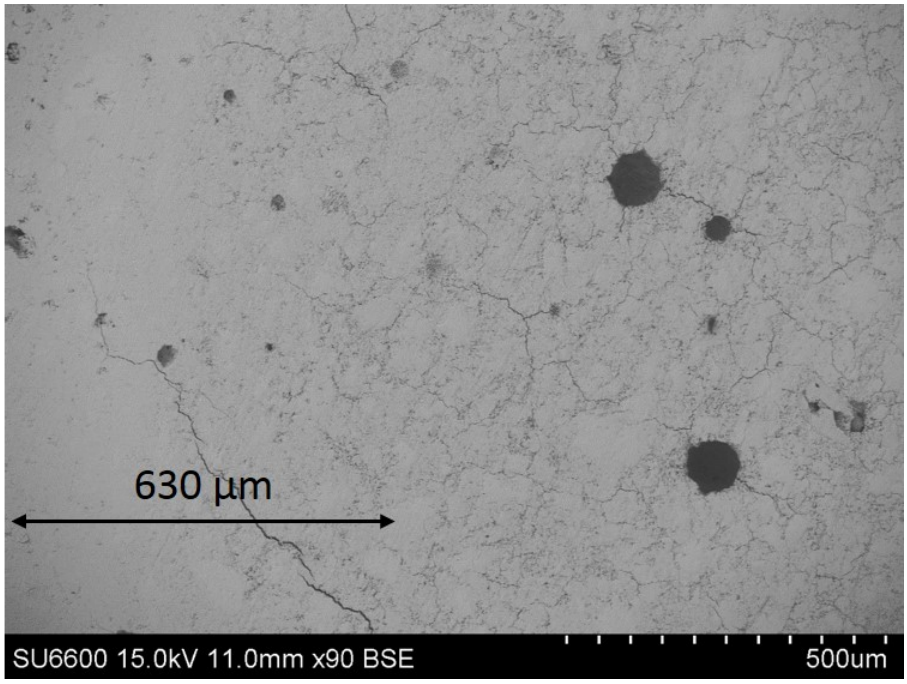

Figure 5.12: BSE-SEM image of samples S15-14 and silica-front measurement.

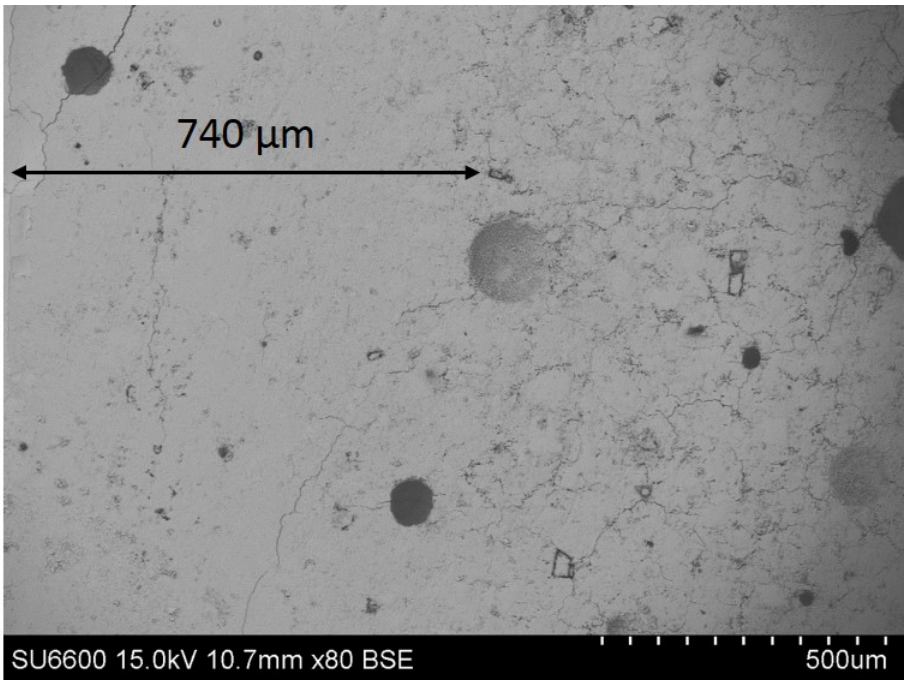

Figure 5.13: BSE-SEM image of samples S20-14 and silica-front measurement.

5.4 Conclusions

In this work we present a novel concrete and cement surface treatment. The following conclusions can be drawn:

- Low-pressure (20 kPa) silica injection has effectively impregnated cement samples. After 14 days of injection with a nano-silica suspension of 20 wt.% concentration it was observed a total reduction of 30% in porosity, suggesting this is a potential consolidant for friable or cracked concrete.
- Nano-silica injection is more efficient than silica fume, due to its smaller particle size allowing it to penetrate further into the pore structure and react to produce more C-S-H.
- Some of the silica injected has reacted with the calcium hydroxide naturally present in hydrated cement, forming additional binding phases such as C-S-H and C-A-S-H. Unreacted silica however has been absorbed and acts as a filler agent reducing porosity.
- After 14 days of nano-silica injection an average penetration depth of *ca.* 750 μm of was measured, which is *ca.* 20% of the cross section of the sample (4 mm).

Chapter 6

Can Portland cement be replaced by low-carbon alternative materials? A study on thermal properties and carbon emissions of innovative cements

Abstract. One approach to decarbonising the cement and construction industry is to replace ordinary Portland cement (OPC) with lower carbon alternatives that have suitable properties. We show that seven innovative cementitious binders comprised of metakaolin, silica fume and nano-silica have improved thermal performance compared with OPC and we calculate the full CO_2 emissions associated with manufacture and transport of each binder for the first time. Due to their high porosity, the thermal conductivity of the novel cements is 58–90% lower than OPC, and we show that a thin layer (*ca.* 20 mm), up to 80% lower than standard insulating materials, is enough to bring energy emissions in domestic construction into line with 2013 UK Building Regulations. Carbon emissions in domestic construction can be reduced by 20–50% and these cementitious binders are able to be recycled, unlike traditional insulation materials.

6.1 Introduction

Ordinary Portland cement (OPC) is one of the most manufactured materials in the world. Over 3 billion tonnes of cement were manufactured in 2012 [164], and global demand is expected to increase due to rapid infrastructural development of emerging economies [165, 166]. Indeed, global cement production is forecast to reach 3.7–4.4 billion tonnes by 2050, as stated by the World Business Council for Sustainable Development (WBCSD) report in 2009 [167]. Cement is primarily used by the construction and geotechnical industries, but there are other emerging applications, including nuclear waste containment, biological and dental ceramics, and water filtration. Cement clinker is produced by calcining limestone (or marl or chalk) with some clay in a furnace at c. 1500 °C and is a significant source of greenhouse gas emissions (GHG), which are usually expressed as CO_2 equivalent (CO_{2eq}) and sometimes referred to as "embedded carbon" [168]. Approximately *ca.* 900 kg of CO_{2eq} is released per tonne of cement produced by current practices [169]. Thus, the cement industry is estimated to contribute 5–7% of global anthropogenic CO_2 emissions in 2009 [22]. The direct release of CO_2 from calcination during clinker production is responsible for *ca.* 50% of the emissions from cement manufacture (Figure 6.1, adapted from Imbabi et al., (2012) [164]). Much of the remaining emissions come from the combustion of fossil fuels for calcination, plus excavation, transportation, milling and grinding processes. Given the global effort to curb CO_2 emissions in an attempt to mitigate dangerous climate change effects [170] (for example the 2015 Paris Agreement, a framework for an internationally coordinated effort to tackle climate change), and the expected rise in global demand for cement, reducing emissions from cement manufacture presents an important challenge. Indeed, the 'decarbonisation' of cement production is becoming a more prominent issue for the cement sector, as evidenced by the WBCSD and International Energy Agency (IEA) Cement Roadmap (2009), the Industrial Decarbonisation & Energy Efficiency Roadmaps to 2050 report and British Cement Association (BCA73 Carbon Strategy 2005) [167, 171, 172].

Researchers and industry have focused their attention on using alternative fuels in place of conventional fossil fuels (and so reducing the GHG emissions of the traditional OPC

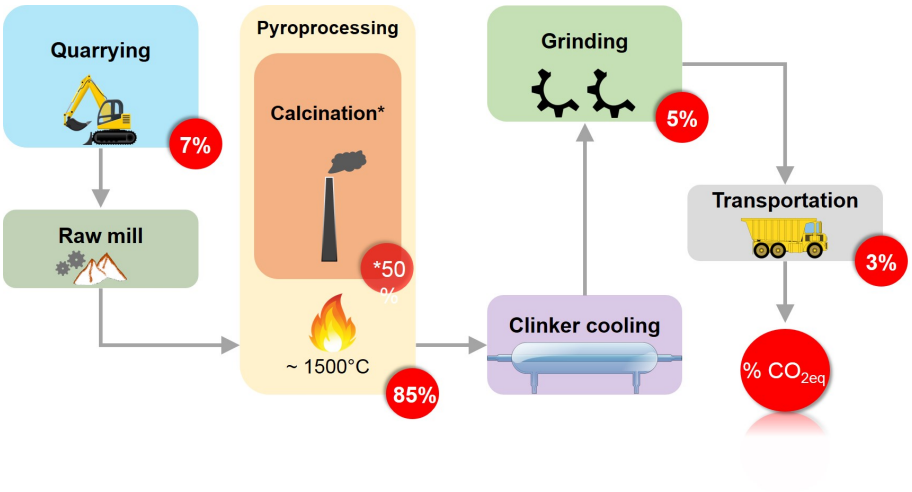

Figure 6.1: Simplified diagram of the cement production process. Red circles indicate the percentage of CO_{2eq} emissions associated with manufacturing. $^{(*)}$50% of the emissions associated with pyroprocessing arises from direct release of CO_2 from calcination and the remaining 35% from fuel and energy consumption. [Image adapted from Imbabi et al., (2012)].

manufacturing process), and developing alternative materials by partially replacing Portland cement with fly ash [173]. Alternative materials that have been developed or tested include reused waste (such as industrial by-products like fly ash or biomass wastes like rice husk ash) and novel binders such as geopolymers or alkali-activated cement [174, 175, 22, 176, 177, 178]. Since these novel binders have low or negative carbon emissions associated with their production, they are sometimes referred to as "green cements" [179]. In most cases, the alternative materials only partially replace clinker. This is advantageous from a regulatory perspective since the existing standardised codes of practice for OPC can be adapted or built upon. It is important that the mechanical properties of alternative cements are similar to (or more advantageous than) the properties of OPC. Recent studies have found that some OPC novel binder mixtures such as lime-metakaolin have suitable properties [180] and might be preferable to OPC in humid environments [181]. Other novel additives such as silica fume and nano-silica particles improve the properties of OPC [182, 183, 184, 185] and metakaolin-based geopolymers [186, 29]. The main reason geopolymer binders have not yet been more widely adopted by industry is the current lack of regulatory standards backed by long term testing and development [187].

OPC is used in the preparation of mortar for wall rendering/finishing and also in aerated concrete blocks employed as a thermal insulation material [188, 37]. However, aerated OPC

does not offer thermal conductivity values comparable to other solutions on the market, such as polymer foam, glass fibres and vacuum insulation panels [189]. Although these materials have very low thermal conductivity, in the range 0.01–0.002 W m^{-1} K^{-1} [190, 191], which can help reduce energy consumption, their production is polluting [192, 193] plus they cannot entirely be recycled and have to be disposed of in landfill. Geopolymer binders and OPC-free mixtures have been proposed as alternative insulation materials to OPC-based composites and have shown thermal conductivity values, 0.17–0.35 W m^{-1} K^{-1}, lower than traditional cement mortar or concrete (0.2–0.8 W/(m K) [194]) although not comparable with insulation materials such as glass fibres or polymers [29].

Life cycle analyses on selected geopolymer binders have found that their use in place of OPC could reduce GHG emissions from the cement industry by 9–64% [195, 22]. However, these life cycle emissions are context and country dependent and often subjected to availability of raw materials [196, 197, 198]. To date, the environmental sustainability of a range of OPC free cement mixtures has not been comparatively explored, nor has there been a comprehensive analysis of properties of alternative cements and their potential to completely replace OPC. Here it is considered the carbon reduction that could be achieved by using seven alternative cementitious materials in place of OPC, evaluate CO_{2eq} gas emissions of OPC and geopolymer production, taking the whole life-cycle into account, including the transport of raw materials and the manufacturing process [164].

The aim of this work is to develop novel *'green'* cementitious materials with superior thermal properties to ordinary Portland cement and low environmental impact. Silica particles, metakaolin and calcium hydroxide are combined in binary or ternary systems and their physical, thermal and mechanical properties are characterised. Thermal performance is calculated in the context of a typical domestic construction and a comparison of GHG emissions for these novel cementitious binders and OPC is presented for the first time in the UK-European context. These OPC-free cements represent an environmental friendly alternative with a high recyclability potential, simple manufacturing process and able to ensure thermal comfort within current international standards. Furthermore, GHG emissions are calculated following a simplified life cycle assessment, which provide a useful decision-making tool to industries or

practitioners to rapidly calculate the carbon footprint of novel OPC-free binders.

6.2 Materials and methods

6.2.1 Materials

Portland cement samples were prepared using ordinary Portland cement CEM I 42.5-R (CAS number 65997-15-1), commercially available from the Lafarge Cement Group, and deionised water (W). Physico-chemical properties of Portland cement are listed in Table 6.2. Cement samples (OPC) were prepared with a liquid to solid (l/s) ratio of 0.3 using a rotary mixer according to BS EN 196-1:2016 and cast into cubic molds for 24 hours. After 24 hours samples were kept for 28 days at RH 98 ± 2% and temperature of 21 ± 2 °C in a nitrogen gas environment to minimise carbonation prior to testing. Novel OPC-free cement samples were prepared using different starting materials. Reagent grade calcium hydroxide, $Ca(OH)_2$ (CAS Number 1305-62-0) and Ludox T50 nano-SiO_2 aqueous suspension (CAS number 7631-86-9) were purchased from Sigma Aldrich. Silica fume (CAS number 69012-64-2), commercially available as SF920D from Elkem Microsilica (Norway), was used. Metakaolin was obtained from calcination of kaolin (China clay type purchased from Imerys UK, CAS number 1332-58-7) at 750 °C over 24 hours, as described by Alonso et al., (2001) [199]. Reagent grade sodium hydroxide, NaOH (CAS number 1310-73-2) of nominal concentration 10 M was purchased from Fisher Chemical. Chemical and physical properties of the starting materials (calcium hydroxide (CH), nano-silica (NS), metakaolin (MK), silica fume (SF)) are reported in Table 6.3. Given the pozzolanic reactivity of nano-silica and amorphous silica fume, binary mixes using calcium hydroxide and silica (nano-silica or silica fume) were investigated (samples CHI, CHI10, CHNS). Alkali activated binders were prepared mixing metakaolin with calcium hydroxide in different proportions. Sodium hydroxide 10 M was added as an activator (sample MK10, AMK, BMK). Finally metakaolin was mixed with nano-silica and calcium hydroxide, using lower concentration NaOH (1 M) as activator (sample MKNS). Mix proportions and sample identification are listed in Table S3 in the Supporting Information. Fresh paste was cast into cubic moulds and specimens were kept for 28 days at RH 98 ± 2% and temperature

of 21 ± 2 °C in a nitrogen gas environment to minimise carbonation. Sample MK10 was thermally prepared following the methodology of Zhang et al., (2014) for geopolymers [200]. After mixing, specimens were cast into a cubic mould and kept in an oven at 60 °C and atmospheric pressure for 24 hours, then placed in a sealed environment for 28 days at RH 98 ± 2% and temperature of 21 ± 2 °C.

Table 6.1: Characteristic of CEM I (Class 42.5 R) Portland cement (according to the certificate of conformity, test method BS EN 196-2).

Components	CEM I
Clinker	96%
Gypsum added	4.0%
Chemical composition (>0.2%)	
SiO_2	19.3%
Al_2O_3	4.9%
Fe_2O_3	2.9%
CaO	63.4%
MgO	1.3%
SO_3	2.3%
Na_2O	0.23%
L.O.I.	2.27%
Density (kg m^{-3})	3300
Specific area (m^2 g^{-1})	420
Compressive strength at 28 day (MPa)	51.2

6.2.2 Physical, thermal and mechanical properties

After ageing for 28 days samples were removed from the mold and dried at 60 °C to remove pore water and perform mechanical tests and micro-structural analyses. Water removal has an impact on the microstructure, therefore analysis and results presented should be regarded comparatively. Compressive strength testing was performed according to BS EN 196-1:2016, using a uniaxial compressive testing machine at a constant strain rate of 0.4 mm min^{-1} until fracture [183, 201]. Three specimens of each composite were tested. The resistance value (R_c) is given in MPa as a mean value of three replicates for each mixing. It must be noted that the drying procedure followed has an influence on mechanical behaviour; compressive strength

Table 6.2: Characteristic and chemical composition of calcium hydroxide (CH), nano-silica (NS), silica fume (SF), metakaolin (MK) and sodium hydroxide (NaOH).

Components	CH	NS	SF	MK	NaOH 10M
State	powder	suspension	powder	powder	liquid
Chemical composition (>0.2%)					
SiO_2	-	50%	99.9%	47%	-
Al_2O_3	-	-	-	38%	-
$Ca(OH)_2$	95%	-	-	-	-
NaOH (% w$\check{}$)	-	-	-	-	40%
Water	-	50%	-	-	60%
pH	12.4 (slurry)	8.5-9.5	-	-	>12.0
Particle size diameter (nm)	-	5-20	100-1000	700-2000	-
Density (kg m^{-3})	2240	1400	2200	2600	1320
Specific area (m^2 g^{-1})	20-41	110-150	15–30	14	-

Table 6.3: Sample mixes and proportions of starting materials and liquid to solid (l/s) ratio, including OPC.

Sample	OPC %	CH %	NS %	SF %	MK %	W l/s	NaOH 10 M l/s	NaOH 1 M l/s
OPC	100	-	-	-	-	0.3	-	-
CHI	-	75	-	25	-	0.6	-	-
CHI10	-	75	-	25	-	-	0.8	-
MK10	-	-	-	-	100	-	0.8	-
AMK	-	75	-	-	25	-	1	-
BMK	-	66	-	-	33	-	1	-
MKNS	-	10	5	-	85	-	-	1
CHNS	-	50	50	-	-	2	-	-

values are approximately 10% higher for air-dried than saturated cement paste [202, 203]. The heat of hydration was measured using an isothermal calorimeter (I-Cal 4000 HPC, Calmetrix). Fresh paste (*ca.* 60 g) was cast into a cylindrical container and placed into the calibrated calorimeter, at a constant temperature of 21 ± 2 °C. The heat flow was recorded over 80 hours. Open porosity (φ) was estimated by measuring the total water content in each sample (in three replicates) after oven-drying at 60 °C and overnight saturation in a vacuum chamber. Open porosity was calculated using equation 6.1:

$$\varphi = \frac{m_s - m_d}{V \varrho_w} \tag{6.1}$$

where φ is the open porosity, m_s is the sample water saturated mass (kg), m_d is the sample dried mass (kg), V is the volume of the sample (m^3) and ϱ_w is the density of water at 20 °C (kg m^{-3}). Bulk density (ϱ) and matrix density (ϱ_{mat}) in kg/m^{-3} were calculated respectively using equations 6.2 and 6.3

$$\varrho = \frac{m_d}{V} \tag{6.2}$$

$$\varrho_{mat} = \frac{m_d}{V(1-\varphi)} \tag{6.3}$$

For each sample the laser flash method (LFA) was used to estimate the coefficient of thermal conductivity (λ), given in W m^{-1} K^{-1}. A Netzsch instrument 427 LFA was used. Samples of each composition were tested in an argon atmosphere and thermal conductivity was calculated according to the BS EN 821-2:1997. The specimens were powdered and pelletized using an hydraulic press to make pellets of ⌀12.7 mm and 3 mm thickness. The surface was coated with graphite to minimise reflectance of the laser beam. A pyroceramic standard supplied by Netzsch was analysed and used as a reference material to calculate the specific heat capacity and thermal diffusivity. Thermal conductivity was calculated at 25, 60 and 105 °C using the equation 6.4:

$$\lambda_p = \alpha c_p \varrho \tag{6.4}$$

where λ_p is the thermal conductivity of the pelletized sample in W m^{-1} K^{-1}, α is the

thermal diffusivity ($m^2\ s^{-1}$), c_p is the specific heat capacity at constant pressure in J kg^{-1} K^{-1}. Assuming the porosity of the pelletized sample is negligible, the effective thermal conductivity of the bulk sample is given by the equation 6.5:

$$\lambda = \lambda_a \varphi + \lambda_p (1 - \varphi) \tag{6.5}$$

where λ_a is the thermal conductivity of the air at the given temperature (W m^{-1} K^{-1}), and φ is the open porosity of the sample. The thermal conductivity value of the novel cement paste is then used for the calculation of the thermal transmittance of a typical composite wall, given in (m^2 K W^{-1}), according to the BS EN ISO 6946:2007.

The thermal transmittance value of a typical composite wall, is estimated using the equation 6.6:

$$U = \frac{1}{R_T} \tag{6.6}$$

where U is the total transmittance value of a composite wall in W m^{-2} K^{-1} and R_T is the total thermal resistance, in m^2 K W^{-1}. The thermal resistance R_T can be calculated according to the equation 6.7:

$$R_T = R_{si} + \sum_{i=1}^{n} (R_i) + R_{se} \tag{6.7}$$

where R_{si} and R_{se} are the internal surface resistance and the external surface resistance respectively in W m^{-2} K^{-1}, and R_i is the design thermal resistances of each layer, and n is the number of layers. The resistance of each layer, in m^2 K W^{-1} is calculated using the equation 6.8:

$$R_i = \frac{d}{\lambda} \tag{6.8}$$

where d is the thickness of the material layer in the component (m) and λ is the thermal conductivity calculated according equation 6.5 or obtained from tabulated values.

In order to evaluate the insulation properties of these novel cement composites, the thermal transmittance (U) of a typical wall was calculated. An external wall (1 m high and 1 m wide) of standard domestic construction was considered, as shown in Figure 6.8 (*left*). The wall

consists (from outdoor to indoor) of horizontal bricks (225 × 112 × 65 mm BS EN 771-1:2011, $\lambda = 0.84$ W m^{-1} K^{-1}) with a 5 mm layer of cement mortar ($\lambda = 1.4$ W m^{-1} K^{-1}, [190]) and externally finished with 18 mm thickness of mortar render ($\lambda = 1.4$ W m^{-1} K^{-1}). Adjacent to the outer brick skin is a 20 mm thick air cavity ($\lambda = 0.03$ W m^{-1} K^{-1}), 9 mm layer of plywood ($\lambda = 0.14$ W m^{-1} K^{-1}), a rock-wool insulation wall of 40 mm thick ($\lambda = 0.04$ W m^{-1} K^{-1}, [189]) and a 15 mm thick gypsum plaster board ($\lambda = 0.21$ W m^{-1} K^{-1}, [190]) finished with 2 mm thick waterproof plaster painting ($\lambda = 0.09$ W m^{-1} K^{-1}, [190]). The wall is then finished with an outside mortar render and internal plaster. This is a pattern in the construction that repeats itself every 70 cm in the vertical direction. Therefore a 1 m wide and 0.7 m high portion of the wall was considered, as it is representative of the entire wall. One-directional heat transfer and constant thermal conductivity values are assumed.

6.2.3 Powder X-Ray Diffraction and Scanning Electron Microscopy

Powder XRD analyses were performed using a Bruker D8 Advance diffractometer with CuKα radiation over the range 5–60° 2θ, step size of 0.02° 2θ and 0.5 s step^{-1}. DiffracEva software from Bruker was used for XRD pattern evaluation and phase identification. Microstructural analysis of samples was carried out using tungsten emission scanning electron miscroscopy (W-SEM) and field emission scanning electron microscpy (FE-SEM) (W-SEM, Hitachi S-3700N and FE-SEM, Hitachi SU6600) with Energy Dispersive Spectroscopy (EDS, Oxford INCA-7260) at an accelerating voltage of 10–15 kV. All samples were resin impregnated, polished and gold coated.

6.2.4 Greenhouse gas emission assessment

Calculation of the total greenhouse gas emission (GHG), expressed as carbon dioxide equivalent (CO_{2eq}) per 1000 kg of cement produced, takes into account the collective contribution of CH_4, NO_x, SO_x, CO_2 and synthetic gases evolved during production activity, including excavation and transport of raw materials and reagents, and manufacturing. The approach to estimate the total GHG is based on the methodology reported in McLellan et al., (2011) [195] and

calculated using the equation 6.9:

$$GHG_{Tot} = \sum_{i=1}^{n} m_i(d_i e_i + p_i) \tag{6.9}$$

where GHG_{Tot} is the total greenhouse gas emission ($kg_{CO_{2eq}}$) per tonne of material produced, m_i is the fraction of component i, d_i is the distance transported by a given mode of transport (km), e_i is the emission factor for the transportation mode ($kg_{CO_{2eq}}$ km^{-1} $tonne^{-1}$) and p_i is the emissions per unit mass of component i produced ($kg_{CO_{2eq}}$ $tonne^{-1}$). The following assumptions were made in the analysis:

1. The calculations were based on the manufacture of 1 tonne of Portland cement binder and 1 tonne of novel materials in the United Kingdom, using, where possible, UK products, otherwise materials from a typical supply chain.
2. Previously published values for CO_{2eq} emissions from the manufacture of the raw materials were used, and added to the emissions from transport to and within the UK.
3. The emissions due to the addition of water to cement paste are very low (0.271 $kg_{CO_{2eq}}$ $tonne^{-1}$ [204]) therefore negligible and not taken into account.
4. Maximum distances and mode of transport are selected as those which maximise CO_{2eq} emissions, because this work adopts the worst-case scenario for CO_{2eq} emissions.
5. Emission factors associated with road transport (e_r) and sea transport (e_s) are respectively 0.09 $kg_{CO_{2eq}}$ km^{-1} $tonne^{-1}$ and 0.02 $kg_{CO_{2eq}}$ km^{-1} $tonne^{-1}$ [195, 205].
6. Emissions per unit mass of OPC (p_{OPC}) are 750 $kg_{CO_{2eq}}$ $tonne^{-1}$ and is produced in mainland UK [195].
7. Emissions per unit mass of metakaolin (p_{MK}), produced in England and silica fume (p_{SF}), produced in Norway, are respectively 236 $kg_{CO_{2eq}}$ $tonne^{-1}$ and $7{\times}10^{-6}$ $kg_{CO_{2eq}}$ $tonne^{-1}$ [206, 195].
8. The manufacture of calcium hydroxide is based on the hydration of calcium oxide, produced in Northern Ireland, (p_{CO} = 750 $kg_{CO_{2eq}}$ $tonne^{-1}$) taking into account a correction factor of 0.97 due to the addition of water (p_{CH} = 720 $kg_{CO_{2eq}}$ $tonne^{-1}$) as explained in the IPCC Guidelines for national greenhouse gas emissions [207].
9. Sodium hydroxide is produced in Northern Ireland by a chemical process using electro-

lytic cells. The emissions associated with the production are in the range 1120–1915 $kg_{CO_{2eq}}$ $tonne^{-1}$ as reported for a nominal concentration of 16 M [22, 205, 208]. In order to take into account lower sodium hydroxide concentrations, a correction factor of 0.43 and 0.63 was used, respectively for NaOH 1 M and NaOH 10 M on the lowest emission value ($p_{NaOH} = 1120$ $kg_{CO_{2eq}}$ $tonne^{-1}$), following the principle of the IPCC guidelines [207].

10. Nano-silica solution is manufactured in Germany and the carbon emissions value can be obtained from the manufacture of sodium silicate solution ($p_{NS} = 386$ $kg_{CO_{2eq}}$ $tonne^{-1}$) [209, 81, 185].

A schematic diagram of mode of transport and distances for each raw material is shown in Figure 6.2.

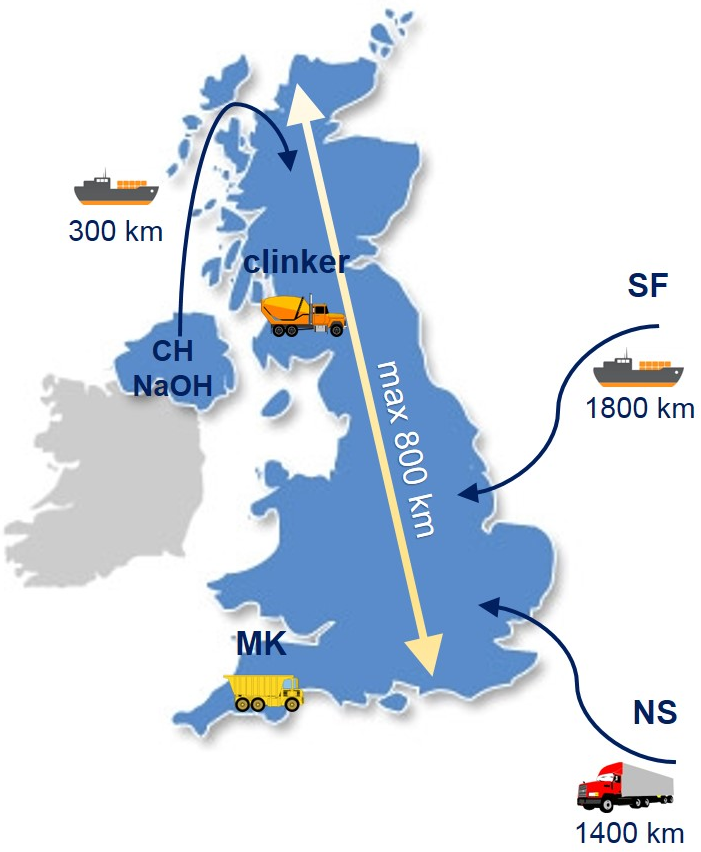

Figure 6.2: Diagram of transportation mode and average distance for raw materials in and to UK. Silica fume (SF) is supplied from Norway, nano-silica (NS) from Germany, calcium hydroxide (CH) and sodium hydroxide (NaOH) from Northern Ireland (UK), metakaolin (MK) and Portland clinker are available in mainland UK.

6.3 Results and discussion

6.3.1 Physical, thermal and mechanical properties

The particle size and the high specific surface area of nano-particles play an important role in the physical and mechanical properties. The measured bulk density (ϱ), matrix density (ϱ_{mat}), open porosity (φ), compressive strength (R_c) results and cumulative heat released values are reported in Table 6.4. All the mixes show values of bulk density in the range 600–1100 kg m^{-3}, much lower than standard OPC (1900 kg m^{-3}). Density and porosity values are in good agreement with literature data on lightweight materials such as calcium silicate boards and aerated concretes [51, 210, 211]. Sample CHI10 shows a higher bulk density and lower porosity due to the greater l/s ratio and the presence of an alkaline activator. Samples MK10, AMK and BMK show decreasing density values directly proportional to the content of metakaolin, from 100% to 66%. On the other hand porosity increases when a lower amount of MK is used (sample MKNS) and higher concentration of nano-silica is used (sample CHNS). Mechanical tests performed on all the samples after 28 days of curing show values of compressive strength, in the range of 1.8–7.8 MPa. Although compressive strength values are not comparable with OPC, they satisfy the resistance requirement for non-loaded structures; results are in agreement with the values given for aerated concrete blocks [212, 213] and lime-metakaolin mortars [214, 215]. Isothermal calorimetry was used to measure the heat flow development of the samples at 21 °C. Figure 6.3 shows the heat flow of the samples compared to OPC. Since the mixing was done externally, the first peak appears at the very beginning of the measurement for all the samples (Figure 6.3a); it corresponds to particle wetting and dissolution, the chemical reaction which leads to the formation of hydrated phases. The second peak appears broad and delayed compared to OPC. It corresponds to the polymerisation of dissolved species into new crystal structures. In sample CHI the first peak converges into a straight horizontal line and no second peak is detected, indicating very low reactivity [50]. Sample CHI10 shows the influence of the alkali-activator, resulting in higher intensity and accelerated reaction. Specimen CHNS (CH and NS) shows the same trend of mix CHI (CH and SF), with a high first peak converging into a horizontal line. However a second peak is

detected as a broad hump at around 20 hours. This is due to the smaller particle size and higher reactivity of NS compared with SF. Sample MK10 shows a high-intensity broad first peak followed by small broad hump associated with the second peak of hydration. Samples AMK and BMK have respectively 75% and 66% of calcium hydroxide content. In sample BMK, the higher content of MK produces a delay in the second peak compared to sample AMK. The peak is higher in intensity from the increased formation of alkaline aluminosilicate due to the greater concentration of dissolved aluminium ions [199]. The cumulative heat released in the first 80 hours was obtained by integrating the heat flow curves and is summarised in Table 6.4. Except for the mix MK10, with a total heat release of 440 J g^{-1} due to the presence of NaOH 10M that acts as an accelerator, in accordance with the work of Zhang et al., (2012) [216], all the other mixes show a cumulative energy lower than OPC, due to the lower number of reactants dissolved. Cumulative heat released is shown in Figure 6.4. OPC clinker is a complex mixture of compounds and usually gypsum is added to delay the setting time.

Table 6.4: Bulk density (ϱ), matrix density (ϱ_{mat}), open porosity (φ), compressive strength (R_c) and cumulative heat release (H) of all the samples.

Sample	ρ kg m^{-3}	ρ_{mat} kg m^{-3}	φ -	R_c MPa	H J g^{-1}
OPC	1940	2460	0.21	51.2	235
CHI	940	2430	0.61	6.4	44
CHI10	1120	2160	0.48	7.7	211
MK10	1020	2190	0.53	5.2	463
AMK	900	2180	0.59	4.7	75
BMK	850	2020	0.58	6.5	104
MKNS	640	2260	0.72	1.7	51
CHNS	610	2390	0.74	2.2	148

6.3.2 Powder X-Ray Diffraction and Scanning Electron Microscopy

Figure 6.5 presents the XRD patterns obtained for the developed materials, where only the major mineral phases are shown. Samples CHI and CHI10 are mainly crystalline portlandite (P) and semi-crystalline calcium silicate hydrate gel (C-S-H), the most abundant component of hydrated cement paste and responsible for early strength development and hardening [8] or

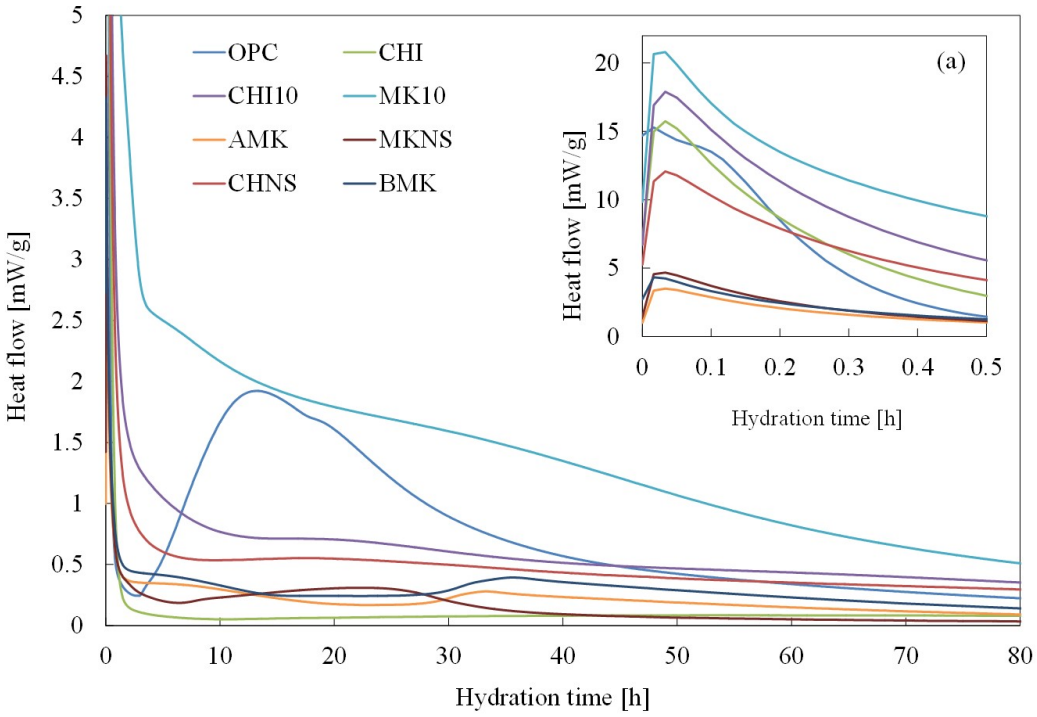

Figure 6.3: Heat flow measurement for each sample. (a) magnification of the first 30 min of heat flow measurement.

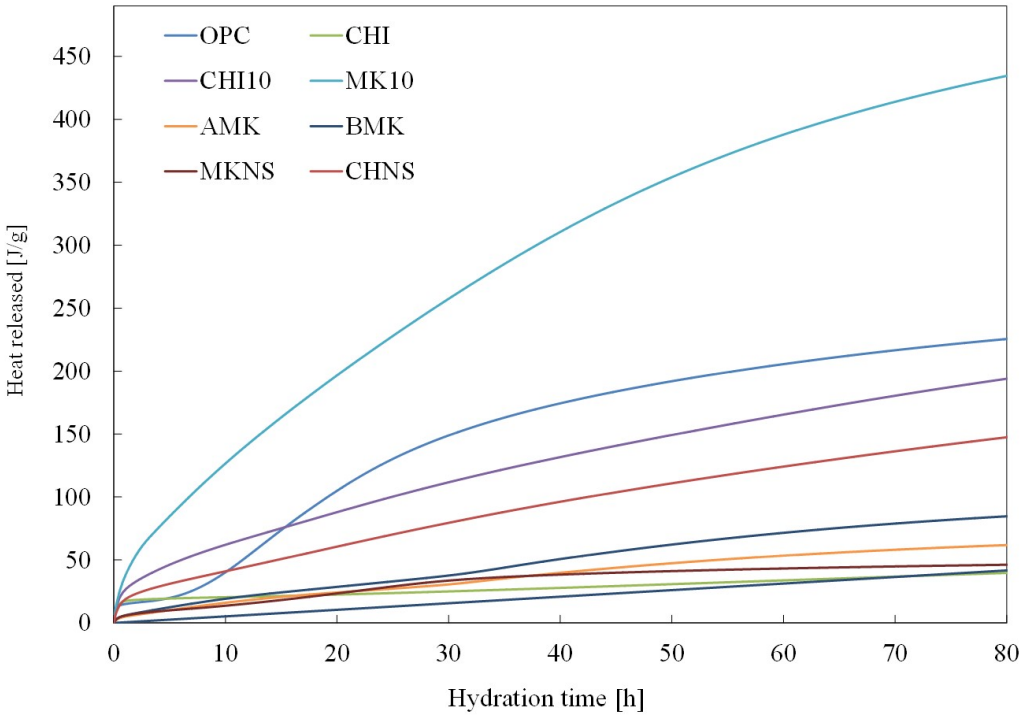

Figure 6.4: Heat of hydration (cumulative heat released, in J g^{-1}) of each mix calculated as a function of time.

calcium (sodium) silicate hydrate (C-(N)-S-H) [217, 218]. Semi-quantitative analysis of the XRD patterns showed that, despite the high pH, sample CHI10 has 54% C-S-H compared to sample CHI (61%). The added Na^{+} concentration takes Ca^{++} to produce C-N-S-H in addition to the C-S-H produced. Some minor carbonated phases are detected, (calcite, carbon, and sodium carbonate), arising from surface carbonation. In the mixes containing metakaolin and calcium hydroxide (sample AMK, BMK and MKNS), stratlingite (St), calcium aluminate hydrate (C-A-H) and monocarboaluminate (M) phases are detected, in agreement with Silva et al., (2014) [181]. Stratlingite is the main hydrate phase responsible for strength development in lime-metakaolin based materials. An increase of metakaolin content from 25% to 35% respectively in samples AMK and BMK results in well defined peaks of stratlingite, and consequently higher compressive strength. Faujasite (F) is the main crystalline compound in sample MK10 along with C-S-H gel, calcium aluminate hydrate and minor stratlingite. In sample MK10, mixing metakaolin with 10 M NaOH solution promotes alkaline activation and leads to the precipitation of sodium aluminum silicate hydrate (N-A-S-H) gel into the mineral structure of faujasite (F) [200, 219]. In sample MKNS, reducing the concentration of the activator from 10 M to 1 M and the addition of calcium hydroxide at ambient temperature results in the precipitation of semi-crystalline calcium aluminate hydrate (C-A-H), the main phase detected. Sample CHNS presents broad humps at *ca.* 29° and 32° 2θ, typical of C-S-H gel [54].

As shown in the SEM images, the developed materials present a highly porous matrix in agreement with the density and porosity values measured. In sample CHI the matrix is mainly semi-crystalline C-S-H whereas the presence of NaOH as alkaline activator in sample CHI10 promotes the formation of C-S-H combined with C-(N)-S-H phases, respectively in Figure 6.6a and Figure 6.6b. As shown in XRD patterns, alkali-activation of metakaolin-lime mixes results in formation of calcium aluminate silicate hydrate (stratlingite) and C-S-H (sample BMK, Figure 6.6c). Figure 6.6d shows a semi-crystalline C-S-H phase forming a complex plate-like structure in sample CHNS.

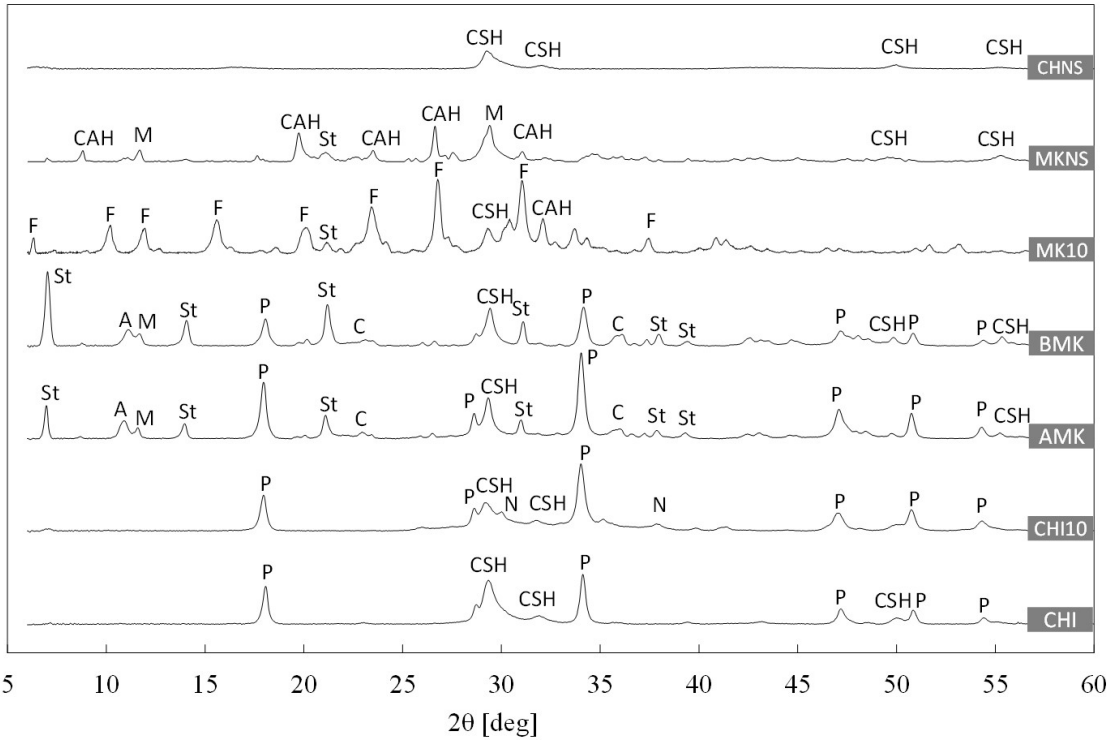

Figure 6.5: XRD patterns of each sample and major mineral phases. [P: portlandite; CSH: calcium silicate hydrate; C: calcite; St: stratlingite; M: monocarboaluminate; A: tetracalcium aluminate hydrate; F: faujasite; CAH: calcium aluminate hydrate; K: katoite; N: Natrite.]

6.3.3 Thermal conductivity measurements

Thermal conductivity values at 25, 60 and 105 °C calculated according to equation S5 are shown in Figure 6.7 and compared to OPC. Values are in the range 0.05–0.26 W m^{-1} K^{-1}, 50–90% lower than OPC. Samples made mixing metakaolin and sodium hydroxide (MK10, AMK and BMK) show thermal conductivity values in accordance with Palmero et al., (2015) and Villaquiran-Caicedo et al., (2015) [211, 29]. Furthermore samples show an inversely proportional trend to the content of MK 100, 75 and 66 wt.% respectively. The addition of silica nano-particles has a beneficial effect on the thermal conductivity. Sample MKNS and CHNS in fact show the lowest λ values at 25 °C, 0.055 and 0.088 W m^{-1} K^{-1} respectively. These values are typical of insulating materials [220, 190]. This effect is attributed to the nano-silica smaller particle size range and greater surface area, which increases the pore volume ($\varphi = 0.7$) and decreases the pore-size; the overall consequence is an enhanced phonon scattering

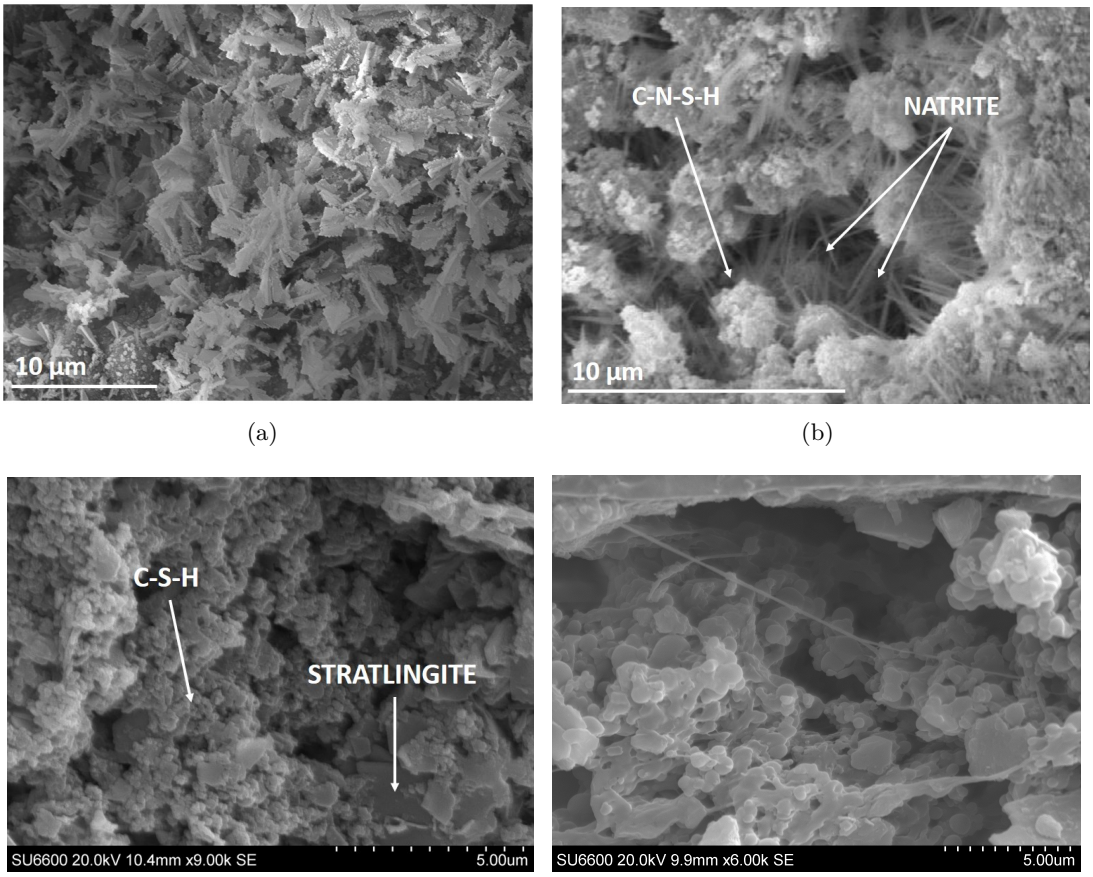

Figure 6.6: SEM images of (a) sample CHI showing a poorly crystallised C-S-H phase flake-shaped [FE-SEM, acceleration voltage 15 kV]; (b) sample CHI10 showing semi-crystalline C-N-S-H phase and natrite needles [W-SEM, acceleration voltage 15 kV]; (c) sample BMK showing a porous microstructure formed by stratlingite and C-S-H [FE-SEM, acceleration voltage 20 kV], and (d) sample CHNS showing a porous microstructure formed by plate-like C-S-H phase [FE-SEM, acceleration voltage 20 kV].

effect which reduces heat transfer [221]. Samples made by mixing CH and SF, either with water or alkali-actived show a different thermal behaviour: while sample CHI has a thermal conductivity value ($\lambda = 0.09$ W m^{-1} K^{-1}) similar to CHNS, sample CHI10 has a higher λ, suggesting that the alkali-activator (NaOH, 10 M) contributes to the reduction of porosity and decreases the thermal transmittance. As shown in XRD patterns, sample CHI contains C-S-H and portlandite, whereas CHI10 is made of C-S-H, natrite and portlandite, bound together in a denser and less porous matrix (*ca.* 20% less than CHI).

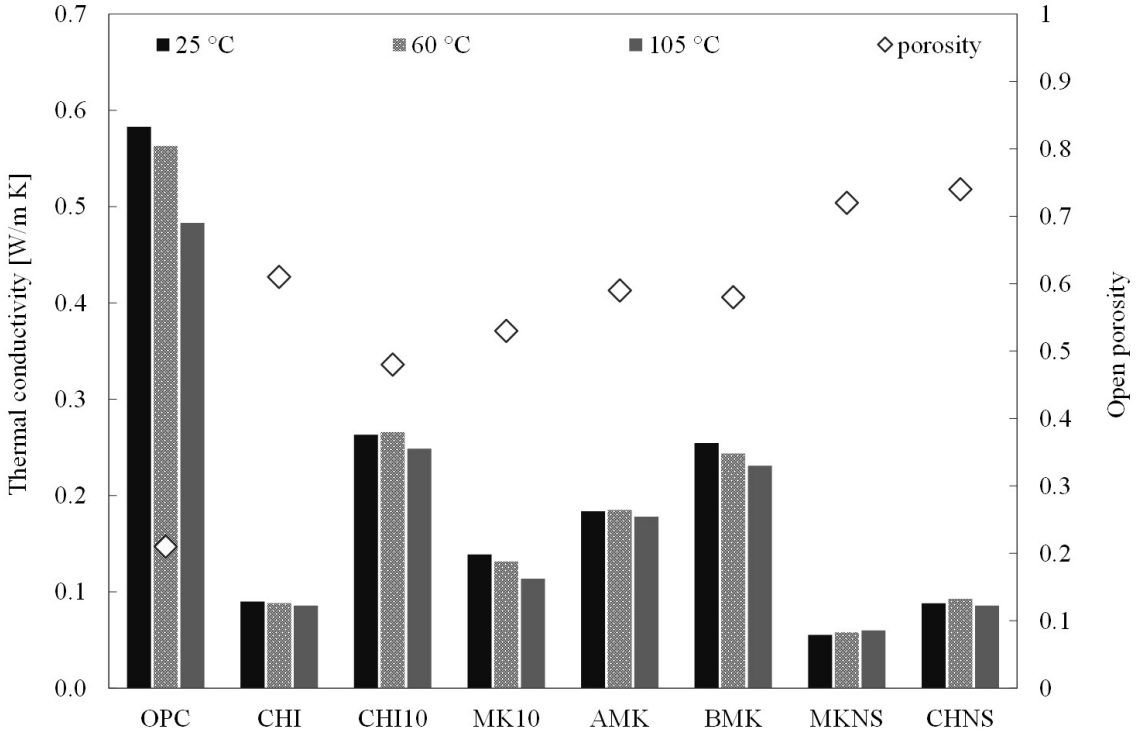

Figure 6.7: Thermal conductivity of samples at 25, 60 and 105 °C and porosity values compared to OPC.

Thermal transmittance (U-value) for the typical wall (Figure 6.8) was calculated to be 0.32 W m^{-2} K^{-1}, using equation 6.6. Building Regulation 2013 in England and Wales for refurbishment of existing buildings (domestic and non-domestic use) requires values less than 0.30 W m^{-2} K^{-1}. The application of a layer of novel cementitious material can contribute to the reduction of the total transmittance below the limit imposed by Building Regulations 2013. The U-value was then calculated taking into account an additional layer of developed material placed in between the bricks and the air cavity. The thickness was chosen in order to minimise

the total transmittance below the limit of the building regulations. Thickness values of all the mixes are summarised in Table 6.5. The thickness of insulation material layers used in the construction industry is in the range of 30–100 mm (e.g. glass fiber, rock-wool or polymeric foam [190]). A 20 mm layer of mix MKNS is required to reduce the total transmittance by 10%, as shown in Figure 6.8. Conventional insulation materials such as rock-wool, polystyrene or glass fibres, are usually placed in layers of *ca.* 40–80 mm [191, 222].

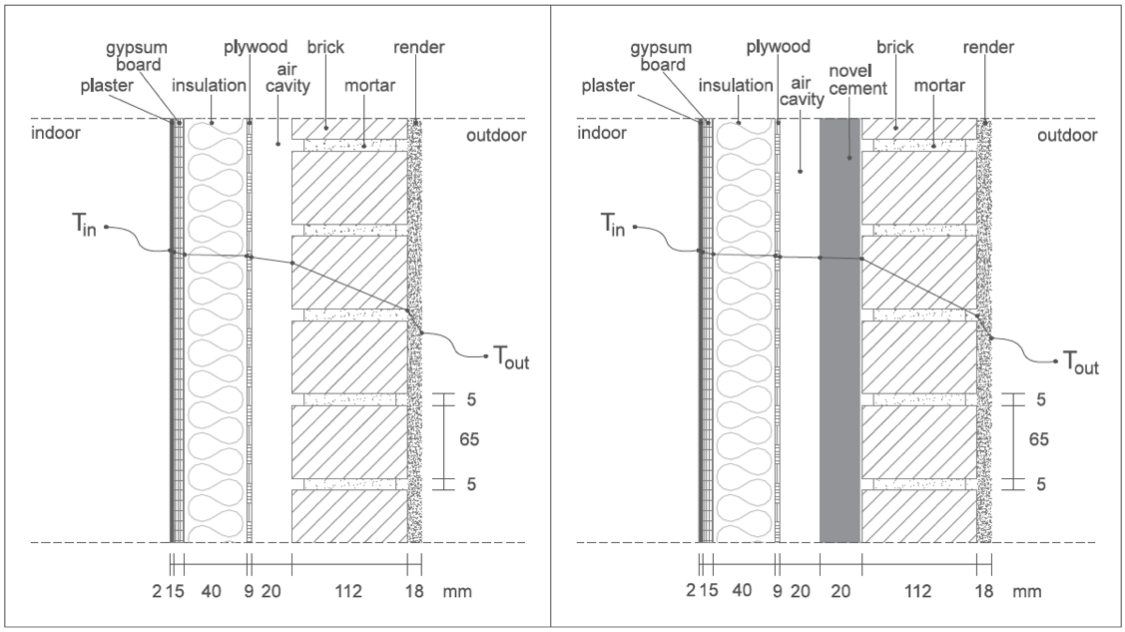

Figure 6.8: Typical external composite brick wall of domestic building in United Kingdom. [Wall-section and temperature (T) profile (*left)*. Wall-section including a layer of MKNS and temperature profile (*right*)]

6.3.4 Life cycle emissions

The estimated CO_{2eq} emissions (GHG_i) for each of the seven cementitious material are reported in Figure 6.9 and compared to OPC. These present the 'worst case scenario', and so the actual CO_{2eq} emissions would likely be lower than those reported here. The carbon footprint of each component material is shown in Figure 6.9 (*right*): clinker (750 $kg_{CO_{2eq}}$ $tonne^{-1}$), CH (720 $kg_{CO_{2eq}}$ $tonne^{-1}$), SF (0.01 $kg_{CO_{2eq}}$ $tonne^{-1}$), NS (390 $kg_{CO_{2eq}}$ $tonne^{-1}$), MK (236 $kg_{CO_{2eq}}$ $tonne^{-1}$), NaOH 10 M (700 $kg_{CO_{2eq}}$ $tonne^{-1}$), NaOH 1 M (481 $kg_{CO_{2eq}}$ $tonne^{-1}$). The calculated values are similar to previously published estimates for geopolymer binders

Table 6.5: Minimum thickness of novel cement to achieve U-value ≤ 0.29 W m^{-2} K^{-1}, according to the Building Regulations 2013.

Sample	minimum thickness mm
CHI	30
CHI10	80
MK10	50
AMK	60
BMK	80
MKNS	20
CHNS	30

and concrete in different contexts [195, 22, 205, 208]. The results show that all types of novel cements studied here have lower embedded carbon compared to OPC. For example, sample MKNS has the lowest CO_{2eq} emissions associated with its manufacture, estimated to be half the emissions from OPC. Sample AMK, which has the highest embedded carbon among the novel cements, still has 20% lower CO_{2eq} than OPC. The selected raw materials, their world-wide availability coupled with minimum manufacturing make these novel binders environmentally competitive compared to traditional insulators (e.g. 1 tonne of extruded polystyrene is responsible for 1180 $kg_{CO_{2eq}}$) [192]. NaOH and CH are the most common ingredients of the alternative cements tested here, and the embedded carbon in these materials is similar to clinker (Figure 6.9 *right*). Thus, it is the relative proportion of low carbon materials such as SF, MK and NS which determine the overall carbon footprint for each cement. The major energy expended in the manufacture of NaOH occurs in the electrolysis process followed by cooling, which has a large electricity requirement. CH is produced by calcination of calcium carbonate followed by hydration. The CO_2 footprint of both materials could be reduced if they were produced using alternative source of energy for the electricity required (e.g. wind turbine, nuclear energy, photovoltaic energy for the manufacture of NaOH) or using bio-mass or other green fuel in the pyroprocessing of calcium carbonate.

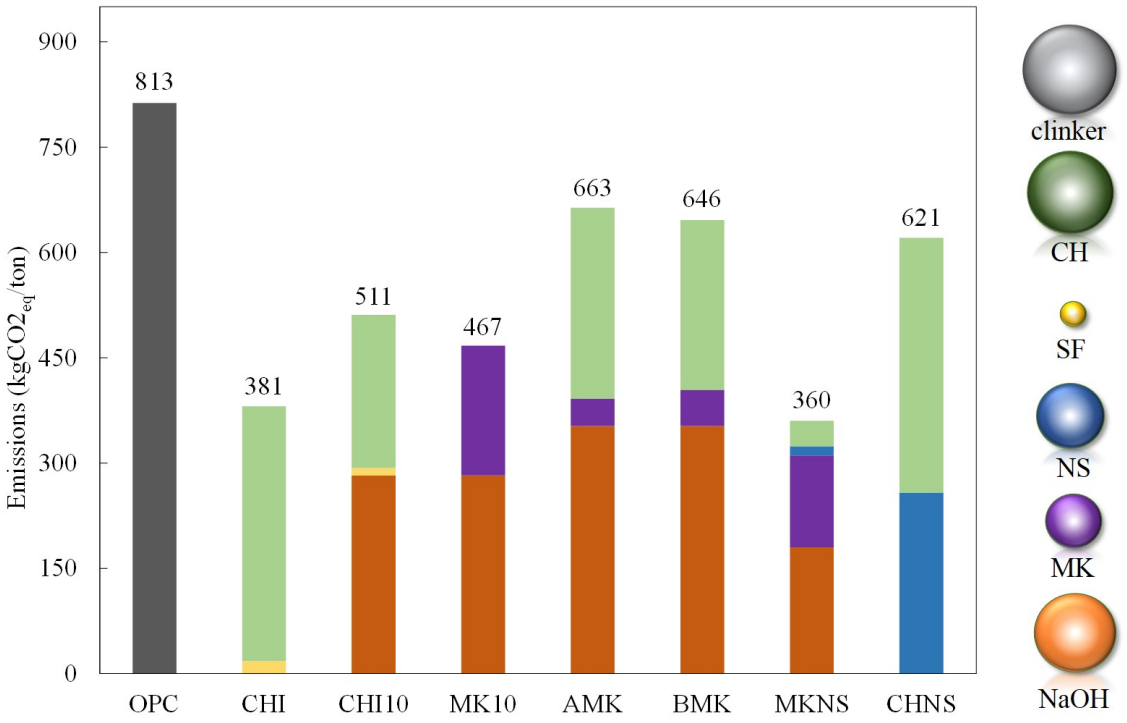

Figure 6.9: Total GHG emission and contribution of each raw material for all the mixes. *left*: Bubbles indicate the single component in each mix and the size indicates the GHG emission associated: clinker (750 $kg_{CO_{2eq}}$ $tonne^{-1}$), CH (720 $kg_{CO_{2eq}}$ $tonne^{-1}$), SF (0.01 $kg_{CO_{2eq}}$ $tonne^{-1}$), NS (390 $kg_{CO_{2eq}}$ $tonne^{-1}$), MK (236 $kg_{CO_{2eq}}$ $tonne^{-1}$), NaOH 10 M (700 $kg_{CO_{2eq}}$ $tonne^{-1}$), NaOH 1 M (481 $kg_{CO_{2eq}}$ $tonne^{-1}$), (not in scale).

6.3.5 Environmental impact

The low thermal conductivity of the novel cements also present an environmentally sustainable alternative for purposes such as wall cladding. Improving insulation in homes and buildings is an important aspect of reducing thermal energy loss and thus in turn reducing energy consumption. These innovative binders are also highly recyclable compared to conventional insulating components such as polymeric foams, polystyrene, polyurethane, rock-wool or vacuum insulation panels. With the exception of the samples with high alkali content, novel cements could be re-used in the building industry as construction and demolition waste (CDW), as intended by the European Waste Framework Directive 2008/98/EC and the EU Framework Programme for Research and Innovation Horizon 2020: '*incorporation up to ca. 80% of recycled CDW material to decrease the content of Portland cement used and consequently reduce the*

amount of waste to be placed in landfill'. These innovative cements are more environmentally friendly than OPC and other polymeric plastic insulators, and offer an environmental friendly alternative to traditional materials. They require less manufacturing and processing and the raw materials and reagents are readily available, which is important to consider for large-scale production.

Thus, although novel cements cannot replace OPC in all applications, they offer an environmentally sustainable alternative for several applications, and there is significant potential for these materials to contribute towards the decarbonisation of the cement industry.

6.4 Conclusions

In this study low-carbon cementitious materials have been developed and characterised. Metakaolin, silica fume, nano-silica and calcium hydroxide were combined at different ratios to produce 'green' binders for construction industry. Physical and mechanical properties were investigated. Compressive strength values (in the range 2–7 MPa) are typical of non-structural cements (mortars, rendering cements, etc.); density and porosity measurements show that these materials could be used in construction industry as functional building elements. Pozzolanic activity was detected by isothermal calorimetry and hydrated phases (calcium/aluminum silicate hydrate, faujasite, stratlingite) were found in XRD diffractograms. SEM images give an insight to the micro-structure, with the presence of semi-crystalline phases (C-S-H) and highly porous matrix, in agreement with the porosity measurements (0.48–0.74). Samples present thermal conductivity (0.05–0.26 W m^{-1} K^{-1}), in the range of conventional insulating materials. While previous studies have focused their attention on solely physical properties of OPC-free cements and geopolymers, here are brought together innovative materials able to satisfy thermal performance requirements within environmental standards. In facts, the addition of a 20 mm layer of sample MKNS to an external wall of existing housing, contributes to 10% decrease in thermal transmittance, as required by the Building Regulation 2013 in England and Wales. The environmental impact of the newly developed materials was assessed estimating the greenhouse gas emission associated to the manufacturing and production; all

the sample have a carbon footprint up to 23–55% lower than OPC. These materials are 'cleaner' than OPC and help to reduce CO_{2eq} emissions. The life cycle analysis presented here is simplistic, and more detailed life cycle and cost analyses should be the subject of future research to fully understand the economic impact of those materials in replacing OPC. However, the methodology adopted provides the basis for implementing a decision-making tool that can advise on, or scope in, low-carbon options before a more resource intensive life cycle assessment approach is applied. It will be therefore useful to construction companies or private developers intended to develop non-conventional building materials (e.g. geopolymers, alkali-activated cements), not yet regulated by law or international standards.

Chapter 7

Concluding remarks and outlook

7.1 Summary of key findings

One of the aims of this doctoral thesis was to study and characterise a mineral phase found in hydrated Portland cement, namely calcium silicate hydrate (C-S-H). Despite being the largest component in Portland cement and concrete, its properties are still researched. Recent developments in atomistic modelling and simulations have been proven effective in partially resolving C-S-H structure in its lattice parameters and atomic coordinates. However, laboratory experiments still face the challenges of reproducing synthetic C-S-H with similar characteristics to C-S-H formed by hydration of Portland cement (e.g. morphology, high C/S ratio). The importance of this mineral phase is also in its double-chained structure, which is being investigated for its ability to adsorb radionuclide and heavy metal ions.

Reported in *Chapter 2* is the synthesis and characterisation of solid synthetic C-S-H phase with a tobermorite-like structure, produced by simply mixing silica particles with water and $Ca(OH)_2$ powder. Solid-state characterisation of synthetic C-S-H using synchrotron XRD and PDF, showed that its structure is tailorable, and its d-spacing varied with the C/S ratio. A linear relationship was established to relate initial stoichiometry, with C/S ratio from 0.81 to 2.4 mol/mol, and final C/S ratio, respectively from 0.75 to 1.88 mol/mol. This is a useful tool to reproduce solid synthetic C-S-H with confidence using a simple, fast and comparatively low-cost synthesis process.

Once it was established that the C/S ratio is a key-parameter to 'tailor' C-S-H structure, the influence of silica particle size range on the C/S ratio was investigated, and results are summarised in *Chapter 3*. Synthetic C-S-H was produced from calcium hydroxide and a silica source, using either nano-silica (particle size 5–20 nm) or silica fume (particle size 100-1000 nm). Isothermal calorimetry, Raman spectrometry and thermal analysis showed that usage of nano-silica contributes to the formation of C-S-H with a higher C/S final ratio and lower excess of portlandite. This is due to the lower particle size of nano-silica and its higher specific surface area which makes nano-silica a high pozzolanic reactivity source of silica.

The environmental conditions under which C-S-H forms have been shown to influence the crystal growth and the final C/S ratio of hydrated C-S-H. In *Chapter 4* experiments on hydrothermal formation of C-S-H are reported. C-S-H was analysed using *in-situ* synchrotron XRD during continual hydrothermal formation from an initial slurry, over 3 hours at 110 °C. Results showed that temperature influences the C-S-H final C/S ratio and anisotropic behaviour in the crystallographic structure was observed. Furthermore, investigation on crystal growth rate revealed that an excess in initial calcium content (C/S ratio of 1.2 mol/mol) resulted in precipitation of portlandite that appeared to be incorporated in the C-S-H interlayer. This is further experimental evidence of the 'tailorability' of C-S-H structure.

C-S-H was experimentally investigated as a sealing agent for porosity reduction and micro-cracks closure. A non-destructive technique for low-pressure silica injections was developed and reported in *Chapter 5*. C-S-H was formed and precipitated inside cement pores by means of silica-injections; aqueous silica reacted with the calcium hydroxide naturally present in hydrate Portland cement to form additional C-S-H in the pore-volume. Results showed that a low-pressure (20 kPa) silica injection for 14 days with a 20 wt.% nano-silica suspension reduced the porosity by 30%, suggesting that this is a potential consolidant for friable or cracked concrete. Furthermore, the technique developed is non-destructive and does not require specific equipment, which is suitable for restoration of historical construction and nuclear waste containment ponds, in a localised section or large area.

Innovative OPC-free cementitious binders (including pure C-S-H paste) were developed and characterised mechanically and thermally, and described in *Chapter 6*. These novel binders

were compared with OPC cements in terms of thermal properties and their performance as insulation material. Measurement and calculationn of thermal properties showed that the application of an additional thin layer (20 mm) of OPC-free pastes reduces the thermal transmittance of an existing building wall by 10%. Furthermore, the greenhouse gas emissions (GHG) associated with their manufacture were calculated and compared to that of OPC; all the samples have a carbon footprint up to 23–55% lower than OPC. These materials are 'cleaner' than OPC and help to reduce CO_{2eq} emissions.

7.2 Future research

In conclusion, a summary of all the links to possible future work and applications of the findings described.

- The method described in *Chapter 2* for the synthesis of C-S-H with tobermorite-like structure has the potential to be scaled up for larger production. However further research needs to be conducted to address specific challenges in batch-production (e.g. ensure CO_2 environment, adequate cost analysis).
- The capability of C-S-H phase to physically adsorb pollutants, due to its high porosity, needs to be further investigated: water permeability and sorptivity test coupled with reactive transport modelling, would determine the potential of a relative low-cost solid C-S-H to be used in engineering application such as waste-water advanced treatment in filtration unit.
- Researchers have proven that OPC concrete has high γ-radiation shielding properties, suitable for use in the nuclear industry. The findings reported in this thesis have shown that C-S-H has a tailorable structure able to accommodate varying C/S ratios. Future investigation is needed to understand the interaction at the atomic scale between radionuclides (with different characteristics, e.g. anions or cations, ionic radius, etc.) and C-S-H phases, by means of high-resolution synchrotron XAFS, XPS and thermal analysis.
- To better understand the role of C/S ratio in the formation of C-S-H, different (non

standard) curing and/or environmental conditions should be investigated: varying CO_2, pH, temperature beyond tobermorite formation-crossover and pressure. Varying these parameters will contribute to expanding the experimental dataset available on C-S-H and build a solid basis for further modelling and simulations.

- The methodology for the calculation of GHG emissions of novel cementitious binders reported in chapter 6 needs be expanded to cover a full life cycle assessment and life cycle cost analysis. Both evaluations will build the basis to assess the recyclability potential of the developed OPC-free binders, contributing to a research aspects that has been overlooked in recent years.
- In order to evaluate the economical benefit from reduced energy consumption in heating, thermal flow modelling needs to be carried out to assess the insulating properties of novel cementitious binder in existing and new dwellings.

References

[1] D. P. Bentz and P. E. Stutzman, "Evolution of Porosity and calcium hydroxide in laboratory concretes containing silica fume," *Cement and Concrete Research*, vol. 24, no. 6, 1994.

[2] H. Du, S. Du, and X. Liu, "Durability performances of concrete with nano-silica," *Construction and Building Materials*, vol. 73, pp. 705–712, 2014.

[3] J.-Y. Shih, T.-P. Chang, and T.-C. Hsiao, "Effect of nanosilica on characterization of Portland cement composite," *Materials Science and Engineering: A*, vol. 424, no. 1-2, pp. 266–274, 2006.

[4] P.-k. Hou, S. Kawashima, K.-j. Wang, D. J. Corr, J.-s. Qian, and S. P. Shah, "Effects of colloidal nanosilica on rheological and mechanical properties of fly ash-cement mortar," *Cement and Concrete Composites*, vol. 35, no. 1, pp. 12–22, 2013.

[5] A. R. Jayapalan, B. Y. Lee, and K. E. Kurtis, "Can nanotechnology be 'green'? Comparing efficacy of nano and microparticles in cementitious materials," *Cement and Concrete Composites*, vol. 36, pp. 16–24, feb 2013.

[6] A. Neville, *Properties of Concrete*, 5th ed., Pitman, Ed., 1981.

[7] G. C. Bye, *Portland Cement - Composition, production and Properties*, 2nd ed., Pergamon, Ed. Insitute of Ceramics, 1983.

[8] H. Taylor, *Cement chemistry*, 2nd ed., T. Telford, Ed., 1998, vol. 20.

[9] E. M. Foley, J. J. Kim, and M. Reda Taha, "Synthesis and nano-mechanical characterization of calcium-silicate-hydrate (C-S-H) made with 1.5 CaO/SiO2 mixture," *Cement and Concrete Research*, vol. 42, no. 9, pp. 1225–1232, sep 2012.

[10] J. J. Kim, E. M. Foley, and M. M. Reda Taha, "Nano-mechanical characterization of synthetic calcium-silicate-hydrate (C-S-H) with varying CaO/SiO2 mixture ratios," *Cement and Concrete Composites*, vol. 36, pp. 65–70, feb 2013.

[11] S. Cordes and I. Odler, "Initial hydration of tricalcium silicate as studied by secondary neutrals mass spectrometry," *Cement and Concrete Research*, vol. 32, no. 7, pp. 1071–1075, jul 2002.

[12] K. Mori, T. Fukunaga, Y. Shiraishi, K. Iwase, Q. Xu, K. Oishi, K. Yatsuyanagi, M. Yonemura, K. Itoh, M. Sugiyama, T. Ishigaki, T. Kamiyama, and M. Kawai, "Structural and hydration properties of amorphous tricalcium silicate," *Cement and Concrete Research*, vol. 36, no. 11, pp. 2033–2038, nov 2006.

[13] L. Singh, S. Bhattacharyya, S. Shah, G. Mishra, S. Ahalawat, and U. Sharma, "Studies on early stage hydration of tricalcium silicate incorporating silica nanoparticles: Part I," *Construction and Building Materials*, vol. 74, pp. 278–286, jan 2015.

[14] M. Moukwa, S. Farrington, and D. Youn, "Determination of Ca(OH)2 in hydrated cement paste by differential scanning calorimetry," *Thermochimica Acta*, vol. 195, pp. 231–237, jan 1992.

[15] F. Brunet, T. Charpentier, C. Chao, H. Peycelon, and A. Nonat, "Characterization by solid-state NMR and selective dissolution techniques of anhydrous and hydrated CEM V cement pastes," *Cement and Concrete Research*, vol. 40, no. 2, pp. 208–219, 2010.

[16] S. Dittrich, J. Neubauer, and F. Goetz-Neunhoeffer, "The influence of fly ash on the hydration of OPC within the first 44h- A quantitative in situ XRD and heat flow calorimetry study," *Cement and Concrete Research*, vol. 56, pp. 129–138, 2014.

[17] A. Chaipanich, T. Nochaiya, W. Wongkeo, and P. Torkittikul, "Compressive strength and microstructure of carbon nanotubes-fly ash cement composites," *Materials Science and Engineering: A*, vol. 527, no. 4-5, pp. 1063–1067, feb 2010.

[18] T. Nochaiya and A. Chaipanich, "Behavior of multi-walled carbon nanotubes on the porosity and microstructure of cement-based materials," *Applied Surface Science*, vol. 257, no. 6, pp. 1941–1945, jan 2011.

[19] M. Berra, F. Carassiti, T. Mangialardi, A. Paolini, and M. Sebastiani, "Effects of nanosilica addition on workability and compressive strength of Portland cement pastes," *Construction and Building Materials*, vol. 35, pp. 666–675, oct 2012.

[20] M. Heikal, A. Ali, M. Ismail, and S. A. N. Ibrahim, "Behavior of composite cement pastes containing silica nano-particles at elevated temperature," *Construction and Building Materials*, vol. 70, pp. 339–350, nov 2014.

[21] L. Valentini, M. Favero, M. C. Dalconi, V. Russo, G. Ferrari, and G. Artioli, "Kinetic Model of Calcium-Silicate Hydrate Nucleation and Growth in the Presence of PCE Superplasticizers," *Crystal Growth and Design*, vol. 16, no. 2, pp. 646–654, 2016.

[22] L. K. Turner and F. G. Collins, "Carbon dioxide equivalent (CO2-e) emissions: A comparison between geopolymer and OPC cement concrete," *Construction and Building Materials*, vol. 43, pp. 125–130, jun 2013.

[23] K. Sobolev and M. F. Gutiérrez, "How nanotechnology can change the concrete world," *American Ceramic Society Bulletin*, vol. 84, no. October, pp. 14–18, 2005.

[24] F. Sanchez and K. Sobolev, "Nanotechnology in concrete - A review," *Construction and Building Materials*, vol. 24, no. 11, pp. 2060–2071, 2010.

[25] J. Lee, S. Mahendra, and P. J. J. Alvarez, "Nanomaterials in the Construction Industry: A Review of Their Applications," *ACS nano*, vol. 4, no. 7, pp. 3580–3590, 2010.

[26] C. Ouellet-Plamondon and G. Habert, *Handbook of Alkali-Activated Cements, Mortars and Concretes*. Elsevier, 2015.

[27] L. Raki, J. Beaudoin, R. Alizadeh, J. Makar, and T. Sato, "Cement and Concrete Nanoscience and Nanotechnology," *Materials*, vol. 3, pp. 918–942, 2010.

[28] J. L. Provis, I. Ismail, R. J. Myers, V. Rose, and J. S. J. V. Deventer, "Characterising the structure and permeability of alkali-activated binders," *International RILEM Conference on Advances in Construction Materials Through Science and Engineering*, no. July 2016, pp. 493–501, 2011.

[29] M. A. Villaquirán-Caicedo, R. M. de Gutiérrez, S. Sulekar, C. Davis, and J. C. Nino, "Thermal properties of novel binary geopolymers based on metakaolin and alternative silica sources," *Applied Clay Science*, vol. 118, pp. 276–282, 2015.

[30] L. Singh, S. Karade, S. Bhattacharyya, M. Yousuf, and S. Ahalawat, "Beneficial role of nanosilica in cement based materials âĂŞ A review," *Construction and Building Materials*, vol. 47, pp. 1069–1077, oct 2013.

[31] Y. Liu and X. Shi, "Ionic transport in cementitious materials under an externally applied electric field: Finite element modeling," *Construction and Building Materials*, vol. 27, no. 1, pp. 450–460, aug 2011.

[32] H. Huang and G. Ye, "Application of sodium silicate solution as self-healing agent in cementitious materials," *International RILEM Conference on Advances in Construction Materials Through Science and Engineering*, pp. 530 – 536, 2011.

[33] W. De Muynck, K. Cox, N. D. Belie, and W. Verstraete, "Bacterial carbonate precipitation as an alternative surface treatment for concrete," *Construction and Building Materials*, vol. 22, pp. 875–885, 2008.

[34] R. Siddique and N. K. Chahal, "Effect of ureolytic bacteria on concrete properties," *Construction and Building Materials*, vol. 25, no. 10, pp. 3791–3801, 2011.

[35] R. Pei, J. Liu, S. Wang, and M. Yang, "Use of bacterial cell walls to improve the mechanical performance of concrete," *Cement and Concrete Composites*, vol. 39, pp. 122–130, 2013.

[36] H. E. Cardenas and L. J. Struble, "Modeling Electrokinetic Nanoparticle Penetration for Permeability Reduction of Hardened Cement Paste," *Journal of Materials in Civil Engineering*, vol. 20, no. 11, pp. 683–691, 2008.

[37] Z. Zhang, J. L. Provis, A. Reid, and H. Wang, "Geopolymer foam concrete: An emerging material for sustainable construction," *Construction and Building Materials*, vol. 56, pp. 113–127, apr 2014.

[38] J. J. Chen, J. J. Thomas, H. F. Taylor, and H. M. Jennings, "Solubility and structure of calcium silicate hydrate," *Cement and Concrete Research*, vol. 34, no. 9, pp. 1499–1519, sep 2004.

[39] A. Stumm, K. Garbev, G. Beuchle, L. Black, P. Stemmermann, and R. Nüesch, "Incorporation of zinc into calcium silicate hydrates, Part I: formation of C-S-H(I) with C/S=2/3 and its isochemical counterpart gyrolite," *Cement and Concrete Research*, vol. 35, no. 9, pp. 1665–1675, 2005.

[40] E. Wieland, J. Tits, D. Kunz, and R. Dähn, "Strontium Uptake by Cementitious Materials," *Environmental Science & Technology*, vol. 42, no. 2, pp. 403–409, jan 2008.

[41] Y. Zhou, D. Hou, J. Jiang, and P. Wang, "Chloride ions transport and adsorption in the nano-pores of silicate calcium hydrate: Experimental and molecular dynamics studies," *Construction and Building Materials*, vol. 126, pp. 991–1001, 2016.

[42] X. Cong and R. Kirkpatrick, "29Si MAS NMR study of the structure of calcium silicate hydrate," *Advanced Cement Based Materials*, vol. 3, no. 3-4, pp. 144–156, 1996.

[43] A. Harris, M. Manning, W. Tearle, and C. Tweed, "Testing of models of the dissolution of cements-leaching of synthetic CSH gels," *Cement and Concrete Research*, vol. 32, no. 5, pp. 731–746, 2002.

[44] K. Garbev, M. Bornefeld, G. Beuchle, and P. Stemmermann, "Cell dimensions and composition of nanocrystalline calcium silicate hydrate solid solutions. Part 1: Synchotron-based X-Ray Diffraction," *Journal of the American Ceramic Society*, vol. 91, no. 9, pp. 3005–3014, 2008.

[45] X. Pardal, I. Pochard, and A. Nonat, "Experimental study of Si-Al substitution in calcium-silicate-hydrate (C-S-H) prepared under equilibrium conditions," *Cement and Concrete Research*, vol. 39, no. 8, pp. 637–643, aug 2009.

[46] S. Tränkle, D. Jahn, T. Neumann, L. Nicoleau, N. Hüsing, and D. Volkmer, "Conventional and microwave assisted hydrothermal syntheses of 11 Å tobermorite," *Journal of Materials Chemistry A*, vol. 1, no. 35, p. 10318, aug 2013.

[47] A. Kumar, B. J. Walder, A. Kunhi Mohamed, A. Hofstetter, B. Srinivasan, A. J. Rossini, K. Scrivener, L. Emsley, and P. Bowen, "The Atomic-Level Structure of Cementitious Calcium Silicate Hydrate," *Journal of Physical Chemistry C*, vol. 121, no. 32, pp. 17 188–17 196, 2017.

[48] W. Kunther, S. Ferreiro, and J. Skibsted, "Influence of the Ca/Si Ratio on the Compressive Strength of Cementitious Calcium-Silicate-Hydrate Binders," *J. Mater. Chem. A*, vol. 5, pp. 17 401–17 412, 2017.

[49] O. Mendoza, C. Giraldo, S. S. Camargo, and J. I. Tobón, "Structural and nano-mechanical properties of Calcium Silicate Hydrate (C-S-H) formed from alite hydration in the presence of sodium and potassium hydroxide," *Cement and Concrete Research*, vol. 74, pp. 88–94, aug 2015.

[50] S. Nath, S. Maitra, S. Mukherjee, and S. Kumar, "Microstructural and morphological evolution of fly ash based geopolymers," *Construction and Building Materials*, vol. 111, pp. 758–765, 2016.

[51] A. Hamilton and C. Hall, "Physicochemical Characterization of a Hydrated Calcium Silicate Board Material," *Journal of Building Physics*, vol. 29, no. 1, pp. 9–19, 2005.

[52] J. Filik, A. Ashton, P. Chang, P. Chater, S. Day, M. Drakopoulos, M. Gerring, M. Hart, O. Magdysyuk, and S. Michalik, "Processing two-dimensional X-ray diffraction and small-angle scattering data in DAWN 2," *Journal of Applied Crystallography 2*, vol. 50, pp. 959–966, 2017.

[53] P. J. Chupas, X. Qiu, J. C. Hanson, P. L. Lee, C. P. Grey, and S. J. L. Billinge, "Rapid-acquisition pair distribution function (RA-PDF) analysis," *Journal of Applied Crystallography*, vol. 36, no. 6, pp. 1342–1347, 2003.

[54] K. Garbev, M. Bornefeld, G. Beuchle, and P. Stemmermann, "Cell Dimensions and Composition of Nanocrystalline Calcium Silicate Hydrate Solid Solutions. Part 2: X-Ray and Thermogravimetry Study," *Journal of the American Ceramic Society*, vol. 91, no. 9, pp. 3015–3023, sep 2008.

[55] D. Sugiyama, "Chemical alteration of calcium silicate hydrate (C-S-H) in sodium chloride solution," *Cement and Concrete Research*, vol. 38, no. 11, pp. 1270–1275, nov 2008.

[56] S. Grangeon, F. Claret, C. Lerouge, F. Warmont, T. Sato, S. Anraku, C. Numako, Y. Linard, and B. Lanson, "On the nature of structural disorder in calcium silicate hydrates with a calcium/silicon ratio similar to tobermorite," *Cement and Concrete Research*, vol. 52, pp. 31–37, oct 2013. [Online]. Available: http://www.sciencedirect.com/science/article/pii/S0008884613001208

[57] E. Bonaccorsi, S. Merlino, and A. R. Kampf, "The Crystal Structure of Tobermorite 14 Å (Plombierite), a C-S-H Phase," *Journal of the American Ceramic Society*, vol. 88, no. 3, pp. 505–512, mar 2005.

[58] S. Merlino, E. Bonaccorsi, and T. Armbruster, "The real structure of tobermorite 11 Å: normal and anomalous forms, OD character and polytypic modifications," *European Journal of Mineralogy*, vol. 13, no. 3, pp. 577–590, may 2001.

[59] S. Soyer-Uzun, S. R. Chae, C. J. Benmore, H. R. Wenk, and P. J. M. Monteiro, "Compositional evolution of calcium silicate hydrate (C-S-H) structures by total X-ray scattering," *Journal of the American Ceramic Society*, vol. 95, no. 2, pp. 793–798, 2012.

[60] S. Grangeon, A. Fernandez-Martinez, A. Baronnet, N. Marty, A. Poulain, E. Elkaim, C. Roosz, S. Gaboreau, P. Henocq, and F. Claret, "Quantitative X-ray pair distribution function analysis of nanocrystalline calcium silicate hydrates: a contribution to the understanding of cement chemistry," *Journal of Applied Crystallography*, vol. 50, no. 22, pp. 14–21, 2017.

[61] I. Richardson, L. Black, J. Skibsted, and R. Kirkpatrick, "Characterisation of cement hydrate phases by TEM, NMR and Raman spectroscopy," *Advances in Cement Research*, vol. 22, no. 4, pp. 233–248, 2010.

[62] T. F. Sevelsted and J. Skibsted, "Carbonation of C-S-H and C-A-S-H samples studied by 13C, 27Al and 29Si MAS NMR spectroscopy," *Cement and Concrete Research*, vol. 71, pp. 56–65, 2015.

[63] I. G. Richardson, "Model structures for C-(A)-S-H(I)," *Acta Crystallographica Section B: Structural Science, Crystal Engineering and Materials*, vol. 70, no. 6, pp. 903–923, 2014.

[64] E. L'Hôpital, B. Lothenbach, D. Kulik, and K. Scrivener, "Influence of calcium to silica ratio on aluminium uptake in calcium silicate hydrate," *Cement and Concrete Research*, vol. 85, pp. 111–121, 2016.

[65] A. Morandeau, M. Thiéry, and P. Dangla, "Investigation of the carbonation mechanism of CH and C-S-H in terms of kinetics, microstructure changes and moisture properties," *Cement and Concrete Research*, vol. 56, pp. 153–170, 2014.

[66] E. Tajuelo, K. Garbev, D. Merz, L. Black, and I. G. Richardson, "Thermal stability of C-S-H phases and applicability of Richardson and Groves' and Richardson C-(A)-S-H (I) models to synthetic C-S-H," *Cement and Concrete Research*, vol. 93, pp. 45–56, 2017.

[67] M. Chen, L. Lu, S. Wang, P. Zhao, W. Zhang, and S. Zhang, "Investigation on the formation of tobermorite in calcium silicate board and its influence factors under autoclaved curing," *Construction and Building Materials*, vol. 143, pp. 280–288, 2017.

[68] S. Ma, W. Li, S. Zhang, Y. Hu, and X. Shen, "Study on the hydration and microstructure of Portland cement containing diethanol-isopropanolamine," *Cement and Concrete Research*, vol. 67, pp. 122–130, jan 2015.

[69] F. Saito, G. Mi, and M. Hanada, "Mechanochemical synthesis of hydrated calcium silicates by room temperature grinding," *Solid State Ionics*, vol. 101, pp. 37–43, 1997.

[70] W. Sha and G. Pereira, "Differential scanning calorimetry study of ordinary Portland cement paste containing metakaolin and theoretical approach of metakaolin activity," *Cement and Concrete Composites*, vol. 23, no. 6, pp. 455–461, 2001.

[71] J. Escalante-Garcia, G. Mendoza, and J. Sharp, "Indirect determination of the Ca/Si ratio of the C-S-H gel in Portland cements," *Cement and Concrete Research*, vol. 29, no. 12, pp. 1999–2003, dec 1999.

[72] J. J. Thomas, J. J. Chen, H. M. Jennings, and D. a. Neumann, "Ca-OH bonding in the C-S-H gel phase of tricalcium silicate and white portland cement pastes measured by inelastic neutron scattering," *Chemistry of Materials*, vol. 15, no. 20, pp. 3813–3817, 2003.

[73] E. Tajuelo Rodriguez, I. G. Richardson, L. Black, E. Boehm-Courjault, A. Nonat, and J. Skibsted, "Composition, silicate anion structure and morphology of calcium silicate hydrates (C-S-H) synthesised by silica-lime reaction and by controlled hydration of tricalcium silicate (C3S)," *Advances in Applied Ceramics*, vol. 114, no. 7, pp. 362–371, oct 2015.

[74] I. Ioannou, A. Hamilton, and C. Hall, "Capillary absorption of water and n-decane by autoclaved aerated concrete," *Cement and Concrete Research*, vol. 38, no. 6, pp. 766–771, 2008.

[75] I. Richardson, "Tobermorite/jennite- and tobermorite/calcium hydroxide-based models for the structure of C-S-H: applicability to hardened pastes of tricalcium silicate, β-dicalcium silicate, Portland cement, and blends of Portland cement with blast-furnace slag, metakaol," *Cement and Concrete Research*, vol. 34, no. 9, pp. 1733–1777, sep 2004. [Online]. Available: http://www.sciencedirect.com/science/article/pii/S0008884604002364

[76] Y. Qing, Z. Zenan, K. Deyu, and C. Rongshen, "Influence of nano-SiO2 addition on properties of hardened cement paste as compared with silica fume," *Construction and Building Materials*, vol. 21, no. 3, pp. 539–545, mar 2007.

[77] G. Quercia, G. Hüsken, and H. J. H. Brouwers, "Water demand of amorphous nano silica and its impact on the workability of cement paste," *Cement and Concrete Research*, vol. 42, no. 2, pp. 344–357, 2012.

[78] H. Biricik and N. Sarier, "Comparative study of the characteristics of nano silica-, silica fume- and fly ash-incorporated cement mortars," *Materials Research*, vol. 17, no. 3, pp. 570–582, 2014.

[79] R. Yu, P. Spiesz, and H. Brouwers, "Effect of nano-silica on the hydration and microstructure development of Ultra-High Performance Concrete (UHPC) with a low binder amount," *Construction and Building Materials*, vol. 65, pp. 140–150, 2014.

[80] A. Kar, I. Ray, A. Unnikrishnan, and J. F. Davalos, "Estimation of C-S-H and calcium hydroxide for cement pastes containing slag and silica fume," *Construction and Building Materials*, vol. 30, pp. 505–515, 2012.

[81] A. Lazaro, G. Quercia, H. J. H. Brouwers, and J. W. Geus, "Synthesis of a Green Nano-Silica Material Using Beneficiated Waste Dunites and Its Application in Concrete," *World Journal of Nano Science and Engineering*, vol. 03, no. 03, pp. 41–51, 2013.

[82] Y. Xu and D. Chung, "Cement of high specific heat and high thermal conductivity, obtained by using silane and silica fume as admixtures," *Cement and Concrete Research*, vol. 30, no. 7, pp. 1175–1178, jul 2000.

[83] H.-W. Song, S.-W. Pack, S.-H. Nam, J.-C. Jang, and V. Saraswathy, "Estimation of the permeability of silica fume cement concrete," *Construction and Building Materials*, vol. 24, no. 3, pp. 315–321, mar 2010.

[84] Y. Wei, W. Yao, X. Xing, and M. Wu, "Quantitative evaluation of hydrated cement modified by silica fume using QXRD, 27Al MAS NMR, TG-DSC and selective dissolution techniques," *Construction and Building Materials*, vol. 36, pp. 925–932, 2012.

[85] G. Land and D. Stephan, "The influence of nano-silica on the hydration of ordinary Portland cement," *Journal of Materials Science*, vol. 47, no. 2, pp. 1011–1017, 2012.

[86] L. Wang, D. Zheng, S. Zhang, H. Cui, and D. Li, "Effect of Nano-SiO2 on the Hydration and Microstructure of Portland Cement," *Nanomaterials*, vol. 6, no. 12, p. 241, 2016.

[87] M. Kumar, S. K. Singh, and N. Singh, "Heat evolution during the hydration of Portland cement in the presence of fly ash, calcium hydroxide and super plasticizer," *Thermochimica Acta*, vol. 548, pp. 27–32, nov 2012.

[88] B. W. Langan, K. Weng, and M. A. Ward, "Effect of silica fume and fly ash on heat of hydration of Portland cement," *Cement and Concrete Research*, vol. 32, no. 7, pp. 1045–1051, 2002.

[89] M. Oltulu and R. Åđahin, "Pore structure analysis of hardened cement mortars containing silica fume and different nano-powders," *Construction and Building Materials*, vol. 53, pp. 658–664, feb 2014.

[90] J. J. Thomas, J. J. Biernacki, J. W. Bullard, S. Bishnoi, J. S. Dolado, G. W. Scherer, and A. Luttge, "Modeling and simulation of cement hydration kinetics and microstructure development," *Cement and Concrete Research*, vol. 41, no. 12, pp. 1257–1278, dec 2011.

[91] Q. Zeng, K. Li, T. Fen-chong, and P. Dangla, "Determination of cement hydration and pozzolanic reaction extents for fly-ash cement pastes," *Construction and Building Materials*, vol. 27, no. 1, pp. 560–569, feb 2012.

[92] J. Zhang and G. W. Scherer, "Comparison of methods for arresting hydration of cement," *Cement and Concrete Research*, vol. 41, no. 10, pp. 1024–1036, oct 2011.

[93] R. Maddalena and A. Hamilton, "Low-pressure silica injection for porosity reduction in cementitious materials," *Construction and Building Materials*, vol. 134, pp. 610–616, 2017.

[94] L. Black, C. Breen, J. Yarwood, K. Garbev, P. Stemmermann, and B. Gasharova, "Structural Features of C-S-H(I) and its Carbonation in Air: A Raman Spectroscopic Study. Part II: Carbonated Phases," *Journal of the American Ceramic Society*, vol. 90, no. 3, pp. 908–917, mar 2007.

[95] K. Garbev, P. Stemmermann, L. Black, C. Breen, J. Yarwood, and B. Gasharova, "Structural Features of C-S-H(I) and its Carbonation in Air: A Raman Spectroscopic Study. Part I: Fresh Phases," *Journal of the American Ceramic Society*, vol. 90, no. 3, pp. 900–907, mar 2007.

[96] R. J. Kirkpatrick, J. L. Yarger, P. F. McMillan, Y. Ping, and X. Cong, "Raman spectroscopy of C-S-H, tobermorite, and jennite," *Advanced Cement Based Materials*, vol. 5, no. 3-4, pp. 93–99, apr 1997.

[97] S. Potgieter-Vermaak, J. Potgieter, M. Belleil, F. DeWeerdt, and R. Van Grieken, "The application of Raman spectrometry to the investigation of cement," *Cement and Concrete Research*, vol. 36, no. 4, pp. 663–670, apr 2006.

[98] V. Tydlitát, J. Zákoutský, M. Schmieder, and R. Černý, "Application of large-volume calorimetry for monitoring the early-stage hydration heat development in cement-based composites as a function of w/c," *Thermochimica Acta*, vol. 546, pp. 44–48, 2012.

[99] V. Tydlitát, J. Zákoutský, and R. Černý, "Early-stage hydration heat development in blended cements containing natural zeolite studied by isothermal calorimetry," *Thermochimica Acta*, vol. 582, pp. 53–58, apr 2014.

[100] F. Bellmann, J. Leppert, M. Görlach, M. Krbetschek, D. Damidot, and H.-M. Ludwig, "Analysis of disorder in tricalcium silicate by 29Si NMR spectroscopy and additional methods," *Cement and Concrete Research*, vol. 57, pp. 105–116, 2014.

[101] M. Avrami, "Kinetics of Phase Change," *Journal of Chemical Physics*, vol. 7, pp. 1103–1112, 1939.

[102] W. Johnson and R. Mehl, "Reaction kinetics in processes of nucleation and growth," *Trans. Am. Inst. Min. Metall. Eng.*, vol. 135, p. 416, 1936.

[103] A. Kolmogorov, "A statistical theory for the recrystallization of metals," *Bull. Acad. Sci. USSR Phys.*, vol. 1, p. 255, 1937.

[104] J. Cahn, "The kinetics of grain boundary nucleated reactions," *Acta Metall.*, vol. 4, pp. 449–459, 1956.

[105] H. M. Jennings and S. Johnson, "Simulation of microstructure development during the hydration of a cement compound," *Journal of American Ceramic Society1*, vol. 69, pp. 790–795, 986.

[106] K. Van Breugel, "Numerical simulation of hydration and microstructural development in hardening cement paste (I): theory," *Cement and Concrete Research*, vol. 25, pp. 319–331, 1995.

[107] E. Garboczi and D. Bentz, "Computer simulation of the diffusivity of cement-based materials," *Journal of Materials Science1*, vol. 27, no. 8, pp. 2083–2092, 1992.

[108] J. W. Bullard, "A three-dimensional microstructural model of reactions and transport in aqueous mineral systems," *Modelling Simul. Mater. Sci. Eng.*, vol. 15, pp. 711–738, 2007.

[109] S. Bishnoi and K. L. Scrivener, "μic: a new platform for modelling the hydration of cements," *Cement and Concrete Research2*, vol. 39, pp. 266–274, 2009.

[110] J. J. Thomas, "A new approach to modeling the nucleation and growth kinetics of tricalcium silicate hydration," *Journal of the American Ceramic Society*, vol. 90, no. 10, pp. 3282–3288, 2007.

[111] G. Baert, N. De Belie, and G. De Schutter, "Multicompound Model for the Hydration of Portland Cement-Fly Ash Binders," *Journal of Materials in Civil Engineering*, vol. 23, no. 6, pp. 761–766, 2011.

[112] D. Ravikumar and N. Neithalath, "Reaction kinetics in sodium silicate powder and liquid activated slag binders evaluated using isothermal calorimetry," *Thermochimica Acta*, vol. 546, pp. 32–43, 2012.

[113] D. S. Klimesch, A. Ray, and J.-P. Guerbois, "Differential scanning calorimetry evaluation of autoclaved cement based building materials made with construction and demolition waste," *Thermochimica Acta*, vol. 389, no. 1-2, pp. 195–198, jul 2002.

[114] S. Kawashima, P. Hou, D. J. Corr, and S. P. Shah, "Modification of cement-based materials with nanoparticles," *Cement and Concrete Composites*, vol. 36, pp. 8–15, feb 2013.

[115] S. Bae, C. Meral, J.-e. Oh, J. Moon, M. Kunz, and P. J. Monteiro, "Characterization of morphology and hydration products of high-volume fly ash paste by monochromatic scanning x-ray micro-diffraction (μ-SXRD)," *Cement and Concrete Research*, vol. 59, pp. 155–164, may 2014.

[116] L. P. Singh, S. K. Bhattacharyya, S. P. Shah, G. Mishra, and U. Sharma, "Studies on early stage hydration of tricalcium silicate incorporating silica nanoparticles : Part II," *Construction and Building Materials*, vol. 102, pp. 943–949, 2016.

[117] Z. Jing, F. Jin, N. Yamasaki, and E. H. Ishida, "Hydrothermal synthesis of a novel tobermorite-based porous material from municipal incineration bottom ash," *Industrial and Engineering Chemistry Research*, vol. 46, no. 8, pp. 2657–2660, 2007.

[118] W. Guan, F. Ji, Z. Fang, D. Fang, Y. Cheng, P. Yan, and Q. Chen, "Low hydrothermal temperature synthesis of porous calcium silicate hydrate with enhanced reactivity SiO2," *Ceramics International*, vol. 40, no. 3, pp. 4415–4420, 2014.

[119] Q. Y. Chen, M. Tyrer, C. D. Hills, X. M. Yang, and P. Carey, "Immobilisation of heavy metal in cement-based solidification/stabilisation: a review." *Waste management (New York, N.Y.)*, vol. 29, no. 1, pp. 390–403, jan 2009.

[120] P. P. Falciglia and F. G. A. Vagliasindi, "Stabilisation/Solidification of Pb Polluted Soils: Influence of Contamination Level and Soil:Binder Ratio on the Properties of Cement-Fly Ash Treated Soils," *Chemical Engineering Transactions*, vol. 32, pp. 385–390, 2013.

[121] P. P. Falciglia, A. Al-Tabbaa, and F. G. a. Vagliasindi, "Development of a performance threshold approach for identifying the management options for stabilisation/solidification of lead polluted soils," *Journal of Environmental Engineering and Landscape Management*, vol. 22, no. 2, pp. 85–95, 2014.

[122] P. P. Falciglia, V. Puccio, S. Romano, and F. G. A. Vagliasindi, "Performance study and influence of radiation emission energy and soil contamination level on γ-radiation shielding of stabilised/solidified radionuclide-polluted soils," *Journal of Environmental Radioactivity*, vol. 143, pp. 20–28, 2015.

[123] B. Guo, B. Liu, J. Yang, and S. Zhang, "The mechanisms of heavy metal immobilization by cementitious material treatments and thermal treatments: A review," *Journal of Environmental Management*, vol. 193, pp. 410–422, 2017.

[124] J.-K. Kim, Y.-H. Moon, and S.-H. Eo, "Compressive Strength Development of Concrete With," *Cement and Concrete Research*, vol. 28, no. 12, pp. 1761–1773, 1998.

[125] E. Gallucci, X. Zhang, and K. Scrivener, "Effect of temperature on the microstructure of calcium silicate hydrate (C-S-H)," *Cement and Concrete Research*, vol. 53, pp. 185–195, nov 2013.

[126] S. Bahafid, S. Ghabezloo, M. Duc, P. Faure, and J. Sulem, "Effect of the hydration temperature on the microstructure of Class G cement: C-S-H composition and density," *Cement and Concrete Research*, vol. 95, pp. 270–281, 2017.

[127] C. Ferry, C. Poinssot, C. Cappelaere, L. Desgranges, C. Jegou, F. Miserque, J. P. Piron, D. Roudil, and J. M. Gras, "Specific outcomes of the research on the spent fuel long-term evolution in interim dry storage and deep geological disposal," *Journal of Nuclear Materials*, vol. 352, no. 1-3, pp. 246–253, 2006.

[128] S. Shaw, S. Clark, and C. Henderson, "Hydrothermal formation of the calcium silicate hydrates, tobermorite (Ca5Si6O16(OH)2·4H2O) and xonotlite (Ca6Si6O17(OH)2): an in situ synchrotron study," *Chemical Geology*, vol. 167, no. 1-2, pp. 129–140, jun 2000.

[129] K. Yanagisawa, X. Hu, A. Onda, and K. Kajiyoshi, "Hydration of β-dicalcium silicate at high temperatures under hydrothermal conditions," *Cement and Concrete Research*, vol. 36, no. 5, pp. 810–816, 2006.

[130] G. O. Assarsson and E. Rydberg, "Hydrothermal Reactions between Calcium Hydroxide and Amorphous Silica," *The Journal of Physical Chemistry*, vol. 60, no. 4, pp. 397–404, 1956.

[131] Y. Okada, H. Ishida, and T. Mitsuda, "29Si NMR spectroscopy of silicate anions in hydrothermally formed C-S-H," *Journal of American Ceramic Society1*, vol. 77, pp. 765–768, 1994.

[132] A. Hartmann, M. Khakhutov, and J.-C. Buhl, "Hydrothermal synthesis of CSH-phases (tobermorite) under influence of Ca-formate," *Materials Research Bulletin*, vol. 51, pp. 389–396, mar 2014.

[133] J. Kikuma, M. Tsunashima, T. Ishikawa, S. Matsuno, A. Ogawa, K. Matsui, and M. Sato, "Effects of quartz particle size and water-to-solid ratio on hydrothermal synthesis of tobermorite studied by in-situ time-resolved X-ray diffraction," *Journal of Solid State Chemistry*, vol. 184, no. 8, pp. 2066–2074, 2011.

[134] J. Kikuma, M. Tsunashima, T. Ishikawa, S. Y. Matsuno, A. Ogawa, K. Matsui, and M. Sato, "In situ time-resolved X-ray diffraction of tobermorite formation process under autoclave condition," *Journal of the American Ceramic Society*, vol. 93, no. 9, pp. 2667–2674, 2010.

[135] K. Matsui, J. Kikuma, M. Tsunashima, T. Ishikawa, S. Y. Matsuno, A. Ogawa, and M. Sato, "In situ time-resolved X-ray diffraction of tobermorite formation in autoclaved aerated concrete: Influence of silica source reactivity and Al addition," *Cement and Concrete Research*, vol. 41, no. 5, pp. 510–519, 2011.

[136] J. Jiang, C. Cui, J. Liu, and W. Liao, "Hydrothermal synthesis of xonotlite-type calcium silicate insulation material using industrial zirconium waste residue," *Journal Wuhan University of Technology, Materials Science Edition*, vol. 26, no. 3, pp. 519–522, 2011.

[137] M. Hart, M. Drakopoulos, C. Reinhard, and T. Connolley, "Complete Elliptical Ring Geometry Provides Energy and Instrument Calibration for Synchrotron-Based Two-Dimensional X-Ray Diffraction," *Journal of Applied Crystallography*, vol. 46, pp. 1249–1260, 2013.

[138] L. Desgranges, D. Grebille, G. Calvarin, G. Chevrier, N. Floquet, and J. C. Niepce, "Hydrogen thermal motion in calcium hydroxide: Ca(OH)2," *Acta Crystallographica Section B*, vol. 49, no. 5, pp. 812–817, 1993.

[139] F. Battocchio, P. J. M. Monteiro, and H. R. Wenk, "Rietveld refinement of the structures of 1.0 C-S-H and 1.5 C-S-H," *Cement and Concrete Research*, vol. 42, no. 11, pp. 1534–1548, 2012.

[140] S. Grangeon, F. Claret, C. Roosz, T. Sato, S. Gaboreau, and Y. Linard, "Structure of nanocrystalline calcium silicate hydrates: Insights from X-ray diffraction, synchrotron X-ray absorption and nuclear magnetic resonance," *Journal of Applied Crystallography*, vol. 49, pp. 771–783, 2016.

[141] H. Xu, Y. Zhao, S. C. Vogel, L. L. Daemen, and D. D. Hickmott, "Anisotropic thermal expansion and hydrogen bonding behavior of portlandite: A high-temperature neutron diffraction study," *Journal of Solid State Chemistry*, vol. 180, no. 4, pp. 1519–1525, 2007.

[142] A. Le Bail, "Monte Carlo indexing with McMaille," *Powder Diffraction*, vol. 19, no. 03, pp. 249–254, 2004.

[143] H. Fukui, O. Ohtaka, T. Fujisawa, T. Kunisada, T. Suzuki, and T. Kikegawa, "Thermo-elastic property of Ca(OH)2 portlandite," *High Pressure Research*, vol. 23, no. 1-2, pp. 55–61, 2003.

[144] H. Manzano, J. S. Dolado, and A. Ayuela, "Elastic properties of the main species present in Portland cement pastes," *Acta Materialia*, vol. 57, no. 5, pp. 1666–1674, 2009.

[145] D. Hou, H. Ma, Y. Zhu, and Z. Li, "Calcium silicate hydrate from dry to saturated state: Structure, dynamics and mechanical properties," *Acta Materialia*, vol. 67, pp. 81–94, apr 2014.

[146] R.-M. Pellenq, N. Lequeux, and H. van Damme, "Engineering the bonding scheme in C-S-H: The iono-covalent framework," *Cement and Concrete Research*, vol. 38, no. 2, pp. 159–174, 2008.

[147] W. Sha, "Differential scanning calorimetry study of the hydration products in portland cement pastes with metakaolin replacement," in *Advances in Building Technology*, vol. I. Elsevier, 2002, pp. 881–888.

[148] H. E. Cardenas and L. J. Struble, "Electrokinetic Nanoparticle Treatment of Hardened Cement Paste for Reduction of Permeability," *Journal of Materials in Civil Engineering*, vol. 18, no. 4, pp. 554–560, aug 2006.

[149] P. Hou, X. Cheng, J. Qian, and S. P. Shah, "Effects and mechanisms of surface treatment of hardened cement-based materials with colloidal nanoSiO2 and its precursor," *Construction and Building Materials*, vol. 53, pp. 66–73, feb 2014.

[150] M. Sánchez, M. Alonso, and R. González, "Preliminary attempt of hardened mortar sealing by colloidal nanosilica migration," *Construction and Building Materials*, vol. 66, pp. 306–312, sep 2014.

[151] P. Hou, X. Cheng, J. Qian, R. Zhang, W. Cao, and S. P. Shah, "Characteristics of surface-treatment of nano-SiO2 on the transport properties of hardened cement pastes with different water-to-cement ratios," *Cement and Concrete Composites*, vol. 55, pp. 26–33, jan 2015.

[152] H. Li, H.-g. Xiao, J. Yuan, and J. Ou, "Microstructure of cement mortar with nano-particles," *Composites Part B: Engineering*, vol. 35, no. 2, pp. 185–189, mar 2004.

[153] T. Ji, "Preliminary study on the water permeability and microstructure of concrete incorporating nano-SiO2," *Cement and Concrete Research*, vol. 35, no. 10, pp. 1943–1947, oct 2005.

[154] J. Björnström, A. Martinelli, A. Matic, L. Börjesson, and I. Panas, "Accelerating effects of colloidal nano-silica for beneficial calcium-silicate-hydrate formation in cement," *Chemical Physics Letters*, vol. 392, no. 1-3, pp. 242–248, jul 2004.

[155] B.-W. Jo, C.-H. Kim, G.-h. Tae, and J.-B. Park, "Characteristics of cement mortar with nano-SiO2 particles," *Construction and Building Materials*, vol. 21, no. 6, pp. 1351–1355, jun 2007.

[156] C. Gallé, "Effect of drying on cement-based materials pore structure as identified by mercury intrusion porosimetry," *Cement and Concrete Research*, vol. 31, no. 10, pp. 1467–1477, oct 2001.

[157] L. Alarcon-Ruiz, G. Platret, E. Massieu, and A. Ehrlacher, "The use of thermal analysis in assessing the effect of temperature on a cement paste," *Cement and Concrete Research*, vol. 35, no. 3, pp. 609–613, mar 2005.

[158] A. Korpa and R. Trettin, "The influence of different drying methods on cement paste microstructures as reflected by gas adsorption: Comparison between freeze-drying (F-drying), D-drying, P-drying and oven-drying methods," *Cement and Concrete Research*, vol. 36, no. 4, pp. 634–649, apr 2006.

[159] W. Sha, E. O'Neill, and Z. Guo, "Differential scanning calorimetry study of ordinary Portland cement," *Cement and Concrete Research*, vol. 29, no. 9, pp. 1487–1489, sep 1999.

[160] S. Shaw, C. Henderson, and B. Komanschek, "Dehydration/recrystallization mechanisms, energetics, and kinetics of hydrated calcium silicate minerals: an in situ TGA/DSC and synchrotron radiation SAXS/WAXS study," *Chemical Geology*, vol. 167, no. 1-2, pp. 141–159, jun 2000.

[161] B. J. Christensen, T. O. Mason, and H. M. Jennings, "Comparison of Measured and Calculated Permeabilities," *Cement and Concrete Research*, vol. 26, no. 9, pp. 1325–1334, 1996.

[162] C. Hall and W. D. Hoff, *Water transport in brick, stone, and concrete*, C. Press, Ed. Spon Press, 2012.

[163] A. J. Allen, J. J. Thomas, and H. M. Jennings, "Composition and density of nanoscale calcium-silicate-hydrate in cement," *Nature Materials*, vol. 6, no. 4, pp. 311–316, 2007.

[164] M. S. Imbabi, C. Carrigan, and S. McKenna, "Trends and developments in green cement and concrete technology," *International Journal of Sustainable Built Environment*, vol. 1, no. 2, pp. 194–216, 2012.

[165] M. Schneider, M. Romer, M. Tschudin, and H. Bolio, "Sustainable cement production-present and future," *Cement and Concrete Research*, vol. 41, no. 7, pp. 642–650, jul 2011.

[166] E. Benhelal, G. Zahedi, E. Shamsaei, and A. Bahadori, "Global strategies and potentials to curb CO2 emissions in cement industry," *Journal of Cleaner Production*, vol. 51, no. 0, pp. 142–161, jul 2013.

[167] World Business Council for Sustainable Development and I. E. A. IEA, "Cement roadmap," Tech. Rep., 2010.

[168] D. A. Salas, A. D. Ramirez, C. R. Rodríguez, D. M. Petroche, A. J. Boero, and J. Duque-Rivera, "Environmental impacts, life cycle assessment and potential improvement measures for cement production: A literature review," *Journal of Cleaner Production*, vol. 113, pp. 114–122, 2016.

[169] A. Hasanbeigi, L. Price, H. Lu, and W. Lan, "Analysis of energy-efficiency opportunities for the cement industry in Shandong Province, China: A case study of 16 cement plants," *Energy*, vol. 35, no. 8, pp. 3461–3473, 2010.

[170] A. Hienola, J.-p. Pietikäinen, D. O. Donnell, A.-i. Partanen, and H. Korhonen, "The role of anthropogenic aerosol emission reduction in achieving the Paris Agreement 's objective," *Geophysical Research Abstracts*, vol. 19, 2017.

[171] WBCSD, "CO2 and Energy Accounting and Reporting Standard for the Cement Industry," Tech. Rep. May, 2011.

[172] Various, "Industrial Decarbonisation & Energy Efficiency Roadmaps to 2050 - Cement," Department for Business, Innovation & Skills and Department of Energy & Climate Change, Tech. Rep., 2015.

[173] R. Kajaste and M. Hurme, "Cement industry greenhouse gas emissions - Management options and abatement cost," *Journal of Cleaner Production*, vol. 112, pp. 4041–4052, 2016.

[174] H. Rostami and W. Brendley, "Alkali ash material: A novel fly ash-based cement," *Environmental Science and Technology*, vol. 37, no. 15, pp. 3454–3457, 2003.

[175] M. Cruz-Yusta, I. Mármol, J. Morales, and L. Sánchez, "Use of olive biomass fly ash in the preparation of environmentally friendly mortars," *Environmental Science and Technology*, vol. 45, no. 16, pp. 6991–6996, 2011.

[176] Y. Wu, J. Y. Wang, P. J. M. Monteiro, and M. H. Zhang, "Development of ultra-lightweight cement composites with low thermal conductivity and high specific strength for energy efficient buildings," *Construction and Building Materials*, vol. 87, pp. 100–112, 2015.

[177] P. Sturm, G. J. G. Gluth, H. J. H. Brouwers, and H. C. Kühne, "Synthesizing one-part geopolymers from rice husk ash," *Construction and Building Materials*, vol. 124, pp. 961–966, 2016.

[178] Q. Nie, W. Hu, T. Ai, B. Huang, X. Shu, and Q. He, "Strength properties of geopolymers derived from original and desulfurized red mud cured at ambient temperature," *Construction and Building Materials*, vol. 125, pp. 905–911, 2016.

[179] T. Hemalatha, M. Mapa, N. George, and S. Sasmal, "Physico-chemical and mechanical characterization of high volume fly ash incorporated and engineered cement system towards developing greener cement," *Journal of Cleaner Production*, vol. 125, pp. 268–281, 2016.

[180] A. Gameiro, A. Santos Silva, R. Veiga, and A. Velosa, "Hydration products of lime-metakaolin pastes at ambient temperature with ageing," *Thermochimica Acta*, vol. 535, pp. 36–41, may 2012.

[181] A. S. Silva, A. Gameiro, J. Grilo, R. Veiga, and A. Velosa, "Long-term behavior of lime-metakaolin pastes at ambient temperature and humid curing condition," *Applied Clay Science*, vol. 88, pp. 49–55, 2014.

[182] K. N. Yu, R. V. Balendran, S. Y. Koo, and T. Cheung, "Silica fume as a radon retardant from concrete," *Environmental Science and Technology*, vol. 34, no. 11, pp. 2284–2287, 2000.

[183] F. Sanchez and C. Ince, "Microstructure and macroscopic properties of hybrid carbon nanofiber/silica fume cement composites," *Composites Science and Technology*, vol. 69, no. 7-8, pp. 1310–1318, jun 2009.

[184] P. Aggarwal, R. P. Singh, and Y. Aggarwal, "Use of nano-silica in cement based materials - A review," *Cogent Engineering*, vol. 2, no. 1, p. 1078018, 2015.

[185] A. Lazaro, Q. Yu, and H. Brouwers, "Nanotechnologies for sustainable construction," in *Sustainability of Construction Materials*. Elsevier Ltd, 2016, ch. 4, pp. 55–78.

[186] K. Gao, K.-L. Lin, D. Wang, C.-L. Hwang, B. L. Anh Tuan, H.-S. Shiu, and T.-W. Cheng, "Effect of nano-SiO2 on the alkali-activated characteristics of metakaolin-based geopolymers," *Construction and Building Materials*, vol. 48, pp. 441–447, nov 2013.

[187] C. Heidrich, J. Sanjayan, M. L. Berndt, and S. Foster, "Pathways and barriers for acceptance and usage of geopolymer concrete in mainstream construction," in *2015 World of Coal Ash (WOCA) Conference in Nashville*, Nashville, 2015.

[188] A. Ahmed and A. Fried, "Flexural strength of low density blockwork," *Construction and Building Materials*, vol. 35, pp. 516–520, 2012.

[189] M. S. Al-homoud, "Performance characteristics and practical applications of common building thermal insulation materials," *Building and Environment*, vol. 40, pp. 353–366, 2005.

[190] K. Cho, Y. Hong, and J. Seo, "Assessment of the economic performance of vacuum insulation panels for housing projects," *Energy and Buildings*, vol. 70, pp. 45–51, 2014.

[191] F. Aldawi and F. Alam, "Residential Building Wall Systems," in *Thermofluid Modeling for Energy Efficiency Applications*, Elsevier, Ed. Elsevier Inc., 2016, ch. 8, pp. 169–196.

[192] A. M. Papadopoulos and E. Giama, "Environmental performance evaluation of thermal insulation materials and its impact on the building," *Building and Environment*, vol. 42, no. 5, pp. 2178–2187, 2007.

[193] S. Proietti, U. Desideri, P. Sdringola, and F. Zepparelli, "Carbon footprint of a reflective foil and comparison with other solutions for thermal insulation in building envelope," *Applied Energy*, vol. 112, pp. 843–855, 2013.

[194] A. G. Loudon, "The thermal properties of lightweight concretes," *International Journal of Cement Composites and Lightweight Concrete*, vol. 1, no. 2, pp. 71–85, 1979.

[195] B. C. McLellan, R. P. Williams, J. Lay, A. van Riessen, and G. D. Corder, "Costs and carbon emissions for geopolymer pastes in comparison to ordinary portland cement," *Journal of Cleaner Production*, vol. 19, no. 9-10, pp. 1080–1090, jun 2011.

[196] F. N. Stafford, A. C. Dias, L. Arroja, J. A. Labrincha, and D. Hotza, "Life cycle assessment of the production of Portland cement: A Southern Europe case study," *Journal of Cleaner Production*, vol. 126, pp. 159–165, 2016.

[197] F. N. Stafford, F. Raupp-Pereira, J. A. Labrincha, and D. Hotza, "Life cycle assessment of the production of cement: A Brazilian case study," *Journal of Cleaner Production*, vol. 137, pp. 1293–1299, 2016.

[198] L. Moretti and S. Caro, "Critical analysis of the Life Cycle Assessment of the Italian cement industry," *Journal of Cleaner Production*, vol. 152, pp. 198–210, 2017.

[199] S. Alonso and A. Palomo, "Alkaline activation of metakaolin and calcium hydroxide mixtures: influence of temperature, activator concentration and solids ratio," *Materials Letters*, vol. 47, no. 1-2, pp. 55–62, jan 2001.

[200] J. Zhang, Y. He, Y.-p. Wang, J. Mao, and X.-m. Cui, "Synthesis of a self-supporting faujasite zeolite membrane using geopolymer gel for separation of alcohol/water mixture," *Materials Letters*, vol. 116, pp. 167–170, feb 2014.

[201] Q. Lin, X. Lan, Y. Li, Y. Ni, C. Lu, Y. Chen, and Z. Xu, "Preparation and characterization of novel alkali-activated nano silica cements for biomedical application." *Journal of biomedical materials research. Part B, Applied biomaterials*, vol. 95, no. 2, pp. 347–56, nov 2010.

[202] J. Zhou, X. Chen, and L. Wu, "Influence of Free Water Content on the Compressive Mechanical Behaviour of Cement Mortar under High Strain Rate," *Sadhana*, vol. 36, no. June, pp. 357–369, 2011.

[203] X. Chen, W. Huang, and J. Zhou, "Effect of moisture content on compressive and split tensile strength of concrete," *Indian Journal of Engineering & Materials Sciences*, vol. 19, no. December, pp. 427–435, 2012.

[204] E. Reffold, F. Leighton, F. Choudhury, and P. S. Rayner, "Greenhouse gas emissions of water supply and demand management options," Environment Agency, Tech. Rep., 2008.

[205] A. Mellado, C. Catalán, N. Bouzón, M. V. Borrachero, J. M. Monzó, and J. Payá, "Carbon footprint of geopolymeric mortar: study of the contribution of the alkaline activating solution and assessment of an alternative route," *RSC Adv.*, vol. 4, no. 45, pp. 23 846–23 852, 2014.

[206] P. Duxson, J. L. Provis, G. C. Lukey, and J. S. J. van Deventer, "The role of inorganic polymer technology in the development of 'green concrete'," *Cement and Concrete Research*, vol. 37, no. 12, pp. 1590–1597, 2007.

[207] IPCC, "Chapter 2: Mineral Industry Emissions," *2006 IPCC Guidelines for National Greenhouse Gas Inventories*, vol. 3, p. 40, 2006.

[208] C. C. S. Chan, D. Thorpe, and M. Islam, "An evaluation carbon footprint in fly ash based geopolymer cement and ordinary Portland cement manufacture," *IEEE International Conference on Industrial Engineering and Engineering Management*, vol. 2016-Janua, no. 1, pp. 254–259, 2016.

[209] EU, "Reference document on best available techniques for the manufacture of large volume inorganic chemicals - Silica and others," *European Commission*, vol. BREF - LVI, no. August, pp. 1–711, 2007.

[210] O. Ünal, T. UygunoÇğlu, and A. Yildiz, "Investigation of properties of low-strength lightweight concrete for thermal insulation," *Building and Environment*, vol. 42, no. 2, pp. 584–590, 2007.

[211] P. Palmero, A. Formia, P. Antonaci, S. Brini, and J. M. Tulliani, "Geopolymer technology for application-oriented dense and lightened materials. Elaboration and characterization," *Ceramics International*, vol. 41, no. 10, pp. 12 967–12 979, 2015.

[212] K. S. Al-Jabri, A. W. Hago, A. S. Al-Nuaimi, and A. H. Al-Saidy, "Concrete blocks for thermal insulation in hot climate," *Cement and Concrete Research*, vol. 35, no. 8, pp. 1472–1479, 2005.

[213] T. M. Prakash, B. G. Naresh, B. G. Karisiddappa, and S. Raghunath, "Properties of Aerated (Foamed) Concrete Blocks," *International Journal of Scientific & Engineering Research*, vol. 4, no. 1, pp. 1–5, 2013.

[214] J. Grilo, A. Santos Silva, P. Faria, A. Gameiro, R. Veiga, and A. Velosa, "Mechanical and mineralogical properties of natural hydraulic lime-metakaolin mortars in different curing conditions," *Construction and Building Materials*, vol. 51, pp. 287–294, 2014.

[215] A. Gameiro, A. Santos Silva, P. Faria, J. Grilo, T. Branco, R. Veiga, and A. Velosa, "Physical and chemical assessment of lime-metakaolin mortars: Influence of binder:aggregate ratio," *Cement and Concrete Composites*, vol. 45, pp. 264–271, 2014.

[216] Z. Zhang, H. Wang, J. L. Provis, F. Bullen, A. Reid, and Y. Zhu, "Quantitative kinetic and structural analysis of geopolymers. Part 1. the activation of metakaolin with sodium hydroxide," *Thermochimica Acta*, vol. 539, pp. 23–33, 2012.

[217] L. Gomez-Zamorano, M. Balonis, B. Erdemli, and N. Neithalat, "Structure, Composition and Thermochemical Properties of C-(N)-S-H and N-A-S-H Gels," in *1st International Conference on Grand Challenges in Construction Materials*, 2016, pp. 1–9.

[218] L. Gomez-Zamorano, M. Balonis, B. Erdemli, N. Neithalath, and G. Sant, "C-(N)-S-H and N-A-S-H gels: Compositions and solubility data at 25 C and 50 C," *Journal of the American Ceramic Society*, no. May 2016, pp. 2700–2711, 2017.

[219] L. Reig, L. Soriano, M. Borrachero, J. Monzó, and J. Payá, "Influence of calcium aluminate cement (CAC) on alkaline activation of red clay brick waste (RCBW)," *Cement and Concrete Composites*, vol. 65, pp. 177–185, 2016.

[220] J. Fricke, U. Heinemann, and H. P. Ebert, "Vacuum insulation panels-From research to market," *Vacuum*, vol. 82, no. 7, pp. 680–690, 2008.

[221] F. X. Alvarez, D. Jou, and A. Sellitto, "Pore-size dependence of the thermal conductivity of porous silicon: A phonon hydrodynamic approach," *Applied Physics Letters*, vol. 97, no. 3, pp. 1–4, 2010.

[222] J. Bull, A. Gupta, D. Mumovic, and J. Kimpian, "Life cycle cost and carbon footprint of energy efficient refurbishments to 20th century UK school buildings," *International Journal of Sustainable Built Environment*, vol. 3, no. 1, pp. 1–17, 2014.

Publications and presentations

The following is a full list of peer reviewed journal publications, conference presentations and proceedings papers that resulted and/or are related with this thesis.

Journals

[1] R. Maddalena and A. Hamilton, "Low-pressure silica injection for porosity reduction in cementitious materials", *Construction and Building Materials*, vol.134, pp.610–616, Mar 2017.

[2] R. Maddalena, Li Kefei and A. Hamilton, "Direct synthesis method of solid Calcium Silicate Hydrate phase with tobermorite-like structure", in review.

[3] R. Maddalena, J. Roberts and A. Hamilton, "Can Portland cement be replaced by low-carbon materials? A study on thermal properties and carbon emissions of innovative cements", accepted for publication at *Journal of Cleaner Production*, Feb 2018.

[4] R. Maddalena, S. Michalik and A. Hamilton, "Hydrothermal synthesis of calcium silicate hydrate: structural studies on the effect of temperature and calcium to silicate ratio", in review.

[5] R. Maddalena and A. Hamilton, "Effect of silica particle size on the hydration of calcium silicate hydrate investigated by thermal analysis", in review.

Conferences

[1] R. Maddalena, A. Mali and A. Hamilton, "Low-pressure silica injection for crack sealing and water transport", *SAHC 2016, 10^{th} Structural Analysis of Historical Constructions Conference*, 13–16 September 2016, Leuven, Belgium. Published in "Structural Analysis of Historical

Constructions–Anamnesis, diagnosis, therapy, controls" Van Balen & Verstrynge (Eds) 2016 Taylor & Francis Group, London, ISBN 978-1-138-02951-4.

[2] R. Maddalena A. Mali and A. Hamilton, "Low-pressure silica injection for crack sealing and water transport", *36^{th} Cement and Concrete Science Conference*, 5–6 September 2016, Cardiff, UK. Published in "Proceedings of the 36^{th} Cement and Concrete Science Conference" Gary Perkins (Eds) 2016 IOM3, London, ISBN 978-1-86125-175-6.

[3] R. Maddalena and A. Hamilton, "X-ray diffraction and Raman spectroscopy of synthetic calcium silicate hydrate (C-S-H)", *35^{th} Cement and Concrete Science Conference, 26–28 August 2015*, Aberdeen, UK. Published in "Proceedings of the 35^{th} Cement and Concrete Science Conference".